Collinear Laser Spectroscopy of Magic Lead and Mid-Shell Palladium Isotopes

Kollineare Laserspektroskopie magischer Blei- und offenschaliger Palladiumisotope
Zur Erlangung des Grades eines Doktors der Naturwissenschaften (Dr. rer. nat.)
Genehmigte Dissertation im Fachbereich Physik von Laura Renth
Tag der Einreichung: 25.06.2024, Tag der Prüfung: 22.07.2024

1. Gutachten: Prof. Dr. Wilfried Nörtershäuser
2. Gutachten: Prof. Dr. Alexandre Obertelli
Darmstadt, Technische Universität Darmstadt

TECHNISCHE UNIVERSITÄT DARMSTADT

Physics Department
Institut für Kernphysik
LaserSpHERe

Collinear Laser Spectroscopy of Magic Lead and Mid-Shell Palladium Isotopes
Kollineare Laserspektroskopie magischer Blei- und offenschaliger Palladiumisotope

Accepted doctoral thesis in the department of Physics by Laura Renth

Date of submission: 25.06.2024
Date of thesis defense: 22.07.2024

Darmstadt, Technische Universität Darmstadt

Erklärungen laut Promotionsordnung

§ 8 Abs. 1 lit. d PromO

Ich versichere hiermit, dass zu einem vorherigen Zeitpunkt noch keine Promotion versucht wurde. In diesem Fall sind nähere Angaben über Zeitpunkt, Hochschule, Dissertationsthema und Ergebnis dieses Versuchs mitzuteilen.

§ 9 Abs. 1 PromO

Ich versichere hiermit, dass die vorliegende Dissertation – abgesehen von den in ihr ausdrücklich genannten Hilfen – selbstständig verfasst wurde und dass die „Grundsätze zur Sicherung guter wissenschaftlicher Praxis an der Technischen Universität Darmstadt“ und die „Leitlinien zum Umgang mit digitalen Forschungsdaten an der TU Darmstadt“ in den jeweils aktuellen Versionen bei der Verfassung der Dissertation beachtet wurden.

§ 9 Abs. 2 PromO

Die Arbeit hat bisher noch nicht zu Prüfungszwecken gedient.

Darmstadt, 25.06.2024

L. Renth

Abstract

Nuclear size and shape are fundamental physical properties defined by the composition of neutrons and protons within the nucleus. The precise investigation of both properties provides benchmarks for nuclear models and helps to understand the nucleon-nucleon interaction. The nuclear charge radius and the nuclear magnetic dipole and electric quadrupole moments can be probed by the well-known electromagnetic interaction and extracted from atomic spectra. Collinear laser spectroscopy (CLS) is a versatile tool to measure and resolve fine structure and hyperfine structure required to extract the nuclear parameters. It is an in-flight spectroscopy method and therefore very well suited for short-lived isotopes and isomeric states.

A new online collinear laser spectroscopy setup, the **A**rgonne **T**andem Hall **La**ser Beamli**n**e for A**t**om and **I**on **S**pectroscopy (ATLANTIS) has been commissioned in this work with first online beams of $^{110,112-116,118}$Pd delivered from the Californium Rare Isotope Breader Upgrade (CARIBU). The required high sensitivity for these investigations of palladium isotopes with very low production yields was achieved by a new radio-frequency quadrupole cooler-and-buncher with unprecedented long accumulation times of up to $30\,$s. A new charge-exchange cell, designed specifically for the charge exchange with magnesium, provided unexpected high neutralization efficiency with almost undisturbed and symmetric resonance profiles.

Using the new setup, spectra of all stable and the neutron-rich $^{112-116,118}$Pd isotopes were obtained, the spins of ^{113,115}Pd confirmed, their magnetic dipole moments and the electric quadrupole moment of ^{113}Pd determined, and the trend of the differential nuclear charge radii along the chain of measured isotopes established. The results indicate a complex nuclear structure and are compared to other isotopic chains in the Pd region and to axial Fayans EDF and triaxial Skyrme EDF calculations. The good agreement with the EDF calculations allowing triaxiality, supports the possible existence of triaxial ground states in the mid-shell region between $Z=26$ and $Z=50$ and around $N=60$.

Moreover, CLS measurements were performed at the COLLAPS experiment at ISOLDE/CERN on semi-magic lead isotopes. The differential mean-square nuclear charge radii and nuclear moments of $^{187-208}$Pb and of the isomeric states of the odd $^{187-203}$Pb isotopes were determined. A comparison to Fayans and ab initio calculations show an overall good agreement.

Zusammenfassung

Größe und Form eines Atomkerns sind grundlegende physikalische Eigenschaften, die durch die Verteilung der Neutronen und Protonen bestimmt werden. Die genaue Untersuchung beider Eigenschaften liefert wichtige Informationen für Kernmodelle und trägt zum Verständnis der Wechselwirkung zwischen Nukleonen bei. Der Kernladungsradius und die elektromagnetischen Kernmomente können aus Atomspektren extrahiert werden. Die kollineare Laserspektroskopie (CLS) ist eine vielseitige Methode zur Messung der Hyperfeinstruktur optischer Übergänge, die sich besonders für kurzlebige Isotope und isomere Zustände eignet.

Ein neuer Online-Aufbau für CLS, die **A**rgonne **T**andem Hall **La**ser Beamli**n**e for A**t**om- and **I**on **S**pectroscopy (ATLANTIS), wurde im Rahmen dieser Arbeit mit ersten Online-Strahlen von $^{110,112-116,118}$Pd des Californium Rare Isotope Breader Upgrades (CARIBU), in Betrieb genommen. Die erforderliche hohe Empfindlichkeit für Untersuchungen dieser Isotope mit geringen Ionenstrahlintensitäten von 1-10 Ionen/s wurde durch einen neuen Hochfrequenz-Quadrupol-Kühler und -Buncher gewährleistet, mit dem erstmals Akkumulationszeiten von bis zu $30\,$s ohne größere Verluste erreicht wurden. Eine neue Ladungsaustauschzelle, speziell für Ladungsaustausch mit Magnesium entwickelt, lieferte eine unerwartet hohe Neutralisationseffizienz bei nahezu ungestörten und symmetrischen Resonanzprofilen.

Mit dem neuen Aufbau wurden Spektren von stabilen und den neutronenreichen $^{112-116,118}$Pd Isotopen aufgenommen, die Spins von ^{113,115}Pd bestätigt, ihre magnetischen Dipol- und elektrischen Quadrupolmomente bestimmt sowie der Trend der differentiellen Kernladungsradien entlang der Kette der gemessenen Isotope ermittelt. Die Ergebnisse weisen auf eine komplexe Kernstruktur hin und werden mit anderen Isotopenketten im Pd-Bereich sowie mit axialen Fayans- und triaxialen Skyrme-Energiedichtefunktional (EDF)-Berechnungen verglichen. Die gute Übereinstimmung mit den EDF-Rechnungen, die Triaxialität zulassen, unterstützt die mögliche Existenz triaxialer Grundzuständen offenschaliger Isotope zwischen $Z=26$ und $Z=50$ und um $N=60$.

Des Weiteren wurden CLS-Messungen am COLLAPS-Experiment an ISOLDE/CERN an semimagischen Blei-Isotopen durchgeführt. Die differentiellen Kernladungsradien und Kernmomente von $^{187-208}$Pb sowie der isomeren Zustände der ungeraden $^{187-203}$Pb-Isotope wurden bestimmt und stimmen insgesamt gute mit Fayans-EDF- und ab initio Berechnungen überein.

Contents

List of Figures

List of Tables

1 Introduction

Since its discovery by Rutherford in 1911 [1] physicists try to obtain a consistent picture of the atomic nucleus. Using alpha-scattering, he could show that an atomic nucleus was not point-like, but a few fm in size [2]. He also observed the first nuclear reaction [3], leading to the conclusion that protons, which form the nucleus of ordinary hydrogen ^{1}H, are constituents of heavier nuclei. The occurrence of chemically identical isotopes of the same element, but with different masses was only understood after the discovery of the neutron by Chadwick in 1932 [4]. Since then, atomic nuclei are treated as systems of neutrons and protons, the *nucleons*. However, their complete interaction and dynamics inside the nucleus is only partially understood. Therefore, the main goal of nuclear physicists is to explore the nuclear structure and nucleon-nucleon interactions.

One of the earliest models is the liquid drop model [5, 6], which treats nuclei similarly to a water drop bound by surface tension. It also takes into account the repulsive Coulomb force between protons and the effect arising from the Pauli exclusion principle that an equal number of protons and neutrons is favoured in a nucleus. The liquid-drop model predicts a smooth trend of binding energies and masses along the nuclear chart.

Around 1950, sharp irregularities from such an overall smooth trend were noticed in nuclear masses and binding energies at nuclei of specific neutron or proton numbers [7, 8]. The discovery of these *magic numbers* lead to the development of the famous nuclear shell model by Goeppert-Mayer and Jensen [9]. This model perfectly reproduces the observed magic numbers, i.e., the unexpected stability of *magic nuclei* with magic neutron and proton numbers. It assumes a spherical nuclear binding potential created by the average potential of all other nucleons with distinct single-particle binding energy levels, leading to a spherical nuclear shape for magic nuclei in their ground state.

Later on, Bohr, Mottelson and Nilsson extended the shell model to deformed nuclei, which are observed especially in the mid-shell region [10, 11]. Many of these have still axial symmetry and are oblate or prolate. The shape directly influences the electro-magnetic nuclear moments and the observable nuclear radii. This also motivates that isomers (long-lived excited states) may have a different nuclear size compared to their ground states.

Many further approaches have been developed over the past century, like ab initio calculations starting with individual nucleons in, e.g., the no-core shell model or Green's function Monte Carlo calculations. A complementary approach is the energy density functional (EDF) theory, which is based on densities and currents instead of individual nucleons. Significant progress has been made in both fields during recent years particularly with respect to nuclear charge radii [12, 13, 14, 15, 16]. Their predictions are compared to nuclear ground state and nuclear transition properties.

Atomic physics studies of short-lived isotopes play an important role in this endeavor, since mass and laser spectroscopy allow a precise and nuclear-model independent approach to nuclear ground-state properties like masses, spins, nuclear moments and charge radii [17]. This work investigates spherical lead nuclei as well as the deformed palladium region, using a laser-spectroscopic technique.

For (semi-) magic nuclei, like the tin and lead isotopes, the spherical nuclear shell model has been applied successfully to, e.g., the nuclear spin and the nuclear structure. The ^{208}Pb nucleus, with $Z = 82$ and $N = 126$, is a textbook example of a doubly magic nucleus, having large excitation energies and a spherical shape [18].

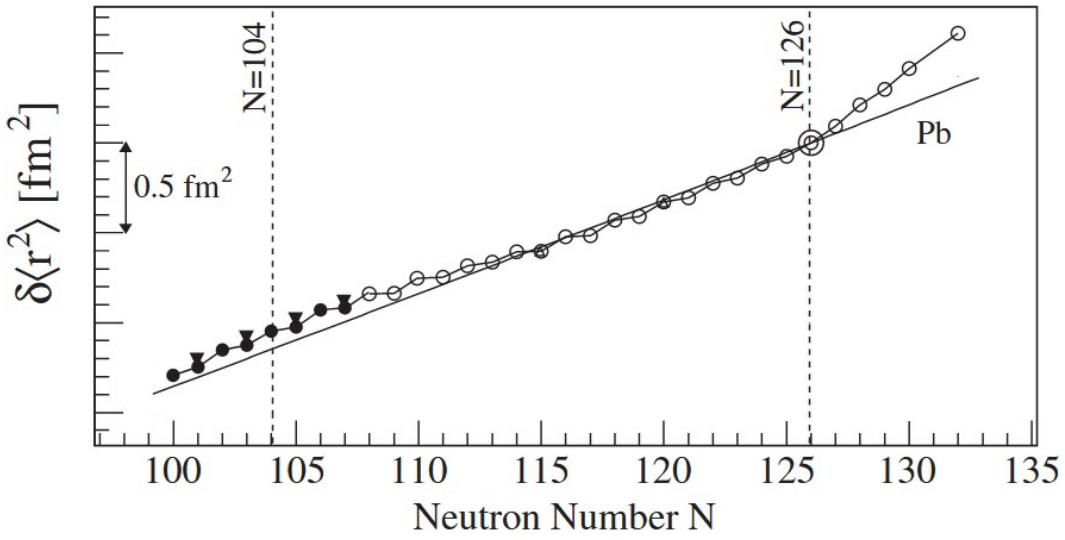

Figure 1.1: Experimental differential mean-square (ms) charge radii $\delta\langle r^2\rangle$ along the lead isotopic chain. The ground states are represented by circles, the isomeric states by triangles. The solid line represents theoretical predictions assuming zero deformation, i.e., spherical nuclei. The good agreement of the experimental data to this linear model hints to a very weak deformation from a spherical shape for lead nuclei. Figure taken from [19]. Reprinted figure with permission from Hilde de Witte. Copyright 2007 by the American Physical Society, cropped from original.

The size of nuclei is often calculated by the droplet model [20] with a certain amount of deformation. As can be seen in Fig. 1.1 the nuclear charge radii evolve along an isodeformation line. The isodeformation line of vanishing deformation is shown by the solid linear line reaching across the whole range of neutron numbers N. The experimental values below $N = 126$ are in good agreement with it, showing the robustness of the $Z = 82$ shell closure. Only towards the middle between the $N = 82$ and $N = 126$ shell closures, around $N = 104$, a slightly increasing deformation is observed.

A change in the slope (kink) as it is visible at $N = 126$ has been observed for all traditional magic numbers with $N > 20$, but only recently for $N = 20$ in the scandium isotopes [21]. Its reason is still under debate and a topic of investigation [13, 22].

The most simple approach, the single-particle shell model, uses a single-particle-like description to predict nuclear moments and shapes. For nuclei with more than one particle or hole in an incompletely filled shell, the pairing effect must be taken into account. This is done by the seniority scheme, which was already introduced by Racah [23, 24] for atomic physics, and later applied to the nucleus by Racah, Talmi and Flowers [25, 26].

This seniority scheme can explain characteristic trends in the isomer shifts, i. e. the charge radii differences between the nuclear ground state and the isomeric state, in cadmium isotopes, as it was observed in [28]. In [29], a linearly increasing quadrupole moment was observed for the $^{11}/_{2}^{-}$ unique-parity isomeric states, as it was predicted already by the spherical shell model for single-particle proton states [9] and for single-particle neutron states by [30]. For nucleons of both types outside a closed shell, the seniority scheme predicts a linearly increasing quadrupole moment. This linearity, together with a postulated constant deformation of the ground-state cadmium isotopes, is in [28] connected to the observed quadratic behavior of isomer shifts, which is depicted in Fig. 1.2. The slightly negative offset of the observed parabola is explained by a weak but constant deformation of the nuclear ground state.

A similar trend of the isomer shift was also observed in the magic tin isotopes [27], although the quadrupole moments of the isomeric states increase with a rather quadratic than linear function. For a better understanding of this behavior, the investigation of these trends in similar isotopic chains, e.g. in lead, is needed. This was one motivation for this work, since in lead, the isomeric charge radii and nuclear moments, if known at all, were only measured with large uncertainties. This work presents measurements of these nuclear properties with uncertainties improved by about an order of magnitude.

Continuing the investigation of isomeric trends away from the $Z = 50$ shell closure, initially motivated the experiments performed on palladium within this work. In contrast to the 'simple-structured' lead and tin isotopes, predictions on mid-shell nuclei are more complex and elaborate. Their intricate nuclear structure can lead to nuclear shapes of large deforma-

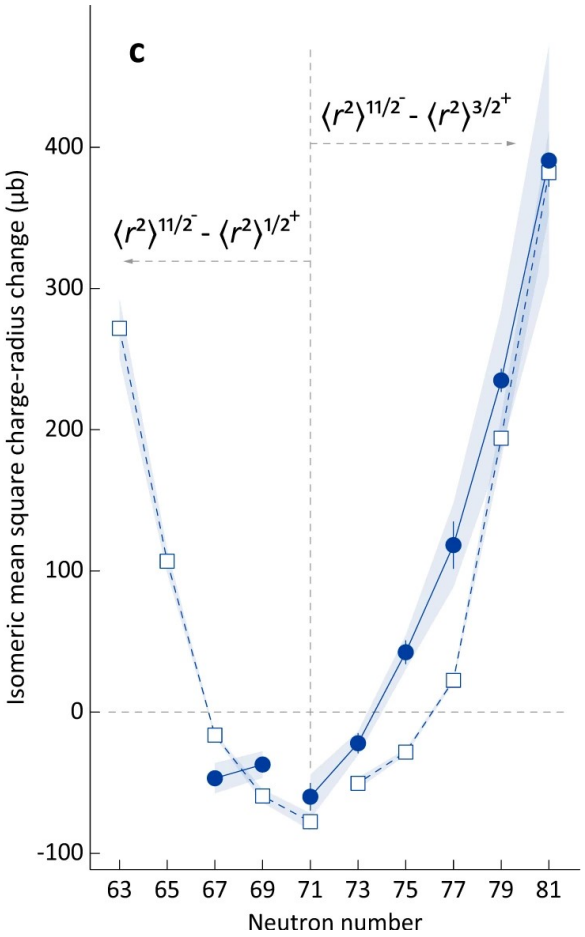

Figure 1.2: Experimental differential ms charge radii of isomeric states ($11/2^-$) in tin (circles) and cadmium (squares) relative to the ground states ($1/2^+$ and $3/2^+$). Figure taken from [27], used under CC by 4.0, cropped from original.

tion or to triaxiality, removing the axial symmetry. In the mid-shell region between the proton shell closures $Z = 28$ and $Z = 50$ and between the neutron shell closures $N = 50$ and $N = 82$, characteristics indicating triaxial ground states have been observed among some Sr, Mo, Ru, Pd and Cd isotopes [31]. In the same region a sudden shape-change at $N = 60$ has been identified in the $37 < Z < 41$ mid-shell isotopes, which manifests in Fig. 1.3 as a sudden increase in the nuclear charge radius [32]. Measurements of charge radii and nuclear moments of palladium are therefore of particular interest, as they continue the investigation of nuclear shapes to higher Z isotopes, approaching the $Z = 50$ shell closure. At the same time, this region is nevertheless known to exhibit triaxial nuclear ground states [40].

The triaxial shape of nuclei in their ground state is considered in a series of energy density functional calculations (EDF) based on the Brussels-Montréal Skyrme (BSk) interactions [31,

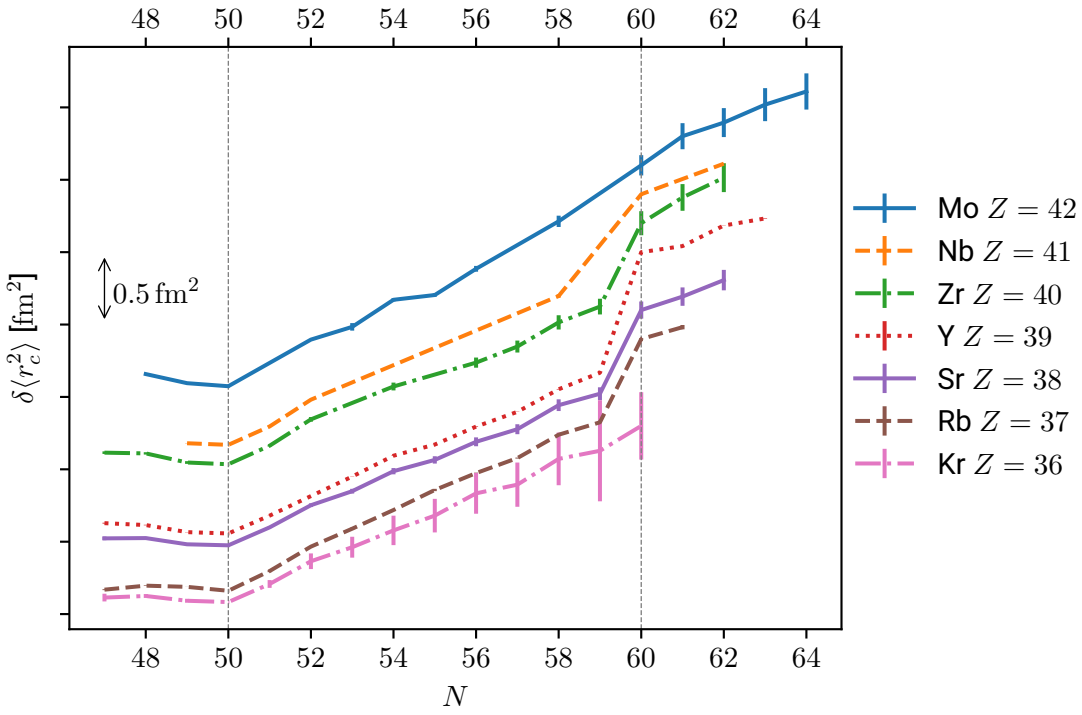

Figure 1.3: Differential ms charge radii $\delta\langle r^2\rangle^{N,60}$ along isotopic chains between krypton ($Z = 36$) and molybdenum ($Z = 42$). For a separation of the individual curves an increasing offset of $0.2\,\mathrm{fm}^2$ per chemical element was added. All isotopic chains reveal a kink at the magic neutron shell closure $N = 50$, which is related to its magicity. In Rb, Sr, Zr and Nb a sudden increase in the charge radius is observed at $N = 60$, caused by a sudden shape change. Values are taken from [33, 34, 35, 36, 37, 38, 39].

41, 42]. A comparison of EDF calculations allowing axial or tiaxial deformations with experimental data can contribute to proving the existence of triaxial ground-state nuclei in the palladium isotopic chain. Comparing EDF calculations based on different nucleon-nucleon interactions with experimental data can reveal important information on the nuclear force.

Precise collinear laser spectroscopy (CLS) measurements on lead and palladium were performed and analyzed as a central part of this work. With CLS we can explore the structure of exotic, short-lived isotopes ($\geq 10\,\mathrm{ms}$) and isomers. This is possible by performing the measurement in flight with a collinear alignment of the spectroscopy laser beam with the ion beam. The collinear geometry leads to a Doppler compression and, thus, spectroscopy with high-resolution can be performed.

The measurements on lead were performed at the COLLAPS experiment at ISOLDE/CERN. COLLAPS was the pioneering CLS setup [43] and still serves as a reliable instrument for online

laser spectroscopy [44]. With the implementation of the radio-frequency quadrupole cooler-and-buncher ISCOOL, a considerable boost of sensitivity was achieved [44]. For many cases, atoms offer better spectroscopic transitions than singly-charged ions. COLLAPS is therefore equipped with a charge-exchange cell (CEC), which converts the ion beam into an atomic beam for CLS.

The measurements and the analysis of the nuclear moments and charge radii of lead are presented in chapter 6.1. The observed trends in the ground state and isomeric nuclear rms charge radii are discussed regarding the magicity of lead in comparison to the magic tin isotopes and the almost magic cadmium isotopes.

The measurements on palladium were performed at the Argonne National Laboratory (ANL). There, the new Argonne Tandem Hall LAser beamliNe for aTom and Ion Spectroscopy (ATLANTIS) was set up. The new installation is attached to CARIBU [45], a californium fission source. This allows the production of refractory metals, that cannot be efficiently produced by the ISOL-technique at ISOLDE. This was demonstrated in the first online measurements performed on palladium which are presented in chapter 7.1.

For high sensitivity at low production rates, the ion beam is bunched by a radio-frequency quadrupole cooler-and-buncher (RFQCB) before it enters the CLS beamline. The RFQCB performs remarkably well for unprecedented long accumulation times of up to $30\,\mathrm{s}$, before an ion bunch is released. This enables a strong photon background suppression, allowing laser spectroscopy on beams of only $10 - 100$ particles per second.

The charge exchange was successfully performed with a newly designed CEC that uses for the first time a magnesium vapour for the charge-exchange process. The CEC was specifically desigend for ATLANTIS, allowing operating temperatures of up to $400 - 500\,^{\circ}\mathrm{C}$ [46]. Magnesium as a charge-exchange agent was chosen, to provide resonant charge exchange with palladium with a high population of low lying atomic states. The total efficiency of this design has proven to be extremely successful, without any visible impact on the beam properties.

The new ATLANTIS setup and its performance is described in detail in chapter 4.3. The achieved results on the mid-shell palladium isotopes are used to investigate the shape evolution along the palladium isotopic chain in comparison to other isotopes in the mid-shell region. Also the possibility of triaxial nuclear ground states is discussed, by comparing the experimental data to axial and triaxial EDF calculations. The nuclear moments are discussed regarding the nuclear structure also in comparison to the neighboring isotopes in chapter 7.2.

2 Theory

In this chapter the theoretical background for this work is set. The first part covers nuclear properties and the basics of nuclear theory that are relevant for the discussion of the experimental results. In the second part, atomic theory and the interaction of atoms and photons are discussed

2.1 Nuclear Theory

Since the discovery of the neutron in 1932 by Chadwick [4], the picture of the nucleus consisting of protons and neutrons, the *nucleons*, is commonly accepted. Both types of nucleons have an intrinsic angular momentum, a spin, of $^1/_2\hbar$. The proton is stable and carries one elementary charge while a free neutron has a half-life of about 10 min [47, 48] and total electric charge zero.

The interactions between these nucleons are of high interest to nuclear physicists, since they were identified as the constituents of nuclei. The electric and repulsive Coulomb interaction between the protons was very well known from the beginning. In order to explain the existence of bound nuclei, a short range attractive force between nucleons was assumed [49] and in 1930, Gamow formulated the liquid drop model [5] to describe the nuclear binding energy B in dependence of the mass number A of an isotope, the charge Z and the neutron number N. It was further developed by Weizsäcker and Bethe to the semi-empirical mass formula [50]

$$B = aA - \sigma A^{2/3} - cZ^2A^{-1/3} - s\frac{(N-Z)^2}{A} + +\delta \cdot pA^{-1/2} \tag{2.1}$$

where the first term a is the volume term, which accounts for the saturation of nucleons inside a nucleus, the second term describes a surface tension effect proportional to the nuclear surface, the third term accounts for the repulsive Coulomb force acting only on protons, the fourth term is the symmetry energy, indicating the preference for equal proton and neutron number. The last term is added to describe the observed preference of even-even isobars, where δ is $+1$ for even-even, -1 for odd-odd and 0 for odd nuclei, and it is called the pairing energy. It is explained in the nuclear shell model (see next section) by the formation of neutron-neutron

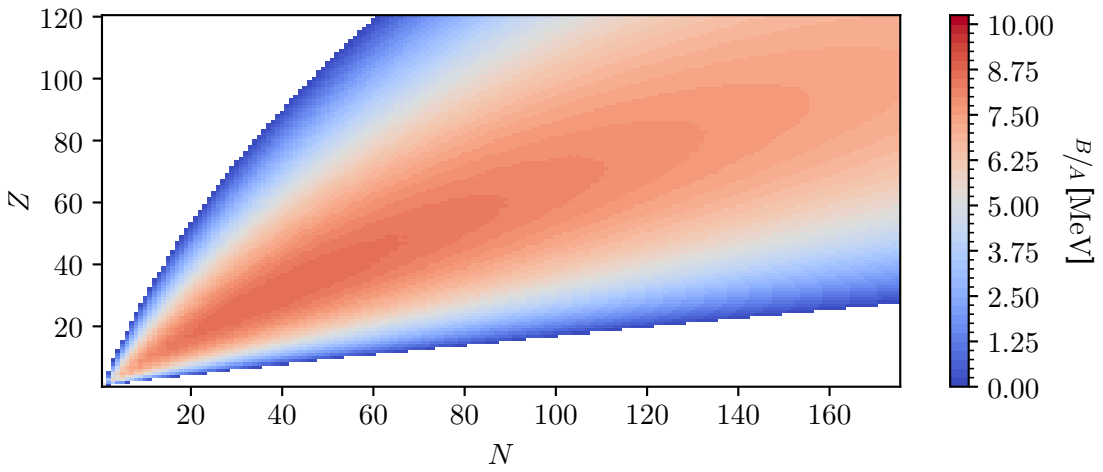

Figure 2.1: Binding energy per nucleon color plotted as a function of neutron number N and proton number Z, as given by Eq. (2.1). The parameters were taken from [50]: $a = 15.84\,\text{MeV}$, $\sigma = 18.33\,\text{MeV}$, $= 0.714\,\text{MeV}$, $s = 23.2\,\text{MeV}$, $p = 12\,\text{MeV}$.

and proton-proton pairs, while for an odd nucleus or odd-odd nucleus, the unpaired nucleons are less strongly bound. The parameters a, σ c, s and p were originally fitted to experimental data. Equation (2.1) describes the general trend of the binding energy per nucleon for the stable isotopes as is depicted in Fig. 2.1.

2.1.1 Nuclear Shell Model

Although Eq. (2.1) is an overall good approximation of the binding energy, for certain neutron and proton numbers larger deviations can be observed at specific points along the nuclear chart. Figure 2.2 shows the two-proton-two-neutron differential binding energy

$$\Delta B^{(2)} = B(N+2, Z+2) + B(N-2, Z-2) - 2B(N, Z) \tag{2.2}$$

across the nuclear chart. It strikingly shows that the proton numbers Z and neutron numbers $N = 2, 8, 20, 28, 50, 126, ...$ stand out, as these nuclei are more strongly bound than their neighboring nuclei. These numbers are called the *magic numbers* and they were explained by Goeppert Mayer [52] and Jensen [53] in the nuclear shell model [9]. It assumes that protons and neutrons can be arranged in shells, similarly to bound electrons in the atomic shell model.

In the nuclear shell model, it is assumed that each nucleon moves in a spherically symmetric average potential $V(r)$, created by the other nucleons but independent of their exact positions. Similarly to the atomic orbits, the possible nuclear orbits are characterized by quantum num-

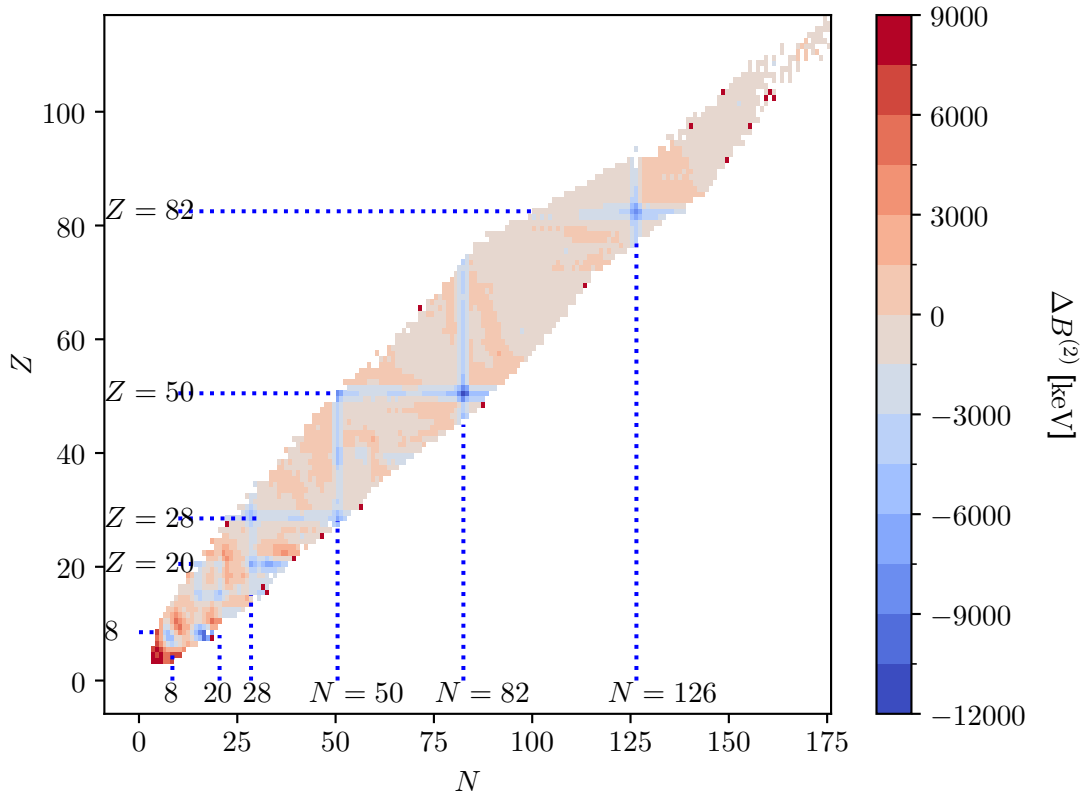

Figure 2.2: The two-proton-two-neutron differential binding energies according to Eq. (2.2), color-plotted across the nuclear chart. Negative values (blue) indicate that the nucleus is more strongly bound than its neighboring nuclei. Binding energies per nucleon are taken from [51].

bers (n, l, j). According to the Pauli principle, each orbit can be occupied by only a limited number of nucleons of the same type. Since the Coulomb potential shifts the proton orbits to higher energies, neutrons and protons do not share orbits. The following chapter, briefly introduces the nuclear shell model by Goeppert Mayer and Jensen.

Isotropic Nuclear Potential: The nuclear shell model reduces the interaction between nucleons to a single-particle potential $V(r)$ acting on every single nucleon and generated by all other nucleons. The nuclear shell structure and the resulting magic numbers are in first order defined by this nuclear potential $V(r)$.

The observed nuclear magic numbers are different from the atomic magic numbers as the

interaction between nucleons is mainly governed by the strong nuclear force. Therefore the nuclear potential $V(r)$ cannot be described in the same way as the atomic potential. There are some restrictions for the construction of the nuclear potential:

- $V(r)$ is generated by the other nucleons.
- The nuclear density saturates inside the nucleus, such that $V(0)$ cannot be singular.
- $V(r)$ must quickly go to zero at the nuclear surface ($r = R$) as the strong nuclear force is a short range interaction.

These requirements can be fulfilled by various potentials, such as a square well or a harmonic oscillator potential. In the harmonic oscillator model the discretization of the energy levels is given by [9]

$$\epsilon_{n_0} = n_0 \hbar\omega \tag{2.3}$$

with the oscillation quantum number $n_0 = 2(n-1) + l$, radial quantum number n and orbital angular momentum quantum number l . According to the possible combinations of n and l, each of these energy levels ϵ_{n_0} is degenerated leading to the magic numbers 2, 8 and 20. This degeneracy is lifted in case of the square-well potential or the more realistic Woods-Saxon potential. The mentioned magic numbers nevertheless remain. Higher magic numbers as observed in experiments are, however, not reproduced in this approach. This is resolved by considering spin-orbit interactions.

Spin-Orbit Potential: Since nucleons do not only carry the orbital momentum $\boldsymbol{l}$ but also an intrinsic spin $\boldsymbol{s}$, a spin-orbit coupling potential of the form $f(r)\,(\boldsymbol{s}\cdot\boldsymbol{l})$ can be introduced, which splits and shifts the energy levels ϵ_{n_0}. The radial factor $f(r)$ depends on the exact form of the nuclear force. In analogy to the electronic case, it is often chosen as $f(r) \propto -1/r \cdot \mathrm{d}V/\mathrm{d}r$. The potential peaks at the nuclear surface. The scalar product $\boldsymbol{s}\cdot\boldsymbol{l}$ can be expressed by the coupling of the intrinsic spin $\boldsymbol{s}$ and the orbital angular momentum $\boldsymbol{l}$ of a nucleon to the total angular momentum $\boldsymbol{j} = \boldsymbol{l} + \boldsymbol{s}$. This implies l, s and j are 'good quantum numbers', i.e. j^2, j_z, l^2 and s^2 are conserved quantities.

Although the exact nucleon-nucleon interaction is not sufficiently known to predict the radial factor $f(r)$, the following assumptions are in agreement with experimental observations in stable or long-lived nuclei [9]: Spin-orbit levels with spin $\boldsymbol{s}$ parallel to $\boldsymbol{l}$ are shifted to lower energies, while levels with anti-parallel spin and orbital angular momentum are shifted upwards. The shift of the energy levels, which is proportional to $f(r)$, decreases with increasing radial quantum number n and increasing orbital radius, but increases with orbital angular momentum since the splitting is proportional to $(2l + 1)$.

In order to completely characterize an energy level, the total angular momentum j must be specified additionally to n and l. For $l > 0$ the (n, l) level is split up by the spin-orbit coupling to the $(n, l, j = l + 1/2)$ and the $(n, l, j = l - 1/2)$ levels.

For a level of given l, first the $2j+1 = 2l+2$ states with $j = l+1/2$ are filled with one nucleon each before the $2j + 1 = 2l$ states with $j = l - 1/2$ are filled. With this spin-orbit coupling of the right size introduced, the magic numbers 28, 50, 82 and 126 can be reconstructed while the lower magic numbers are unaffected.

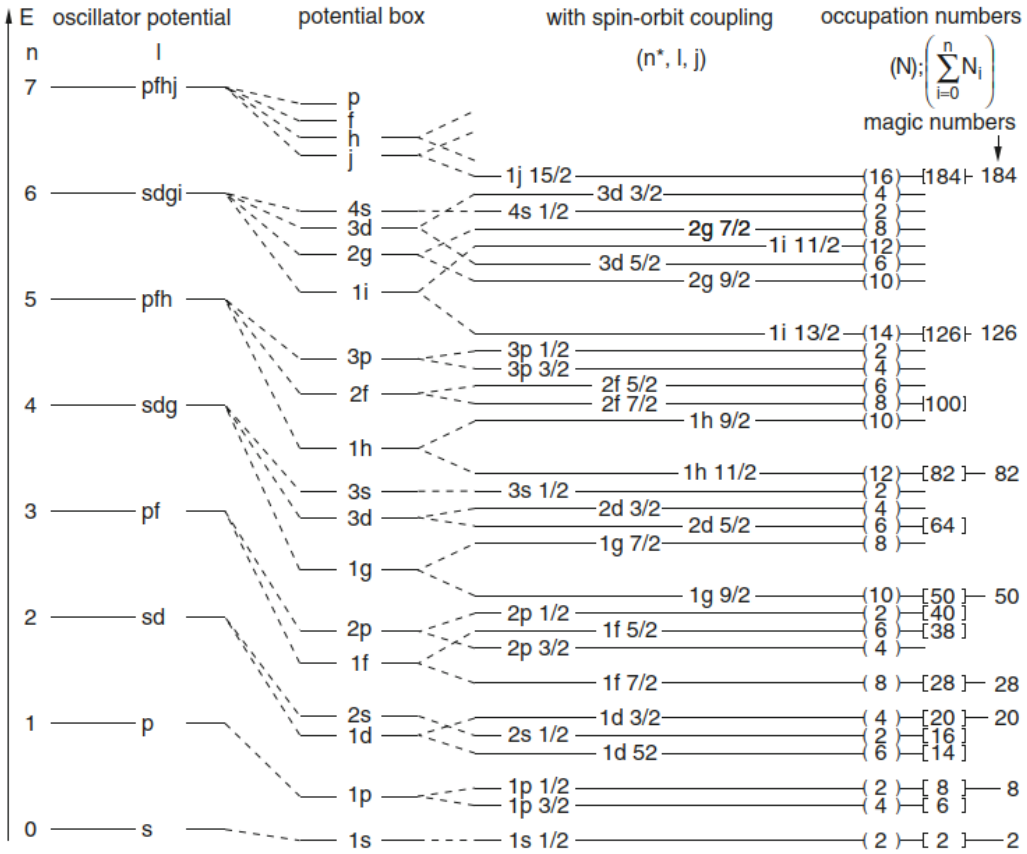

Figure 2.3: Single-particle energy level scheme obtained using a harmonic oscillator potential or a square well (potential box) as nuclear potential $V(r)$. Spin-orbit coupling leads to a splitting of the levels, producing the shell gaps associated with the magic numbers. Figure taken from [50]. Reproduced with permission from Springer Nature.

The energy levels obtained from calculations including the spin-orbit coupling are plotted in Fig. 2.3. A group of levels separated from other levels by a large energy gap is called a *nuclear shell*. The precise order of the levels within the shells depends on the exact nuclear potential and on the strength of the spin-orbit coupling.

Apart from the perfect prediction of the magic numbers, another powerful feature of the nuclear shell model is, that the resulting effective nuclear potential of completely filled (closed) shells and levels is spherically symmetric. In the case of only one missing nucleon (*hole*) from an orbit or only one single nucleon (*particle*) in a level, the nuclear properties (like spin, parity) are exclusively defined by this single particle or hole.

For more than one particle or hole in a nuclear level, the total angular momenta of the individual nucleons in the incompletely filled orbit couple to the nuclear spin $\boldsymbol{I}$. Due to the various different coupling possibilities, the determination of the ground state configuration becomes more elaborate, the more particles and holes are involved.

The examination of empirical data revealed a set of coupling rules [9], helping to identify ground state configurations of nuclei:

- The ground sate of even-even nuclei have zero nuclear spin and even parity.
- The ground state properties of odd-even nuclei are defined by the odd-type nucleons only.
- The ground state spin of the majority of odd nuclei are defined by the quantum number j of the last unpaired nucleon.

2.1.2 Excited Nuclear States

Nuclei can also exist as excited states, where one or more nucleons populate a higher nuclear energy level. These excited nuclei have typical lifetimes τ_{exc} in the range of picoseconds or less, before they decay to the ground state usually by the emission of γ-radiation (photons).

A transition of an excited nuclear state of spin $\boldsymbol{I}_{\mathbf{exc}}$ to the ground state of spin $\boldsymbol{I}_{\mathbf{gs}}$ causes a change of the nuclear spin. Due to angular momentum conservation, the emitted photons must carry a total angular momentum $\boldsymbol{L} = \boldsymbol{I}_{\mathbf{exc}} - \boldsymbol{I}_{\mathbf{gs}}$.

The electromagnetic field emitted in the γ-decay can be classified by a multipole expansion in the angular momentum number L, with multipolarity 2^L. While there are no monopole transitions ($L = 0$), the transition probability decreases with increasing values of L, i.e., the lifetime of the excited state increases.

Due to symmetry selection rules, also the parity Π (the behavior under reflection, $+1$ even parity or -1 odd parity) of the energy levels of a transition influences the lifetime of an excited state. The parity change for electric multipole transitions is $\Delta\Pi = (-1)^L$ and for magnetic multipole transitions it is $\Delta\Pi = (-1)^{L+1}$. It defines which multipole transitions are allowed, e.g., for a dipole transition ($L = 1$) with the same parity in the excited and ground state

($\Delta\Pi = +1$), the electric dipole transition is forbidden, as $(-1)^L = -1$ while the magnetic dipole transition is allowed ($(-1)^{L+1} = +1$).

Excited nuclei of longer lifetimes (nanoseconds up to years) are called *isomers*. Forbidden dipole or quadrupole transitions can cause the long lifetimes. This is often the case for low-lying excited states which need a large spin change for the decay to the nuclear ground state. Therefore, the unique-parity intruder states of high spin are good candidates to form isomers as they are e.g. observed in Cd, Sn and Pb. Isomers with a lifetime of at least a few hundreds of milliseconds can be investigated by the use of collinear laser spectroscopy, as it has been done for several lead isomers within this work.

2.1.3 State-Dependent Nuclear Properties

Despite the very general and qualitative assumptions about the nuclear interaction, the nuclear shell model predicts nuclear properties remarkably well. From a laser spectroscopic point of view, the nuclear charge radius and the nuclear magnetic dipole and electric quadrupole moments are the most important ones since these can be extracted from the optical spectrum. They are introduced in the following sections.

Nuclear Charge Radius

The nuclear charge radius is a measure for the size of the nuclear charge distribution and has to be distinguished from the nuclear matter radius. Following the liquid-drop model, the nuclear charge radius can be approximated by

$$R = A^{1/3} R_0, \tag{2.4}$$

with the empirical constant R_0 varying between 1.12 and $1.24\,\mathrm{fm}$ [54], depending on the exact model.

It is a good approximation for spherical nuclei but for deformed nuclei deviations have to be expected. In these cases the 'size' of the nuclear charge distribution $\rho(\boldsymbol{r})$ strongly depends on the actual form of $\rho(\boldsymbol{r})$.

In this work, the root-mean-square (rms) nuclear charge radius is used as a measure of the size of the nucleus, which depends on the nuclear charge distribution through [55]

$$\sqrt{\langle r_c^2 \rangle} = \sqrt{\frac{\int r^2 \rho\,(\boldsymbol{r})\,\mathrm{d}^3 r}{\int \rho\,(\boldsymbol{r})\,\mathrm{d}^3 r}}. \tag{2.5}$$

With this definition, the rms nuclear charge radius can be derived from form factors measured

in elastic electron scattering experiments. The resulting value of the rms nuclear charge radius depends on the model parameters chosen for the determination of $\rho(\boldsymbol{r})$.

A model-independent measure of the size of the nuclear charge distribution is the Barret equivalent radius $R_{k\alpha}$ [55], which is obtained from muonic x-ray spectroscopy. It is related to the rms nuclear charge radius by

$$\sqrt{\langle r_c^2 \rangle} = \frac{R_{k\alpha}}{V_2}. \tag{2.6}$$

with the V_2-ratio obtained from elastic electron scattering. By combining the information gained from muonic x-ray spectroscopy and electron scattering experiments, a model independent rms nuclear charge radius can be determined. For both methods stationary targets are required, restricting the application to long-lived isotopes. A powerful method to investigate the nuclear charge radius and the nuclear moments of short lived nuclei is collinear laser spectroscopy, although in recent years, advancements have also enabled the investigation of short-lived isotopes using electron scattering [56].

Magnetic Dipole Moment

The moving charges within the nucleus give rise to the magnetic moment of the nucleus. Additionally, the spin induced magnetic fields of the nucleons contribute. The operator of this magnetic dipole moment can be written as

$$\boldsymbol{\mu} = \sum_{i=1}^{A} \{\boldsymbol{l}_i g_l + \boldsymbol{s}_i g_s\} \mu_N \tag{2.7}$$

where $\boldsymbol{l}_i$ and $\boldsymbol{s}_i$ are the angular momentum and the spin of the i^{th} nucleon. The orbital gyromagnetic factor (g-factor) for protons is $g_l = 1$ and for neutrons it is zero. The spin g-factor for free protons is $g_s = 5.586$ [57] and for free neutrons $g_s = -3.826$ [57].

The observable magnetic dipole moment μ_I is the largest possible value of the z-component of $\boldsymbol{\mu}$. It is typically given in units of the nuclear magneton $\mu_N = e\hbar/(2m_p)$ with the elementary charge e and proton mass m_p and can be calculated from the nuclear spin I by

$$\frac{\mu_I}{\mu_N} = gI = \left(g_l \pm \frac{g_s - g_l}{2l+1}\right) I \tag{2.8}$$

where $+$ applies for $\boldsymbol{s}$ and $\boldsymbol{l}$ parallel and $-$ for $\boldsymbol{s}$ and $\boldsymbol{l}$ antiparallel, and g is the nuclear g-factor. If the magnetic moment is calculated by Eq. (2.8) with g_s and g_l owed to the last uncoupled nucleon exclusively and with $I = j$ of the incompletely filled orbit, μ is called the single particle moment μ_{sp}, also called Schmidt value, and the corresponding curves connecting the Schmidt

values for different single-particle angular momenta are the *Schmidt lines*. In reality the magnetic moment of a nucleus is also influenced by polarization effects (see below). Therefore the single-particle moments are rarely observed. Still the Schmidt lines give the upper and lower limits of possible nuclear magnetic dipole moments.

To account for the deviations from the Schmidt values an effective g-factor instead of the spin g-ratio can be used to calculate the nuclear magnetic dipole moment. In the tin region, e.g. for palladium, it was observed to be around $g_{s,\text{eff}} = 0.6 \cdot g_s$ for protons and neutrons [58, 59, 60], i.e. for neutrons $g_{s,\text{eff}} = -2.298$, while for the Pb region, the effective spin g-factor for neutrons can be fitted to $g_{s,\text{eff}} = 0.9 \cdot g_s = -3.447$ [61].

Electric Quadrupole Moment

The classical definition of the quadrupole tensor of a continuous system with charge distribution $\rho(\boldsymbol{r})$ is

$$Q_{ij} = \int \rho(\boldsymbol{r}) \left(3r_i r_j - |\boldsymbol{r}|^2 \delta_{ij}\right) \mathrm{d}^3 r \tag{2.9}$$

where the indices i and j indicate the Cartesian space coordinates x, y, z.

In the nuclear shell model, closed shell nuclei are spherically symmetric. Nucleons outside a closed shell can lead to a deformation of the nuclear charge distribution. These deformed nuclei carry an intrinsic electric quadrupole moment. With the body-fixed spherical coordinates (r', θ', ϕ') the matrix elements of the intrinsic electric quadrupole tensor are [62]

$$Q_{2\mu}^{\text{int}} = \int \rho(\boldsymbol{r'}) r'^2 Y_{2\mu}(\theta', \phi') \, \mathrm{d}^3 r' \tag{2.10}$$

with the charge distribution $\rho(\boldsymbol{r})$ and the spherical harmonics $Y_{\lambda\mu}(\theta, \phi)$. The intrinsic quadrupole moment Q_0 can then be calculated by

$$eQ_0 = \langle K | \, Q_{20}^{\text{int}} \, | K \rangle \tag{2.11}$$

with the intrinsic rotational state $|K\rangle$ (K is the projection of the nuclear spin $\boldsymbol{I}$ onto the body-fixed axis 3 and therefore $K = I, I-1, ..., -I$)[63].

In the nuclear shell model with a single proton (hole) outside a filled orbit, the completely filled levels with $|\sum j| = 0$ are assumed to lead to a spherical charge distribution. The quadrupole moment is therefore only defined by the odd proton (hole). According to Eq. (2.9) and (2.11) the intrinsic quadrupole moment Q_{sp} due to a single proton is defined by its total angular momentum j only [9]

$$Q_{\text{sp}} = -\langle r_j^2 \rangle \frac{2j-1}{2(j+1)} \tag{2.12}$$

with the ms radius $\langle r_j^2 \rangle$ of the particle in orbit of angular momentum j.

For an odd number λ of protons in an orbit of angular momentum j and with normal coupling ($I = j$) the intrinsic quadrupole moment of the nucleus depends on the occupation number λ. Owing to $Q_{\text{sp}}^{m_j} = Q_{\text{sp}}^{-m_j}$ it can be calculated from the single particle quadrupole moment [9] as

$$Q(\lambda) = Q_{\text{sp}} \left(1 - \frac{2(\lambda - 1)}{2j - 1} \right). \tag{2.13}$$

The resulting quadrupole moment is negative for less than half filled orbits, positive for more than half filled orbits and zero for half filled orbits ($\lambda = {}^{(2j+1)}/_{2}$).

Deviations from this expectation value of Q have been observed when mixing of configurations with the same j and the same parity are possible. This configuration mixing can be semi-theoretically be described by Rainwater's model. In this model, the core, consisting of all nucleons but the last unpaired particles, is assumed to be spherically symmetric but soft. It can therefore be deformed by the interaction with the unpaired particles. This deformed core contributes additionally to the quadrupole moment of the nucleus. The softness, or deformability, of the core can be regarded as a measure of the number of possible configurations for the ground state.

Rainwater's model does not only describe quadrupole moments due to configuration mixing, but it also explains the electric quadrupole moments of even-proton-odd-neutron nuclei (odd-N nuclei). Their quadrupole moment cannot arise from the last odd neutron only, as the neutron does not carry electric charge. Rather it has to arise from the non-spherical charge distribution of the deformed core. The single particle quadrupole moment in Eq. (2.12) can be altered to

$$Q_{\text{sp}} = -\langle r^2 \rangle \frac{2j - 1}{2(j + 1)} q_{\text{eff}} \tag{2.14}$$

where q_{eff} is the effective charge of the unpaired neutron derived from fitting to experimental data.

Equation (2.13), with λ replaced by the number of neutrons in a state of angular momentum j, also holds for these odd-N nuclei. For an odd number of protons *and* neutrons, the relation can be generalized according to the seniority scheme [64] to

$$Q(n, \nu) = \frac{2j + 1 - 2n}{2j + 1 - 2\nu} Q_{\text{sp}}, \tag{2.15}$$

where the seniority ν is the number of unpaired nucleons and n is the number of particles occupying partially filled levels of angular momentum j.

Until now the nucleus has been considered in its body-fixed reference frame, with the nuclear spin $\boldsymbol{I}$ rotating around the symmetry axis of the nucleus. In the reference frame of the

observer (laboratory frame), the symmetry axis of the nucleus can also rotate around the z-axis of the laboratory frame. This can distort the time-averaged charge distribution, that can be observed experimentally. The intrinsic quadrupole tensor can be transformed using the Wigner D-Matrix $D^2_{m\mu}(\omega)$ to the laboratory frame, resulting in

$$\begin{aligned} Q_{2m} &= \sum_{\mu=-2}^{2} Q^{\text{int}}_{2\mu} D^2_{m\mu}(\omega) \\ &= \frac{e}{2} Q_0 Y_{2m}(\theta, \phi) \sqrt{\frac{16\pi}{5}} \end{aligned} \tag{2.16}$$

where $\omega = (\phi, \theta, \psi)$ is the orientation of the body fixed system in the laboratory frame (see [63] for more details). In the last expression of Eq. (2.16) axial symmetry of the nuclear charge distribution is assumed.

The observable static, or spectroscopic, quadrupole moment Q_s is given by the diagonal elements of the reduced matrix element from the Wigner-Eckart theorem [63]

$$\langle K I_1 | \, | Q_2 | \, | K I_2 \rangle = \sqrt{(2I_1 + 1)} \, \langle I_1 K; 20 | I_2 K \rangle \, e Q_0. \tag{2.17}$$

where the coupling of the angular momenta in the intrinsic frame is represented by the vector addition coefficients $\langle I_1 K; 20 | I_2 K \rangle$, also called Glebsch-Gordon coefficients. The static quadrupole moment can therefore be calculated from the intrinsic moment by

$$\begin{aligned} Q_{\text{s}} &= \langle IK20 | IK \rangle \, \langle II20 | II \rangle \, Q_0 \\ &= \frac{3K^2 - I(I+1)}{(I+1)(2I+3)} Q_0 \end{aligned} \tag{2.18}$$

The case $I = K$ usually applies for the the ground state of a nucleus [63]. Therefore one obtains for the ground-state static quadrupole moment

$$Q_{\text{s}} = \frac{I}{I+1} \frac{2I-1}{2I+3} Q_0 \tag{2.19}$$

and $|Q_{\text{s}}|$ is in any case smaller than the intrinsic $|Q_0|$.

From Eq. (2.19) one can see that spin-0 and spin-$1/2$ nuclei do not have a spectroscopic quadrupole moment even if the nucleus is intrinsically deformed and has an intrinsic quadrupole moment Q_0. More visually spoken: In experiments only the quadrupole moment of the time-averaged charge distribution can be determined. So the quadrupole moment can only be observed, if the intrinsic quadrupole moment can orientate itself with respect to a nuclear axis. Spin-0 nuclei do not have a preferred axis and are oriented randomly. Therefore, their

quadrupole moment cannot be measured. Also the time-averaged charge distribution of a spin-$^1/_2$ nucleus is spherical symmetric. So only for $I \geq 1$ the nuclear quadrupole moment can be observed.

Consequences The polarization of the core does have a strong influence on the nuclear magnetic dipole moment. As the core is deformed and its potential for the odd nucleon is not spherically symmetric, the angular momentum j of the odd particle is not a good quantum number anymore, only its projection m_j onto the symmetry axis [9]. The core's and the particle's angular momenta couple such that the total nuclear magnetic moment cannot be expected to coincide with the Schmidt values. The expected deviation depends on the strength of the core-particle coupling. The problem can also be treated in the following [62] way: The spin-dependent part of the nuclear force favors LS coupling over jj coupling, which leads to a mixing of configurations with different j (but same parity), causing the deviation of the magnetic dipole moment from the Schmidt value.

An important consequence of core deformation is, that it can even lead to an intrinsic quadrupole moment for even-even nuclei, although it is not directly observable as the total nuclear spin is zero. But it affects the observed nuclear charge distribution, and can therefore have an impact on measured nuclear charge radii.

For a prolate or oblate nucleus the position of the surface of the nuclear charge distribution depends on the polar angle θ and can be described by the angular-dependent nuclear charge radius

$$R(\theta) = R_0 \left(1 + \beta \cdot Y_{20}(\theta) - \frac{1}{4\pi}\beta^2\right) \tag{2.20}$$

with the deformation parameter β and the spherical harmonic Y_{lm}, which is independent of the azimuthal angle ϕ for $m = 0$. R_0 is the radius of a nucleus described as a spherical liquid drop. Higher orders of β were omitted in Eq. (2.20).

For triaxially deformed nuclei the angular-dependent nuclear charge radius also depends on the azimuthal angle ϕ and up to order α^2 it can be expressed by [63]

$$\begin{aligned} R(\theta,\phi) = R_0 \Bigg(1 &+ \sum_{l=2}^{\infty}\sum_{m=-l}^{l} \alpha_{lm} Y_{lm}^*(\theta,\phi) \\ &- \frac{1}{4\pi}\sum_{l=2}^{\infty}\sum_{m=-l}^{l} |\alpha_{lm}|^2 \Bigg) \end{aligned} \tag{2.21}$$

where the multipole parameters α_{lm} now characterize the deformed surface. Usually only the quadrupole contributions are of relevance and their multipole parameters are often expressed by the deformation parameter β and triaxiality parameter γ as $\alpha_{20} = \beta\cos\gamma$ and $\alpha_{22} =$

$\frac{\beta}{\sqrt{2}} \sin\gamma$.

With Eq. (2.5) this decomposes the mean-square nuclear charge radius into a spherical and a deformed contribution

$$\langle r_c^2 \rangle = \langle r_0^2 \rangle + \langle r_{\text{def}}^2 \rangle = \langle r_0^2 \rangle + \langle r_0^2 \rangle \frac{5}{4\pi} \sum_{l=2}^{\infty} \langle \beta_l^2 \rangle \tag{2.22}$$

where in the second part of the equation axial symmetry is assumed and higher orders of β are neglected.

With the deformation parameter β and Eq. (2.9), the intrinsic quadrupole moment can be expressed in terms of β by

$$Q_0 \approx \frac{3}{\sqrt{5\pi}} Z R_0^2 \beta \left(1 + \frac{2}{7} \sqrt{\frac{5}{\pi}} \beta \right), \tag{2.23}$$

or for triaxial shapes by

$$Q_0 \approx \frac{3}{\sqrt{5\pi}} Z R_0^2 \beta \left(\cos\gamma + \frac{2}{7} \sqrt{\frac{5}{\pi}} \beta \cos^2\gamma - \sqrt{\frac{5}{4\pi} \frac{\beta}{2} \sin^2\gamma} \right). \tag{2.24}$$

2.1.4 Ab initio calculations

The nuclear structure is is governed by the nuclear forces, i.e. strong interactions between all nucleons and Coulomb interactions between protons. Therefore, ab initio many-body calculations aim for a microscopic understanding of nuclear structure by solving the Schrödinger equation for all constituents and the interactions between them. The strong interaction is governed by the quark-gluon dynamics within the nucleons and makes a low-energy perturbative approach to describe the nucleus as a quark-gluon system impossible.

Chiral Effective Field Theory

Chiral effective field theory (EFT) makes use of the fact that small-distance details (like quark-gluon dynamics within a nucleon) are not resolved when probing the nucleus at low energies [65, 66]. Therefore one can introduce low-energy degrees of freedom and any contributions to free-space inter-nucleon interactions are treated in a power counting expansion. The relevant degrees of freedom depend on the energy scale, at which the nucleus is probed.

In chiral EFT only protons, neutrons and pions are considered, setting the breakdown energy to $\Lambda_b \approx 500\,\text{MeV}$ [67]. The power counting of nuclear interactions is performed in Ω/Λ_b with the typical momentum Ω of the interacting system. It leads at leading order (LO) Ω^0/Λ_b^0 to two

contributions: the two-nucleon (2N) contact interaction and the one-pion exchange between two nucleons. Three-body interactions only start to appear at next-to-next-to-leading-order (N^2LO). The contact interaction contributions depend on running coupling parameters which depend on the resolution scale Λ, introduced to regularize the theory. The coupling parameters are nowadays fit to experimental data.

In-Medium Similarity Renormalization Group

Low-energy and high-energy components of nuclear interactions can be systematically decoupled from each other by (similarity) renormalization group ((S)RG) techniques [68], while at the same time low-energy observables are conserved. Such a decoupling is performed by a unitary transformation, which depends on a flow parameter or the resolution scale. It improves the convergence of many-body calculations when truncating the basis in which the calculations are performed.

For higher mass numbers the in-medium similarity renormalization group (IMSRG) [69] is a well-established method to reduce the computational costs of calculating eigenvalues and eigenstates. For this technique the Hamiltonian is normal-ordered with respect to a reference state. While the normal-ordered zero-body contribution of the Hamiltonian describes the energy of the reference state, the normal-ordered many-body contributions describe the residual interactions beyond, including n-particle-n-hole (npnh) excitations. Applying the SRG technique to this normal-ordered Hamiltonian transforms it to a block-diagonal form with all considered particle-hole excitation state admixtures already included in the eigenvalue of the 0p0h reference state. By a suitable choice of the used reference state, the main contributions from 3N interactions can already be incorporated at computational costs of 2N interactions [67].

The single-particle basis can additionally be partitioned into core, valence and beyond-valence states and the operators can be normal-ordered with respect to the closed-shell core Slater determinant. The valence state can be decoupled from non-valence states by IMSRG and the eigenvalue problem is then solved with Shell-Model calculations. This approach is called valence-space IMSRG (VS-IMSRG) [70].

Over the last decade ab initio calculations progressed dramatically. While in 2010 only $A \leq 10 - 20$ nuclei were accessible by ab initio calculations, the limit was pushed up to $A \leq 80 - 100$ until 2020[71]. Figure 2.4 shows the nuclei accessible by ab initio theory until 2020. During the last four years further progress has been made to the magic lead isotopes at $Z = 82$ [72, 73] while the mid-shell region below $Z = 50$ around palladium is still not reached yet.

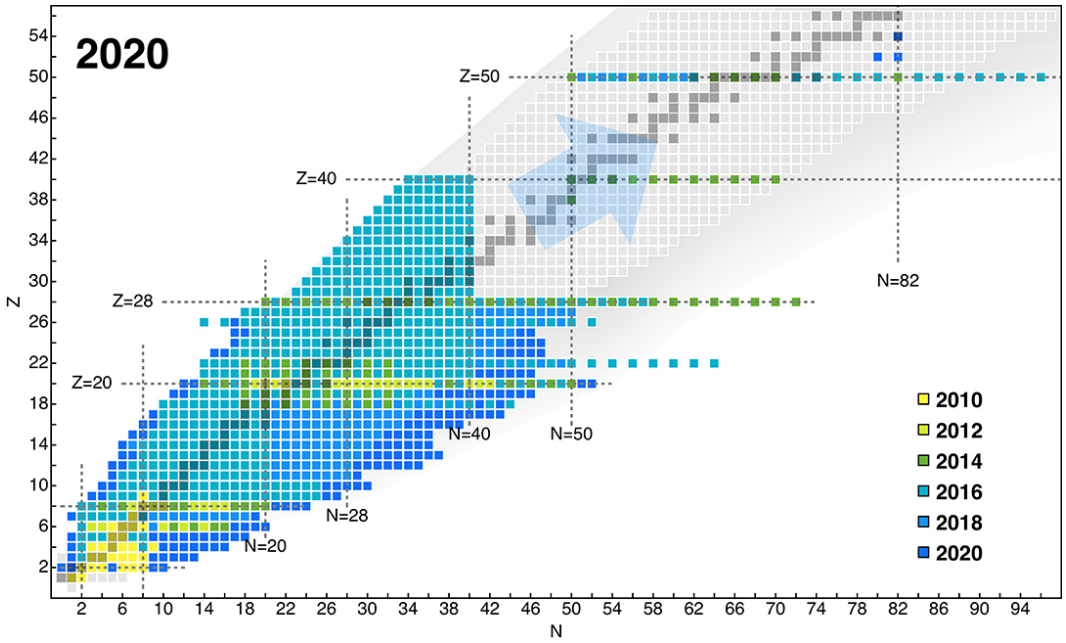

Figure 2.4: Nuclei accessible by ab-inito calculations (status 2020). Figure taken from [71]. Used under CC by 4.0 with permission from Heiko Hergert.

2.1.5 Energy Density Functionals

To extend calculations to the higher-mass regions nuclear energy density functional theory (EDF) is a powerful tool. In EDF the calculations for a nucleus consisting of A particles are performed based on particle densities

$$n(\boldsymbol{r}) = \sum_{i=1}^{A} |\varphi_i(\boldsymbol{r})|^2 \tag{2.25}$$

as degrees of freedom, instead of many-body wave functions $\psi(\boldsymbol{r}_1, \boldsymbol{r}_2, ..., \boldsymbol{r}_A)$ or single particle (orbital) wave functions $\varphi_i(\boldsymbol{r})$, as it is done in ab initio calculations.

EDF is based on the Hohenberg-Kohn theorem [74]. It says, that the functional

$$E[n] \equiv F[n(\boldsymbol{r})] + \int v(\boldsymbol{r}) n(\boldsymbol{r}) \, \mathrm{d}^3 r \tag{2.26}$$

has its minimum at the ground-state energy of the system, described by the Hamiltonian $\hat{H} = \hat{F} + \hat{V}_{\text{ext}}$, where the external potential $\hat{V}_{\text{ext}}$ is associated with $v(\boldsymbol{r})$, and that $F[n(\boldsymbol{r})]$ is universal and exists for any $v(\boldsymbol{r})$. In fact, the functional F depends on the kind of fermions, i.e., on the nucleon-nucleon interaction, and is independent of $v(\boldsymbol{r})$.

Kohn and Sham present an often used scheme [75], where

$$F\left[n\right] \equiv T_s\left[n\right] + G_{NN}[n] + E_{xc}\left[n\right] \tag{2.27}$$

$$G_{NN}[n] = \int n(\boldsymbol{r}) n(\boldsymbol{r}') V_{NN}(|\boldsymbol{r} - \boldsymbol{r}'|)\, \mathrm{d}^3 r' \tag{2.28}$$

$$E_{xc}[n] = \int n(\boldsymbol{r}) \epsilon_{xc}[n(\boldsymbol{r})]\, \mathrm{d}r \tag{2.29}$$

with the kinetic energy T_s of a system of non-interacting nucleons of density $n(\boldsymbol{r})$, the direct nucleon-nucleon interaction energy G_{NN} (Hartree energy) and the so-called exchange and correlation energy E_{xc} of an interacting system of density $n(\boldsymbol{r})$ with the exchange and correlation energy density ϵ_{xc}. Within this scheme one can use the variational principle to derive the Kohn-Sham equations from Eq. (2.26),

$$\left(-\frac{1}{2m}\nabla^2 + V_{KS}[n](\boldsymbol{r})\right)\varphi_i = \epsilon_i \varphi_i \tag{2.30}$$

with the orbital wave functions φ_i and their single-particle energies ϵ_i and the potential V_{KS} depending on the nucleon-nucleon interaction, the exchange and correlation energy density and the external potential. Eq. (2.30) is solved self-consistently, starting with an assumed particle density $n_0(\boldsymbol{r})$, from which V_{KS} is constructed. From Eq. (2.30) and (2.25) a new $n(\boldsymbol{r})$ is found. This process is iterated until the ground state energy (2.26) converges.

For the calculations, different methods exist of which the Hartree-Fock Bardeen-Cooper-Schrieffer (BCS) and the Hartree-Fock Bogoliubov (HFB) methods are the most common. The BCS framework leads to a nucleon density $n(\boldsymbol{r})$ with a gas-like character for small binding energies, while the HFB framework results in a localized nucleon density [15].

A large variety of energy functionals have been developed. For the discussion of the results of this work, the widely used Skyrme functionals and Fayans functionals are relevant. They especially differ in the way how nucleon pairing is established. Any used energy density functional is a phenomenological description of the system and the free coupling constants of the functionals have to be tuned to (selected) experimental data. The impact of different energy-density functionals and of different observables used for tuning the coupling constants is investigated in [13].

2.2 Atomic Theory

The nuclear properties described above are investigated in this work using laser spectroscopy. The following section describes the atomic structure, how it is related to nuclear properties

and how the nuclear observables can be extracted from atomic spectra.

2.2.1 Atomic Structure (Fine Structure)

Similar as the nuclear shell model describes the nuclear structure, atomic structure is well described by a set of discrete energy levels occupied by the atomic electrons. Each electronic orbit is characterized by a set of quantum numbers. Non-relativistic quantum mechanics, assuming an attractive Coulomb potential, predicts levels characterized by the principle quantum number n and the orbital angular momentum quantum number l.

In contrast to the nuclear force, the Coulomb force allows for a fundamental description within the Schrödinger equation and relativistic corrections. It enables the ab initio calculation of few-electron systems with high precision. For the multi-electron systems investigated within this work, approximations or semi-empirical approaches are necessary.

For a multi-electron system, the orbital angular momenta of the individual electrons couple to $\boldsymbol{L} = \sum_i \boldsymbol{l}_i$. As electrons also have a quantized spin of $\boldsymbol{s} = \hbar/2$, these spins also couple to the total spin $\boldsymbol{S} = \sum_i \boldsymbol{s}_i$. The eigenstates of such a multi-electron system are usually labeled by ${}^{2S+1}L$ [76].

Analogously to the LS-coupling in the nuclear shell model, the total orbital angular momentum and total spin couple to a total angular momentum $\boldsymbol{J} = \boldsymbol{L} + \boldsymbol{S}$, splitting and shifting the electronic energy levels by $F_{\mathrm{LS}}\langle \boldsymbol{L} \cdot \boldsymbol{S} \rangle$ [76], with the coupling strength F_{LS}.

The spin-orbit coupling can be expressed by

$$E_{\mathrm{LS}} = \frac{F_{\mathrm{LS}}}{2}[J(J+1) - L(L+1) - S(S+1)], \tag{2.31}$$

with the preserved quantum numbers L, S and J, and the eigenstates are labeled by ${}^{2S+1}L_J$.

In heavier atoms, ls-coupling is often stronger than ll-coupling and ss coupling. In these cases one speaks of jj-coupling, where the total angular momenta $\boldsymbol{j}$ of the individual electrons couple to the total angluar momentum of the atom $\boldsymbol{J} = \sum_i \boldsymbol{j_i} = \sum_i (\boldsymbol{l_i} + \boldsymbol{s_i})$.

2.2.2 Atomic Transitions

The ground state of an atom corresponds to electrons occupying the lowest possible energy levels. By exchanging energy with their environment, the electrons can be excited into higher lying levels. For an optical transition of an electron to a higher level (excitation), a photon of the required energy is absorbed by the atom. In the same way for an optical transition to a lower (not yet fully occupied) level (decay), a photon is emitted carrying the excess energy. The frequency ν of the involved photon is related to the transition energy by $E = h\nu$.

Transitions between two different principal (n) levels are usually in the order of several eV (hundreds of THz) and excitations can therefore be driven by lasers and the photons from a decay can be observed with common optical detectors. This concept of photon-driven transitions is the basis of laser spectroscopy which is explained in more detail in Sec. 4.

Owing to conservation laws not every transition is allowed. As the bosonic photon can only have spin orientations ± 1 and due to parity the quantum numbers between the initial and final atomic levels can only change by $\Delta l = \pm 1$, $\Delta j = 0, \pm 1$ and $\Delta m_j = 0, \pm 1$ for an electric dipole transition. It should be noted that a transition with $\Delta j = 0$ is forbidden in the case of $j_\mathrm{i} = 0 \rightarrow j_\mathrm{f} = 0$.

2.2.3 Atomic Interaction with the Nucleus

In the simplest approximations the atomic energy levels are derived under the assumption of a point-like nucleus of infinite mass and charge Z, without any further properties. As covered by Sec. 2.1 atomic nuclei have a variety of properties and are not point-like at all. These properties influence the atomic energy levels.

Isotope Shift

If the nucleus' finite size and its finite mass are taken into account, both nuclear characteristics lead to the isotope shift between two isotopes of the same element,

$$\delta\nu^{A,A'} = \nu^A - \nu^{A'}, \tag{2.32}$$

a difference in the transition frequency ν^A of the isotope with mass number A compared to the transition frequency $\nu^{A'}$ of the isotope with mass number A'. The two contributions are called the mass shift and the field shift.

Mass Shift:

Considering the finite nuclear mass M, the binding energy B of an atomic electron depends on the reduced mass of the electron-nucleus system [77]

$$B \propto \frac{m_e M}{M + m_e} \tag{2.33}$$

with the electron mass m_e.

As two isotopes of the same element have different nuclear masses M_A and $M_{A'}$ their atomic

binding energies also show small differences, which can be approximated as

$$B_A - B_{A'} \simeq \frac{m_e(M_A - M_{A'})}{(M_A + me)(M_{A'} + m_e)} . \frac{K_{\text{NMS}}}{m_e} h \tag{2.34}$$

where $K_{\text{NMS}} = \nu_\infty m_e$ and ν_∞ corresponds to the atomic binding energy to a nucleus of infinite mass. This simplified theoretical description only holds for one-electron systems and is called the *normal mass shift* (NMS).

In an atom or ion with more than one electron, correlations between those add an extra shift to the binding energies called *specific mass shift* (SMS). It can be treated as a perturbation and leads in first order to a total mass shift of [77]

$$B_A - B_{A'} \simeq h \frac{M_A - M_{A'}}{(M_A + m_e)(M_{A'} + m_e)} \left(K_{\text{NMS}} + \left\langle \sum_{i,j} \boldsymbol{p}_i \cdot \boldsymbol{p}_j \right\rangle \right) , \tag{2.35}$$

with the momenta $\boldsymbol{p_i}$ of the atomic electrons. The first term in the parentheses represents the NMS and the second term the SMS.

The calculation of the SMS for many-electron systems becomes computational more tedious the more electrons have to be considered. As both the NMS and SMS have the same nuclear-mass dependence, the total mass shift can be written as

$$\delta\nu_{\text{MS}}^{A,A'} = \mu^{A,A'}(K_{\text{NMS}} + K_{\text{SMS}}) = \mu^{A,A'} K_{\text{MS}} \tag{2.36}$$

with the mass-scaling factor

$$\mu^{A,A'} = \frac{M_A - M_{A'}}{(M_A + m_e)(M_{A'} + m_e)} . \tag{2.37}$$

Field Shift:

An electron outside the nuclear region sees a Coulomb potential due to the electric charge of the nucleus, which is the same for all isotopes of the same element. An electron that penetrates the nucleus sees a different (and finite) potential, depending on the nuclear charge distribution. Hence, in such a case the binding potential cannot be simply described by a Coulomb potential of a point-like charge.

This deviation from a Coulomb potential shifts the atomic energy levels. The energy shift is proportional to the electron density at the nucleus, and, thus, depends on the electron orbital. This makes the field shift observable in differences of the transition frequencies. Owing to this proportionality $s - p$ transitions are particularly sensitive to field shifts. The isotope shift

caused by the finite-nucleus-size effect can be written as [78]

$$\delta\nu_{\mathrm{FS}}^{A,A'} = -\frac{2\pi}{3h} Z e^2 \Delta\rho_e(0) \lambda^{A,A'} = F\lambda^{A,A'} \tag{2.38}$$

where $\Delta\rho_e(0) = \rho_e(0)^u - \rho_e(0)^l$ is the difference between the electron densities at the nucleus of the upper and lower atomic states.

$$\lambda^{A,A'} = \delta\langle r^2\rangle^{A,A'} + (C_2/C_1)\delta\langle r^4\rangle^{A,A'} + (C_3/C_1)\delta\langle r^6\rangle^{A,A'} + ... \tag{2.39}$$

is called the nuclear parameter and contains the desired information about the nuclear charge radii. The Seltzer coefficients C_n are tabulated in [79, 80, 81].

Separation of Mass and Field Shifts

Optical measurements of the isotope shift are always the sum of the mass and field shift

$$\begin{aligned} \delta\nu^{A,A'} &= \mu^{A,A'} K_{\mathrm{MS}} + F\lambda^{A,A'} \\ &\approx \mu^{A,A'} K_{\mathrm{MS}} + F\delta\langle r^2\rangle^{A,A'}. \end{aligned} \tag{2.40}$$

They can be separated by a so called King-plot procedure. For this, Eq. (2.40) is divided by $\mu^{A,A'}$ leading to

$$\widetilde{\delta\nu}^{A,A'} = K_{\mathrm{MS}} + F\widetilde{\delta\langle r^2\rangle}^{A,A'} \tag{2.41}$$

where tilde includes the division with the mass-scaling factor. It reveals a linear dependency of the modified isotope shift $\widetilde{\delta\nu}^{A,A'}$ on the modified differential ms nuclear charge radius $\widetilde{\delta\langle r^2\rangle}^{A,A'}$. A linear fit to three or more experimental measurements of $\widetilde{\delta\nu}^{A,A'}$ and $\widetilde{\delta\langle r^2\rangle}^{A,A'}$ yields the mass shift factor K_{MS} as the offset of the linear function and the field shift factor F as the slope of the fit function.

In this work, nuclear charge radii of stable isotopes from electron scattering experiments and muonic X-ray spectroscopy are combined with optical isotope shift measurements to determine K_{MS} and F. The differential ms nuclear charge radii of radioactive isotopes are then calculated from optical isotope shifts by

$$\delta\langle r^2\rangle^{AA'} = \frac{\delta\nu^{AA'} - K_{\mathrm{MS}}\mu^{AA'}}{F}. \tag{2.42}$$

It should be noted that Eqs. (2.41)-(2.42) are only (but very good) approximations, since higher-order terms are neglected. This is completely sufficient for the extraction of charge radii in formation of medium-mass and heavy isotopes. However, a closer look is required if one wants to look for, e.g., new bosons contributing to isotope shifts as recently proposed by

Berengut et al.[82] and has been done in several recent works [83, 84, 85, 86, 87].

Hyperfine Splitting

The field shift is the correction of only the monopole contribution $\sim {}^{1}/_{r}$ of the electromagnetic interaction between the nucleus and the atomic electrons for $r < R_{\text{nuc}}$. The total electromagnetic interaction between the two components can be described by a multipole expansion, where owing to parity and time reversal conservation only even electric and odd magnetic multipoles contribute [78].

The magnetic dipole contribution describes the interaction of the magnetic dipole moment $\boldsymbol{\mu}_I$ of the nucleus with spin $\boldsymbol{I}$ with the magnetic field $\boldsymbol{B}_{\text{e}}$ at the nucleus' position created by the atomic electrons. This interaction shifts the binding energy of an atomic configuration with total angular momentum $\boldsymbol{J}$ by [76]

$$\begin{aligned}\Delta E_{\text{HFS}-\text{mag}} &= -\langle JJ|\, \boldsymbol{\mu}_I \cdot \boldsymbol{B}_{\text{e}}\, |JJ\rangle \\ &= -g_I \mu_N \langle JJ|\, \boldsymbol{I} \cdot \boldsymbol{B}_{\text{e}}\, |JJ\rangle \\ &= -g_I \mu_N B_{\text{e},J} \langle JJ|\, \boldsymbol{I} \cdot \boldsymbol{J}\, |JJ\rangle\end{aligned} \tag{2.43}$$

where in the last equation the Wigner-Eckart theorem was applied, i.e., $\langle JM_J|\, \boldsymbol{B_e}\, |JM_J\rangle \propto \langle JM_J|\, \boldsymbol{J}\, |JM_J\rangle$. The scalar product of the nuclear spin and total angular momentum is understood as a coupling to $\boldsymbol{F} = \boldsymbol{I} + \boldsymbol{J}$ and the energy shift can be written as [88]

$$\Delta E_{\text{HFS}-\text{mag}} = \frac{A}{2} K, \quad K = F(F+1) - I(I+1) - J(J+1) \tag{2.44}$$

with the magnetic dipole hyperfine constant

$$A_J = \frac{g_I \mu_N B_{\text{e},J}}{\sqrt{J(J+1)}}. \tag{2.45}$$

Equation (2.44) shows a level splitting into the hyperfine (HF) states characterized by the quantum number $F = |I - J|, ..., |I + J|$ and is called hyperfine splitting (HFS). The eigenstates of the hyperfine interaction are described by the set of $(IJFM_F)$ quantum numbers.

The next order of the electromagnetic interaction between electron and nucleus is the electric quadrupole contribution. It describes the interaction of the static nuclear electric quadrupole moment Q_{s} with the gradient of the electric field ${}^{\partial^2 V_{\text{e}}}/_{\partial z^2}$ of the electrons at the nucleus' position. This interaction leads, without any further splitting, to an additional shift of [78]

$$\Delta E_{\text{HFS}-\text{el}} = \frac{B}{4} \frac{\frac{3}{2}K(K+1) - 2J(J+1)I(I+1)}{J(2J-1)I(2I-1)}, \tag{2.46}$$

with

$$B = eQ_\mathrm{s} \langle JJ| \frac{\partial^2 V_\mathrm{e}}{\partial z^2} |JJ\rangle \tag{2.47}$$

and the z-axis corresponding to the electronic total angular momentum. As Q_s is the time average of the intrinsic quadrupole moment Q_0 (see Sec. 2.1.3), spin-0 or spin-$^1/_2$ nuclei show no electric contribution to the HFS.

Similar to the selection rules in fine-structure spectra discussed in Sec. 2.2.2, the total angular momentum can only change by $\Delta F = 0, \pm 1$, in a transition between hyperfine-structure levels. The transition $F = 0 \rightarrow F = 0$ is forbidden.

If for some reference isotope the magnetic dipole moment μ_ref (and nuclear spin I_ref) and the electric quadrupole moment Q_ref are known, these properties can be determined for other isotopes by measuring the hyperfine splitting of the same levels for both isotopes and using the relations

$$\begin{aligned} \mu_I &= \frac{A}{A_\mathrm{ref}} \frac{I}{I_\mathrm{ref}} \mu_\mathrm{ref} \\ Q &= \frac{B}{B_\mathrm{ref}} Q_\mathrm{ref}. \end{aligned} \tag{2.48}$$

Likewise the ratios $^{A_u}/_{A_l}$ and $^{B_u}/_{B_l}$ of two electronic levels (u upper and l lower) are, to first order, constant within an isotopic chain, as the nuclear contributions cancel out.

2.2.4 Investigated Transitions in Lead and Palladium

Lead (Z=82)

The lead ion (Pb) has no laser-accessible transitions out of the atomic ground state due to the large energy gap to the first excited state of opposite parity. But the neutral Pb atom offers a variety of laser-accessible transitions. Starting from the atomic ground state or metastable states as shown in Fig. 2.5. The latter one can be populated by electron transfer from other atoms in flight. Therefore, the Pb ions have to be neutralized. Within this work, this is performed by the use of a charge-exchange cell, filled with potassium vapor. $55\,\%$ of the neutralized Pb atoms will be in the metastable $6s^2 6p^2\ ^1\mathrm{D}_2$ state [89] which can be laser-excited to the $6s^2 6p 7s\ ^3\mathrm{P}_1$ state. Advantages of this transition are:

- Its wavelength of $723\,\mathrm{nm}$ is accessible with titanium-sapphire lasers.
- The lower state is efficiently populated in the charge-exchange cell.
- The branching ratio of the upper state (see Fig. 2.5) allows separation of the fluorescence light from the laser light using optical filters by detecting the $406\,\mathrm{nm}$ transition.

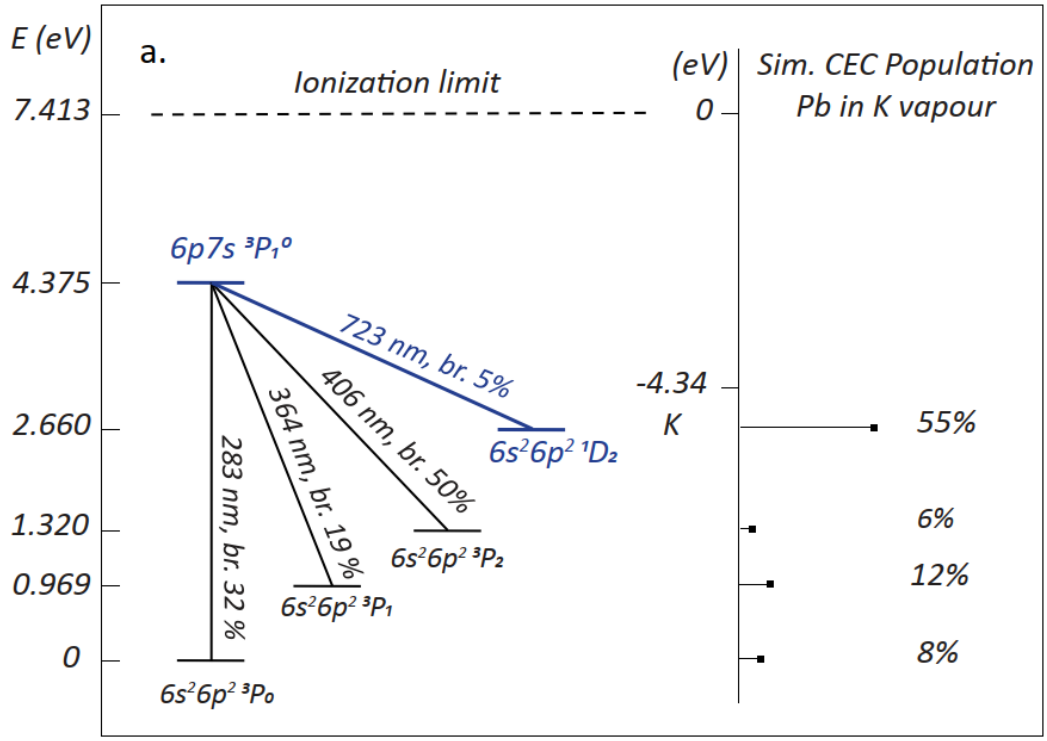

Figure 2.5: Left: Electronic energy levels in the lead atom. In this work, lead is excited from the metastable $6s^2 6p^2\ ^1\mathrm{D}_2$ state to the $6p7s\ ^3\mathrm{P}_1$ state. From there it can undergo different decays to 4 lower lying states. Right: Population probabilities after charge exchange with potassium vapor.

- Owing to the involvement of an s-electron in the transition, it is highly sensitive to the field shift and therefore to $\delta\langle r^2\rangle^{A,A'}$.
- The lower state is highly sensitive to the nuclear quadrupole moment while the upper level is sensitive to the nuclear magnetic moment.

The odd isotopes and the isomeric states show hyperfine splitting due to their non-zero nuclear spin. Depending on the nuclear spin, the lower and upper level can split up into different number of hyperfine levels. The hyperfine splitting for neutral Pb with nuclear spins $I = {}^1/_2, {}^3/_2$, and ${}^5/_2$ are shown in Fig. 2.6, 2.7 and 2.8 respectively. These schemes also show the allowed ($E1$) transitions.

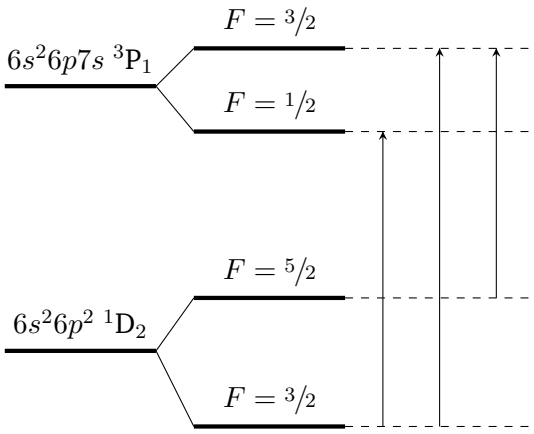

Figure 2.6: Level structure of atomic lead with nuclear spin $I = 1/2$. The left side shows the fine structure without hyperfine splitting. The right side shows the hyperfine splitting. The selection rules allow only three transitions.

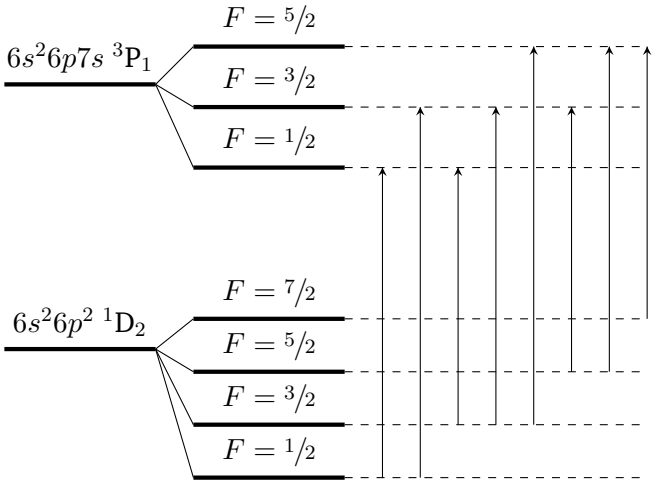

Figure 2.7: Level structure of atomic lead with nuclear spin $I = 3/2$. The left side shows the fine structure without hyperfine splitting. The right side shows the hyperfine splitting. The selection rules allow eight transitions.

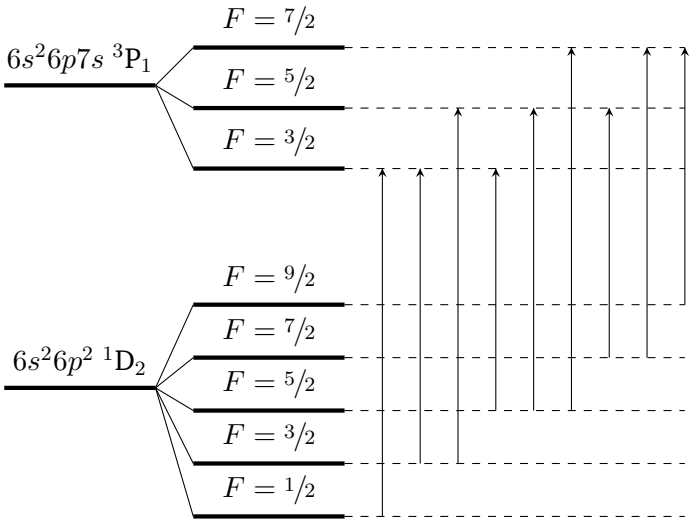

Figure 2.8: Level structure of atomic lead with nuclear spin $I = 5/2$. The left side shows the fine structure without hyperfine splitting. The right side shows the hyperfine splitting. The selection rules allow nine transitions.

Palladium (Z=46)

Like lead, palladium (Pd) offers laser-accessible transitions in the neutral atom. In this work Pd ions are therefore neutralized in a magnesium-filled charge-exchange cell. The ionization energy of magnesium (Mg) ($7.65\,\mathrm{eV}$) almost coincides with the binding energy of an electron in one of the $4d^9(^2\mathrm{D}_{5/2})5s$ levels of neutral Pd ($6.88 - 7.52\,\mathrm{eV}$) [90].

The population distribution of the different electronic states in Pd after charge exchange with Mg depends on the beam energy, the vapor pressure and the initial atomic states of the participating particles. Since right after the charge-exchange process many atoms will be in an excited state with finite lifetime, the population distribution changes over time after the charge exchange happened. The whole process can be simulated, like it was done and is described in detail within [46] and [89].

The simulated population distribution for a Pd ion beam of $29.85\,\mathrm{keV}$ with Mg vapor, after a time corresponding to $40\,\mathrm{cm}$ traveling distance, is shown in Fig. 2.9. It also shows the lowest atomic energy levels of Pd and transitions appropriate for laser spectroscopy. The $4d^9(^2\mathrm{D}_{5/2})5s$ levels are, according to the simulation, both populated by about $30\,\%$ while the $4d^9(^2\mathrm{D}_{3/2})5s\ ^2[3/2]_1$ level is populated by about $18\,\%$ and the population of the ground state is negligible.

All three transitions, the $363.6\,\mathrm{nm}$, $361.1\,\mathrm{nm}$ and $357.2\,\mathrm{nm}$ transitions, where tested with the experimental setup, in order to find the transition with the highest signal counts. All of these transitions include an s-electron and are therefore highly sensitive to $\delta\langle r^2\rangle^{A,A'}$. For the final spectroscopy measurements the $4d^9(^2\mathrm{D}_{5/2})5s\ ^2[5/2]_3 \rightarrow 4d^9(^2\mathrm{D}_{5/2})5p\ ^2[3/2]_2$ was chosen.

Depending on the nuclear spins, different hyperfine splittings can occur, which are shown in Fig. 2.10 and 2.11, leading to 3 transitions for isotopes with nuclear spin $I = 1/2$ and 14 transitions for isotopes with spin $I = 5/2$.

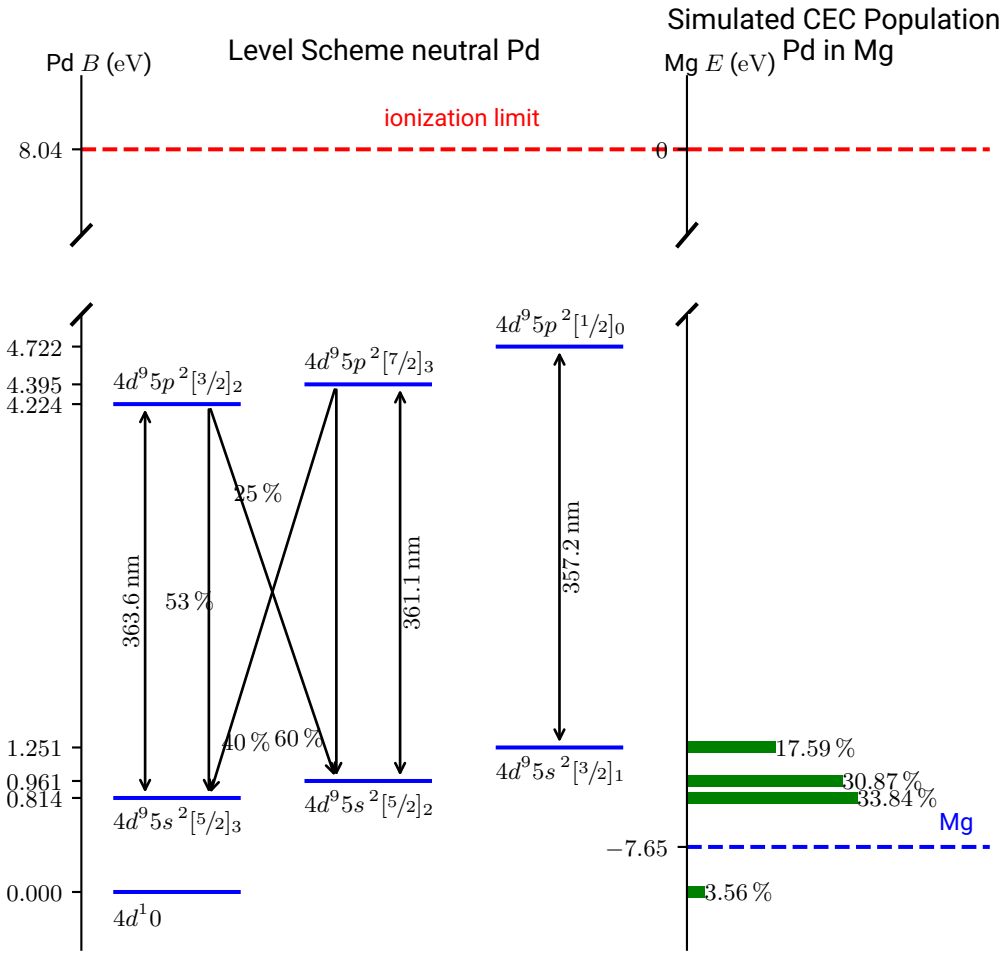

Figure 2.9: The left side shows the level scheme of atomic palladium with the electronic levels relevant for this work. The excitation energies (E) of the electronic levels are given on the left axis. The transition wavelengths are indicated as well as the branching ratios of the excited levels. The right side shows the simulated populations of the lowest electronic states after charge exchange with magnesium and after the ions have traveled $40\,\mathrm{cm}$, which corresponds to the center-center distance between the neutralization point in the CEC and the optical detection region. The simulation was performed for a $29.85\,\mathrm{keV}$ ion beam. The blue line indicates the ionization energy of magnesium, the red line indicates the ionization limit of palladium. The energies are taken from [90], the population distribution was calculated in [46].

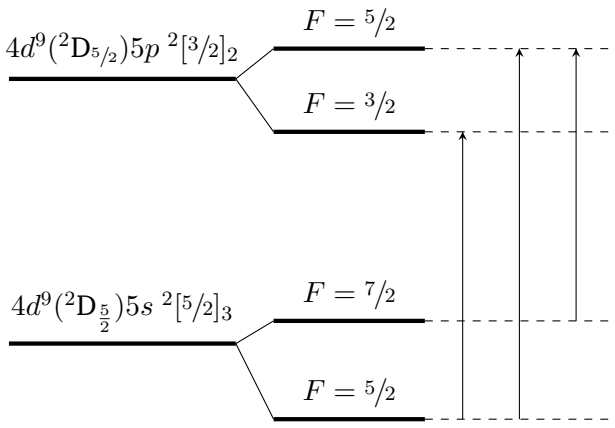

Figure 2.10: Level structure of atomic palladium with nuclear spin $I = 1/2$. The left side shows the fine structure without hyperfine splitting. The right side shows the hyperfine splitting. The selection rules allow only three transitions.

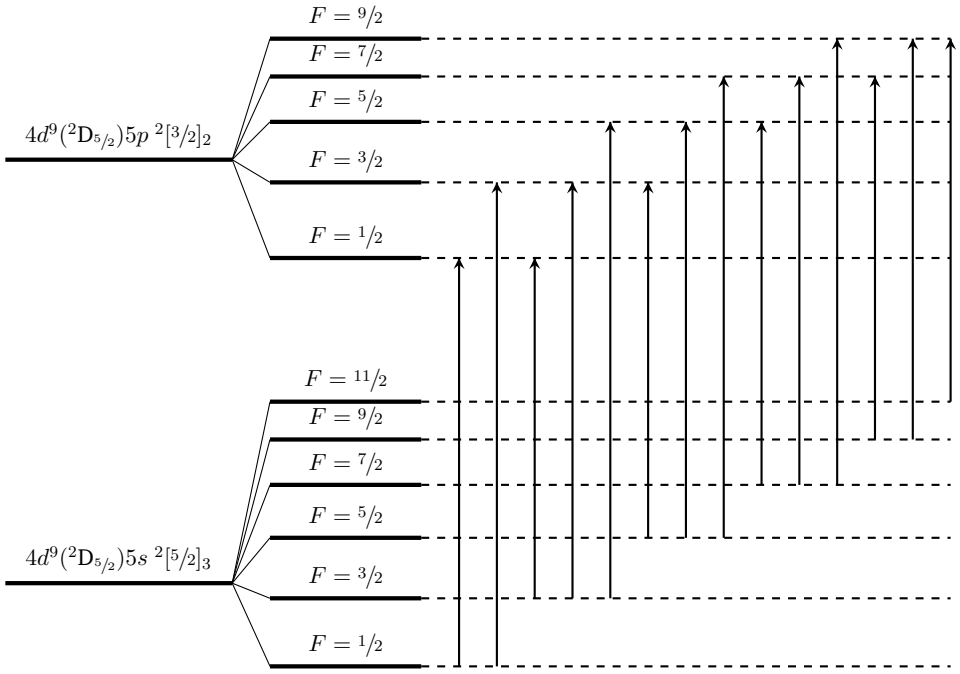

Figure 2.11: Level structure of atomic palladium with nuclear spin $I = 5/2$. The left side shows the fine structure without hyperfine splitting. The right side shows the hyperfine splitting. The selection rules allow fourteen transitions.

3 Regions of interest

The two investigated elements are known to show very different properties and characteristics. Lead's magicity manifests in simple nuclear structure and simple trends in the isotopic chain while the mid-shell palladium is expected to have a more complicated structure. The general properties of lead and palladium isotopes are described in the following sections.

3.1 Lead

With 82 protons, lead is a proton-magic nucleus and, as such, represents a textbook example and benchmarking case for the nuclear shell model. According to the model, all proton levels up to the $1h_{11/2}$ level are fully occupied, and the energy gap to the next proton level is comparably large (see Fig. 2.3). The three stable isotopes are ^{206,207,208}Pb, and the most naturally abundant isotope ^{208}Pb is a doubly magic nucleus with neutron number $N = 126$. The magic number $N = 126$ is visible as a kink in the trend of the differential radius $\delta\langle r^2\rangle^{A,A'}$ along the chain of isotopes (see Fig. 1.1). The magicity of $Z = 82$ can also be concluded from the trend of the differential radii $\delta\langle r^2\rangle^{A,A'}$. The experimental values agree very well to liquid drop model calculations assuming zero deformation (see Fig. 1.1).

The nuclear quadrupole moment Q_s, which quantifies the nuclear deformation, is expected to show only small values, as it would confirm the spherical shape of lead isotopes. Experimental values exist for $^{183-189,197-205}$Pb, but only with relative uncertainties in the order of 2 to 6 [59, 91, 92, 19, 93]. Nuclear quadrupole moments Q_s^m and differential radii $\delta\langle r^2\rangle^{A^m,A}$ for isomeric states are, as well, only known with large uncertainties.

The simple nuclear shell model predicts a linearly increasing Q_s^m for isotopes with an unpaired neutron in the $1i_{13/2}$ orbital, which is the only positive-parity level in this shell. Similarly, for the magic tin isotopes, the quadrupole moments of the isomeric $1h_{11/2}$ state should reveal a linear trend, which was not confirmed by experimental measurements [27], but instead, in the ground state moments of tin. If Q_s^m increases linearly along the lead isomers, while Q_s remains relatively constant, a simple model for the isomeric differential charge radii $\delta\langle r^2\rangle^{A^m,A}$, as proposed in [28], predicts a parabolic trend for $\delta\langle r^2\rangle^{A^m,A}$ with increasing mass. The model

connects the parabolic mass dependence of $\delta\langle r^2\rangle^{A^m,A}$ to the linear mass dependence of Q_s^m, combined with an almost constant and small deformation of the ground state nuclei.

In this work, the lead isotopes from $A = 187$ up to $A = 208$ were investigated. Their masses and known nuclear spins of the ground states and isomeric states are listed in Tab. 3.1.

Table 3.1: Atomic masses and nuclear spins of the ground states (I_{gs}) and isomeric state (I_{m}) of Pb isotopes as well as the parity π. Data is taken from [51].

A	m [u]	I^{π}_{gs}	I^{π}_{m}
187	186.983911(5)	$3/2^-$	$13/2^+$
188	187.980879(11)	0^+	
189	188.980844(15)	$3/2^-$	$13/2^+$
190	189.978082(13)	0^+	
191	190.978216(7)	$3/2^-$	$13/2^+$
192	191.975790(6)	0^+	
193	192.976136(11)	$3/2^-$	$13/2^+$
194	193.974012(19)	0^+	
195	194.974516(5)	$3/2^-$	$13/2^+$
196	195.972788(8)	0^+	
197	196.973435(5)	$3/2^-$	$13/2^+$
198	197.972015(9)	0^+	
199	198.972913(7)	$3/2^-$	$13/2^+$
200	199.971819(11)	0^+	
201	200.972870(15)	$5/2^-$	$13/2^+$
202	201.972152(4)	0^+	9^-
203	202.973391(7)	$5/2^-$	$13/2^+$
204	203.9730435(12)	0^+	
205	204.9744817(12)	$5/2^-$	$13/2^+$
206	205.9744652(12)	0^+	
207	206.9758968(12)	$1/2^-$	$13/2^+$
208	207.9766520(12)	0^+	

3.2 Palladium

Palladium has 46 protons, which is 4 protons below the proton shell closure at $Z = 50$ (tin). It has six stable isotopes ^{102,104,105,106,108,110}Pd. Tab. 3.2 lists the masses and spins of the investigated isotopes.

Isotopes with neutron numbers between $N = 56$ and $N = 72$ are investigated in this work, i.e. the neutron shells $1g_{7/2}$, $2d_{5/2}$, $2d_{3/2}$, $3s_{1/2}$ and $1h_{11/2}$ within the $N = 82$ shell can be populated. The simple nuclear shell model predicts the nuclear spin of the metastable

Table 3.2: Atomic masses an nuclear spins of the ground states (I_{gs}) and isomeric states (I_{m}) of Pd isotopes as well as the parity π. Data is taken from [51].

A	m [u]	I^{π}_{gs}	I^{π}_{m}
102	101.9056323(4)	0^+	
104	103.9040304(14)	0^+	
105	104.9050795(12)	$5/2^+$	$11/2^-$
106	105.9034803(12)	0^+	
108	107.9038918(12)	0^+	
110	109.9051729(7)	0^+	
112	111.907331(7)	0^+	
113	112.910262(7)	$5/2^+$	$9/2^-$
114	113.910369(7)	0^+	
115	114.913659(15)	$1/2^+$	$7/2^-$
116	115.914298(8)	0^+	
118	117.9190673(27)	0^+	

states to be $I = {}^{11}/_{2}$, but gamma decay experiments have already shown that the isomeric nuclear spins deviate from this simple prediction [94]. These deviations are caused by the complicated nuclear structure of mid-shell, or also called open-shell isotopes. For the same reason, the nuclear spins of the ground states cannot be expected to agree with single-particle predictions.

The complexity of the nuclear structure of palladium also manifests in the nuclear shape. Coulomb excitation measurements [40] indicate triaxial shapes for the stable palladium isotopes and elements with $Z < 46$ have revealed interesting shape evolutions (see. Fig. 1.3). The symmetry of a nuclear shape, i.e. (tri)axiality, cannot directly be concluded from laser spectroscopy measurements. But a comparison with theoretical calculations allowing either axial or triaxial states can give guidance in the understanding of nuclear shapes and nuclear structure.

4 Experimental Setups

This chapter explains the experimental technique of collinear laser spectroscopy and the extraction of nuclear parameters from optical spectra. After a general introduction to collinear laser spectroscopy based on the COLLAPS experiment, where lead was investigated, ATLANTIS is presented, at which the measurements on palladium were performed.

4.1 Fluorescence Laser Spectroscopy

An atomic transition can be driven by photons of frequency ν_{ph}, providing the energy $\Delta E_{\text{trans}} = h\nu_{\text{ph}}$ necessary for the excitation. The natural linewidth $\delta\nu_{\text{nat}}$ of a transition is

$$\delta\nu_{\text{nat}} = \frac{1}{2\pi\tau} \tag{4.1}$$

with the lifetime τ of the excited state, assuming that the lifetime of the lower level is infinite or at least much longer than that of the upper level. It limits the resolution in laser spectroscopy experiments even if all other sources of line broadening are eliminated.

For high-resolution fluorescence laser spectroscopy, a laser system provides nearly monochromatic (laser linewidth $\delta\nu_{\text{Laser}} \ll \delta\nu_{\text{nat}}$) photons with frequency ν_{ph} for the excitation of atoms or ions and the emitted photons from the subsequent radiative decays are detected and counted. This count rate decreases, if the laser frequency is not in resonance with the probed particles. By scanning the laser frequency across the resonance in the rest frame of the probed particles and measuring the count rate, a resonance signal is detected and the transition energy can be determined from the position.

In every laser spectroscopy experiment the measured spectroscopy lines are additionally broadened by the Doppler effect, as each particle in the probed particle ensemble sees a Doppler-shifted laser frequency depending on its individual velocity. To increase the resolution, and to make nuclear effects visible in atomic spectra, it is necessary to employ methods to reduce the Doppler broadening like it is done within this work by the use of collinear laser spectroscopy.

4.2 Collinear Laser Spectroscopy at ISOLDE

Collinear laser spectroscopy (CLS) has become a very useful tool and, thus, it has been established at several radioactive beam facilities in the world and even more devices are under construction [95]. After a first demonstration at the TRIGA research reactor in Mainz [96], the pioneering CLS experiment COLLAPS was installed at ISOLDE, CERN in 1979 [97]. A detailed description of the ISOLDE facility can be found, e.g., in [98]. The focus of the following brief description is on the production and preparation of the ion beam for the measurements on the lead isotopes, performed within this work at COLLAPS.

4.2.1 Ion Beam Production and Preparation

The radioactive ion beam facility ISOLDE produces numerous isotopes from helium up to radium ($Z = 88$) via the isotope separation online (ISOL) technique. For this work, radioactive lead ions were used. A thick uranium carbide target was bombarded with $1.4\,\mathrm{GeV}$ protons from the Proton Synchrotron Booster. Lead isotopes are dominantly formed by spallation reactions of uranium, evaporate from the hot target and diffuse into the ion source. These lead atoms are selectively ionized by RILIS [99], a resonance ionization laser ion source, and accelerated from a high-voltage potential. RILIS provides rather pure ion beams with only very low admixtures of isobars coming from surface ionization. After mass separation in the high-resolution mass separator (HRS), the ions are guided to ISCOOL, a radio-frequency quadrupole cooler-and-buncher (RFQCB) [100, 101].

The task of ISCOOL is to stop and cool the ions during accumulation, and to eject the cooled ion bunches. A combination of electrostatic and radio-frequency electric fields confine the ions in the buffer-gas region before they are ejected as a short bunch of typically a few µs length to the experiment. To stop the ions, ISCOOL is located on a high-voltage platform at approximately the ion-beam energy. The ions enter the gas-filled region and dissipate energy in collisions. Afterwards they are not able to overcome the potential walls at the entrance and exit of the RFQCB anymore and are trapped. Further collisions of the trapped ions with a buffer gas reduce the transverse and longitudinal velocity spread. More details are given in the description of the ATLANTIS-RFQCB in Sec. 4.3.5.

For the lead measurements, ISCOOL was operated at bunching frequencies between 25 and $200\,\mathrm{Hz}$, depending on the production rate, total beam currents and half-life of the respective isotopes, and bunch lengths of about $10\,\mu\mathrm{s}$ were achieved. The main advantage for CLS, besides the improvement of beam properties, is the bunch structure that improves the signal-to-background ratio considerably. The latter stems dominantly from scattered laser light that impinges on the photo multiplier tubes (PMTs). Assuming a repetition rate of $50\,\mathrm{Hz}$, all ions of

a continuous beam coming in within 20 ms are compressed into a 10 µs bunch. Time-resolved detection of the fluorescence photons allows to accept only photons arriving during the passage of the ion bunch through the optical detection region, while excluding the background signal acquired during the remaining 19.99 ms. This enhances the signal-to-background ratio of the CLS measurement by a factor of 2000. With longer accumulation times and a shorter bunch length, like it has been realized in this work at the ATLANTIS setup, the sensitivity boost can be increased even further.

4.2.2 COLLAPS

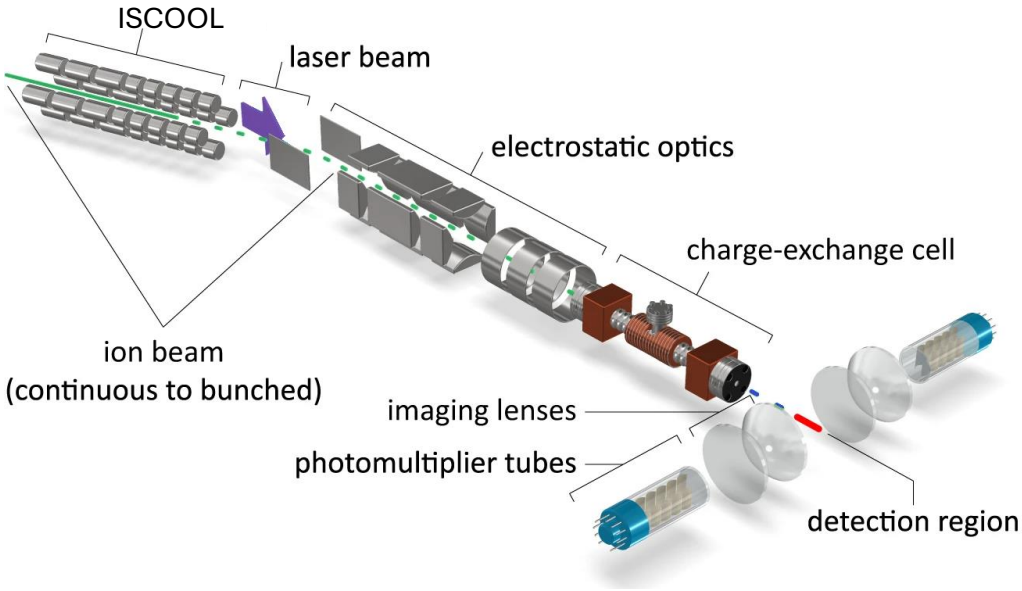

Figure 4.1: Setup of COLLAPS. The bunched ion beam from ISCOOL enters the COLLAPS beamline at an angle of 10° and is overlapped collinearly with the laser beam. It is tuned with electrostatic ion optics and guided into the charge-exchange cell. The CEC is on a scannable electric potential defining the velocity of the resulting atoms. In the subsequent detection region the laser-atom interaction takes place. Fluorescence light is collected by lens systems onto photomultiplier tubes. Figure taken from [27]. Used under CC by 4.0, cropped from original.

Figure 4.1 shows a schematic drawing of the COLLAPS setup. The ion bunches from ISCOOL are reaccelerated from the high-voltage potential with the acceleration voltage $U_{\text{acc}} \approx 50\,\text{keV}$, monitored with a high-precision high-voltage divider [102], and are guided into the CLS beamline. The ions enter the beamline through a 10° bender to be superimposed collinearly with the spectroscopy laser. The initial velocity distribution δv_0 of the ions in the buncher is

further reduced by the acceleration (*Doppler compression*) to [103]

$$\delta v \approx \frac{\delta v_0}{2}\sqrt{\frac{\Delta E}{qU_{\text{acc}}}}, \tag{4.2}$$

where ΔE is the initial energy distribution of the ions before acceleration and q the electric charge of the ions. For a typical energy spread from ISCOOL of $1\,\text{eV}$ [101] the acceleration to $50\,\text{keV}$ reduces the observed Doppler broadening by a factor of 2×10^{-3}.

A very important advantage of CLS is that the Doppler compression takes place in-flight, such that the time between ion production and probing is very short, once the ion has left the ion source. It takes only a few $10\,\mu\text{s}$ to transport the ions to the CLS setup, which is much shorter than β-decay half-lifes. This makes high-resolution laser spectroscopy also possible for short-lived isotopes and isomers. Thus, it is often the extraction time from the target-ion source combination that limits the applicability even if a sufficient amount of an isotope is produced in the target.

In the COLLAPS beamline the ion beam is further shaped by ion-optical elements like electric quadrupoles and lenses before it enters the charge exchange cell (CEC). The CEC is used for the production of a fast atomic beam suitable for CLS, neutralizing the ions with almost no velocity broadening [104]. Inside the CEC an alkaline metal (here potassium) is heated to a temperature that ensures sufficient neutralization efficiency. During the collision process of ions and alkaline atoms, an electron can be transferred from the neutral alkaline atom to the ion, e.g.,

$$\text{Pb}^+ + \text{K} \rightarrow \text{Pb} + \text{K}^+ + \Delta E. \tag{4.3}$$

The efficiency of this charge-exchange process also depends on the ionization energy of the alkaline atom, the atomic energy levels within the ion, and its kinetic energy. The charge-exchange agent is therefore chosen according to the investigated element and the atomic state that is to be populated.

The CEC is floated on an additional electric potential which can be scanned between -10 and $+10\,\text{kV}$ for Doppler tuning, i.e., by scanning the additional voltage, the ion velocities are scanned, before they are neutralized. The velocity v of the ions Doppler shifts the observed transition frequency in the laboratory frame according to

$$\nu_0 = \nu_{\text{a/c}}\gamma\left(1 \pm \beta\right) \quad \Leftrightarrow \quad \nu_{\text{a/c}} = \nu_0\gamma\left(1 \mp \beta\right) \tag{4.4}$$

with the transition frequency ν_0 in the ions' rest frame, the laboratory laser frequency $\nu_{\text{a/c}}$ in anti-/collinear geometry, the ions' velocity $\beta = {}^{v}/_{c}$ in terms of the speed of light c, and the Lorentz factor $\gamma = \left(1 - \beta^2\right)^{-1/2}$. By scanning the additional acceleration voltage applied to the

CEC, i.e., the velocity of the ion bunch, a fluorescence spectrum can be measured with a fixed laser frequency. This is called Doppler tuning and allows to keep the laser frequency stabilized during a measurement. When leaving the CEC and the scanning potential, the atom velocities are not changed, as they do not see the electric potential. With this technique, high-resolution laser spectroscopy can also be performed on atoms [104].

After neutralization, the atom bunch passes through the interaction and detection region. In this part of the beamline, the atoms are resonantly excited by the laser and the subsequent fluorescence light is guided by lenses into photo multiplier tubes (PMTs) [105]. The collinear alignment allows for a long interaction region between ions and laser, increasing the number of induced transitions.

4.2.3 Absolute Transition Frequency

According to Eq. (4.4) the absolute frequency of a transition can only be measured if the laser frequency and the exact ion velocity are known. While the laser frequency can be measured accurately, the ion velocity is usually not known well enough. By performing collinear and anticollinear laser spectroscopy simultaneously or in direct succession and combining both measurements according to

$$\nu_a \nu_c = \nu_0 \gamma(1+\beta)\, \nu_0 \gamma(1-\beta) = \nu_0^2, \tag{4.5}$$

the velocity dependence can be removed and the absolute transition frequency ν_0 extracted [106, 107].

4.2.4 Laser System

The $723\,\mathrm{nm}$ laser wavelength, required for CLS on lead atoms, was generated by a tunable titanium-sapphire Matisse 2DS laser pumped by $25\,\mathrm{W}$ of a Millenia laser. The laser frequency is long-term stabilized using a cavity (High Finesse WS8-2) which is again regularly calibrated to a helium-neon laser. The laser beam is transported through air about $25\,\mathrm{m}$ to the COLLAPS beam-line. There, a spatial filter is used to obtain a spatial Transverse Electromagnetic Mode TEM00 profile, i.e. a cross sectional Gaussian intensity distribution, and the beam is collimated and directed through the COLLAPS setup.

4.3 Collinear Laser Spectroscopy at CARIBU

Not all elements can be produced and extracted from the target by the ISOL technique, as the evaporation temperature is limited to $\sim 2000\,°\mathrm{C}$, which is too low for refractive elements. Therefore, for the measurements of palladium, a new beamline has been set up at the Argonne National Laboratory in Chicago [46, 108].

4.3.1 Online Ion Source CARIBU

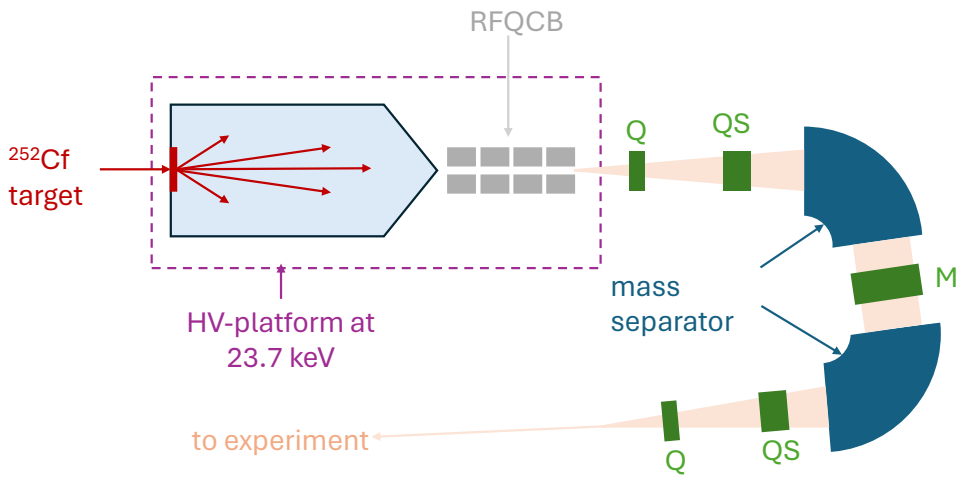

Figure 4.2: Schematic drawing of the CARIBU facility. The small high-voltage platform hosts the gas catcher with the ^{252}Cf fission target. The fission fragments transverse the RFQCB before they are accelerated to the larger high-voltage platform. A combination of quadrupoles (Q) and sextupoles (S) guide the ions through two high-homogeneity $60°$ magnetic dipoles (with an electrostatic multipole (M) in between) for isobaric mass separation before the ions are guided to the CLS setup.

The Californium Rare Isotope Breeder Upgrade (CARIBU) [45] produces short-lived isotopes through spontaneous fission of ^{252}Cf. A general overview of the setup is depicted in Fig. 4.2. Due to the high energy released in the fission process, the products recoil from the thin layer of Cf and are stopped in a gas catcher filled with helium gas. The generated singly or doubly charged ions are extracted from the gas catcher by an electrical drag-field and finally, close to the exit hole, by the gas flow. A subsequent RFQCB cools and bunches the extracted ions before they are accelerated to $\sim 23.7\,\mathrm{keV}$, mass separated by a combination of

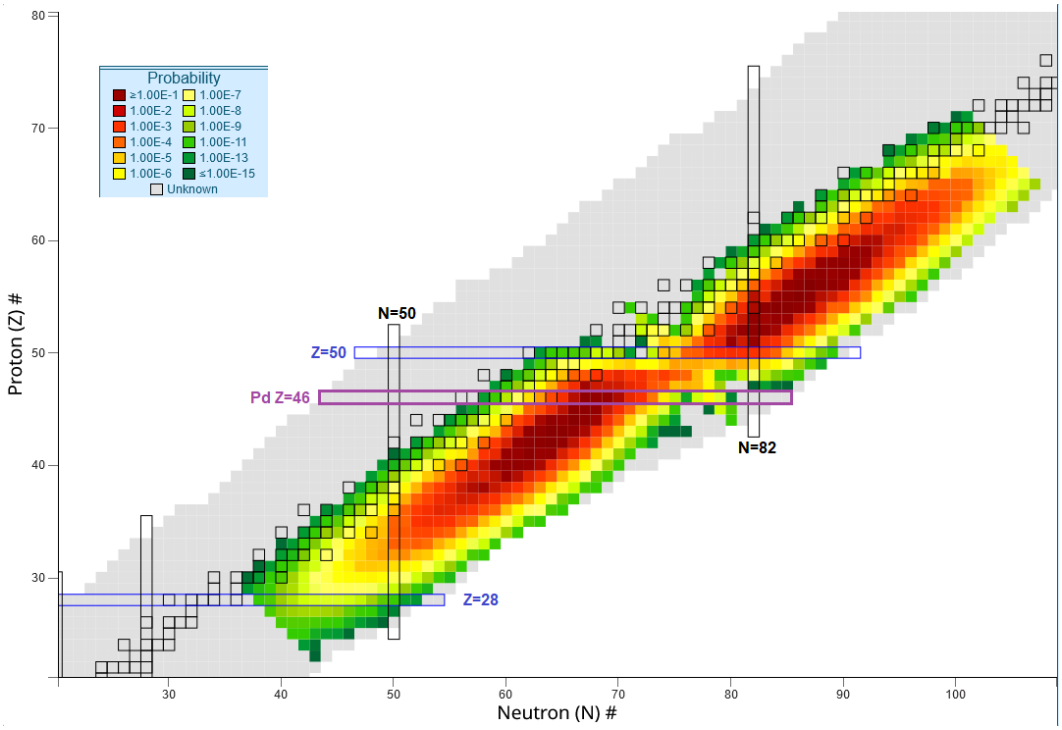

Figure 4.3: Fission yields of ^{252}Cf. The yields are color-coded and normalized so that their sum equals 2. Additionally to the nuclear shell closures, the palladium isotopic chain is highlighted. Figure taken from [51].

two $60°$ magnetic dipoles in combination with an electrostatic multipole, and guided to the experiment.

The fission fragment mass distribution of ^{252}Cf is shown in Fig. 4.3. It exhibits a high production yield in the neutron-rich region just below the magic tin isotopic chain, giving access to the neutron-rich palladium isotopes. Their nominal production rates by CARIBU are listed in Tab. 4.1, assuming a 1 Ci ^{252}Cf source. Unfortunately only an activity of 500 mCi [109] was reached. Additionally, the thicker-than-intended target reduced the number of released recoils from the source installed in 2019 down to 130 mCi and the half-life of ^{252}Cf (2.645 a) lead to a continuously decreasing yield. At the time when the CLS experiments were performed, the available yields were therefore a factor of $10 - 50$ smaller than listed in the table.

4.3.2 Offline Ion Source

A laser ablation ion source is installed to produce stable palladium ions for offline tests and reference measurements with stable isotopes during online campaigns. A laser pulse with a pulse power of up to 20 mJ impinges on a palladium target ablating material from the target

Table 4.1: half-lifes and yields of palladium isotopes produced at CARIBU. Numbers are taken from [110]. The real yields during the experiments in 2022 and 2023 were reduced by a factor of about $10 - 50$ due to issues with the ion-source thickness and the half-life of ^{252}Cf.

Isotope	$t_{1/2}$	rates [ions/s]
^{110}Pd	stable	$8.0 \cdot 10^2$
^{111m}Pd	5.5 h	$2.3 \cdot 10^3$
^{111}Pd	23.4 m	$1.6 \cdot 10^3$
^{112}Pd	20.04 h	$9.8 \cdot 10^3$
^{113}Pd	1.64 m	$3.1 \cdot 10^4$
^{114}Pd	2.48 m	$2.4 \cdot 10^4$
^{115}Pd	47 s	$2.2 \cdot 10^4$
^{116}Pd	12.7 s	$1.1 \cdot 10^4$
^{117}Pd	5 s	$3.8 \cdot 10^3$
^{118}Pd	2.4 s	$1.7 \cdot 10^3$

surface and creating a plasma. The positive ions are then extracted from the source by an electric field. The amount of produced ions can be adjusted by the power of the ablation laser. The whole ion source is mounted on a high-voltage platform which is on a similar potential as the CARIBU platform. The relevant part of the beamline is shown in Fig. 4.4.

4.3.3 The ATLANTIS Radio-Frequency Quadrupole Cooler-and-Buncher

Online and offline ions are guided to the RFQCB just before the CLS beamline, which ensures well-defined beam properties that are independent from the source. The setup of the injection beamline and the RFQCB is shown in Fig. 4.4. Either the online or the offline beam can be chosen by the use of an electrostatic diverter. The beam can then be monitored on two micro-channel plates (MCPs) before it is injected into the RFQCB. The ejected ion bunch can be monitored on another MCP located after the RFQCB.

The ATLANTIS-RFQCB is a copy of a design for the CLS experiment BECOLA at FRIB [111] and is described in detail in [112]. It was specifically designed to enhance the sensitivity of CLS measurements. The efficiency of the RFQCB in bunched mode is reported to be up to $\sim 80\,\%$ [112], depending on the buffer-gas pressure and the cooling time.

The electrode setup for the static field of the RFQCB is shown in Fig. 4.5. The extraction field is defined by the voltage applied to the last three electrodes A, B and C. B is called the trapping electrode, which defines the depth of the trapping potential. C is called the pulling (extraction-)electrode and A is called the kicking (extraction-) electrode. During accumulation, the pulling electrode is on a potential $25\,\mathrm{V}$ above the trapping electrode while the kicking electrode is $4.7\,\mathrm{V}$ above the trapping electrode. The trapping electrode is on $-59.2\,\mathrm{V}$ relative to the total buncher

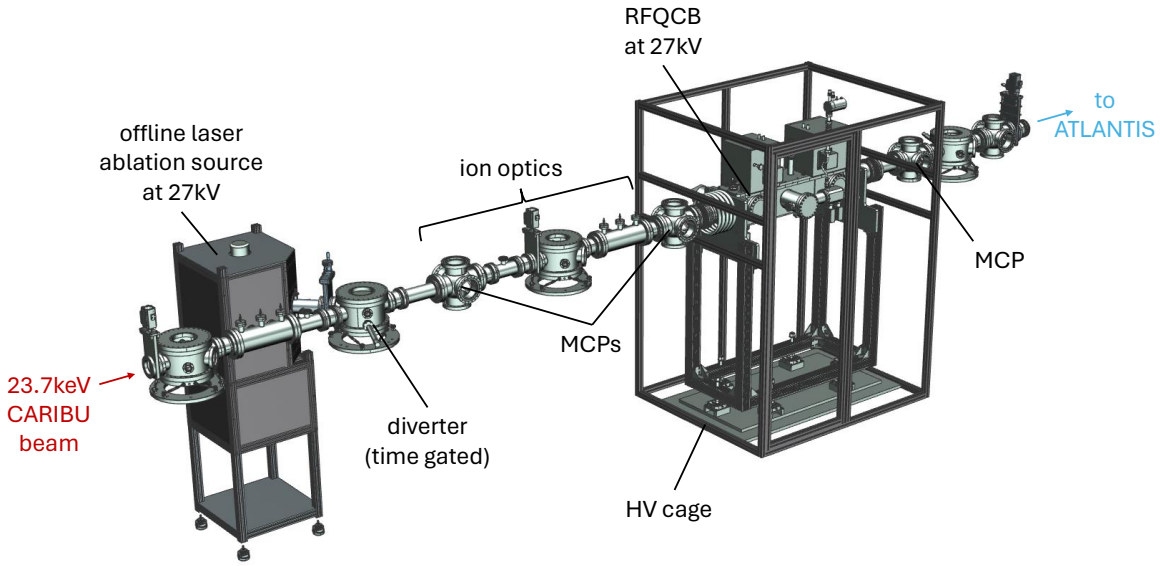

Figure 4.4: The injection beamline and RFQCB section. Radioactive (CARIBU) or stable (offline) beam can be chosen with a voltage applied to a diverter. In offline mode, the diverter is time gated on the ablation laser trigger. Electrostatic ion optics guide the ion beam into the RFQCB, which is lifted to the same potential as the ion beam. The beam can be monitored on micro-channel plates (MCP) before and after the RFQCB.

potential (23.7 kV). In this mode, the trapping and extraction electrodes form a potential well deep enough to trap and accumulate the stopped and cooled ions. For extraction, the pulling electrode has to be switched to a lower potential to release the ions. The kicking electrode is additionally switched to a higher potential, ”kicking” the ions out of the trap. A set of hyperbolic electrodes at the exit of the RFQCB collimates the ion beam before the ions are accelerated out of the trap into the transport beamline towards the CLS setup.

The combination of DC voltages applied to the trap and the extraction electrodes defines the properties of the ejected ion bunches and has been optimized during commissioning experiments that are described in Sec. 4.3.5.

4.3.4 ATLANTIS

From the RFQCB, the ion bunches are reaccelerated to 23.7 keV into the **A**rgonne **T**andem hall **LA**ser beamli**N**e for a**T**om and **I**on **S**pectroscopy (ATLANTIS). A schematic drawing of ATLANTIS is shown in Fig. 4.6. The setup follows the same principle as the COLLAPS beamline. It includes a new charge-exchange cell which was particularly designed for the use with

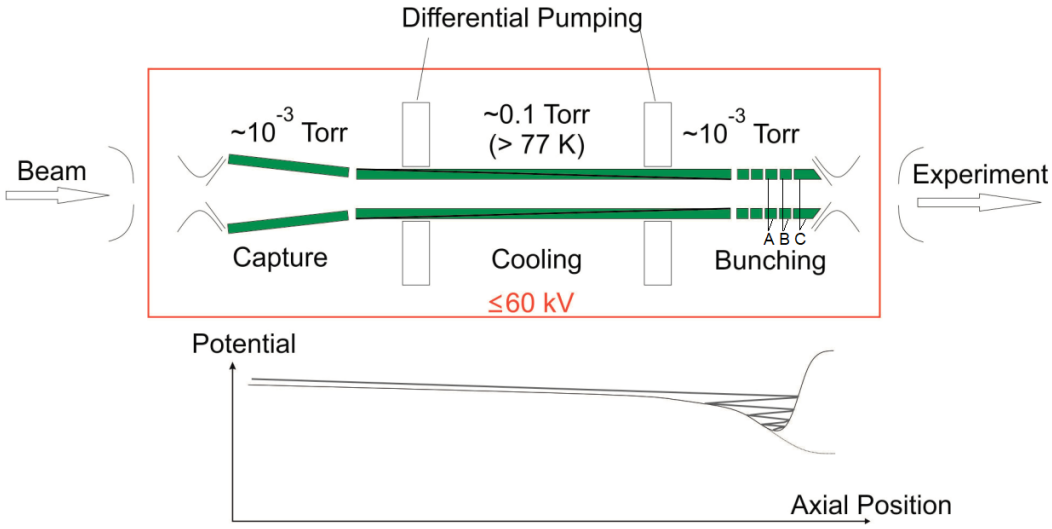

Figure 4.5: Top: Schematic of the electrostatic structure of the RFQCB. The ion beam is focused by hyperbolic electrodes into the conical capture segment of the RFQCB. The dragging field in the cooling segment is created by diagonally wedged segments. The cooled ions then enter the bunching segment. It consists of segmented electrodes creating the trap potential. The extraction field is mainly defined by electrodes A, B, and C. The hyperbolic electrodes at the exit collimate the ion beam during re-acceleration. Bottom: Static potential along the RFQCB axis in accumulation mode (potential on the right is high) with an exemplary ion trajectory and in ejection mode (potential on the right is low). Figure taken and adapted from [112].

magnesium [46]. This new CEC can be set on a scannable potential between -500 and $500\,\mathrm{V}$ for Doppler tuning.

The fluorescence light was detected in two identical detection regions, each consisting of a parabolic mirror system that focuses the fluorescence light into two PMTs, which are positioned perpendicular to the beam axis. A detailed describtion of the detection region design is provided in [108].

The setup can be used for both collinear and anti-collinear laser spectroscopy. Two movable beam monitoring systems are installed before the CEC and at the end of the beamline. For stable beams, the ions are monitored on MCPs during beam tuning. For radioactive beams, a silicon detector is moved into the beam instead. To check the neutralization efficiency during laser spectroscopy measurements, the ions remaining after the CEC can be deflected onto the silicon detector at the end of the beamline.

After the installation of the beamline, commissioning measurements and optimizations of the ATLANTIS-RFQCB and the CEC were carried out within this work and are described in the following sections.

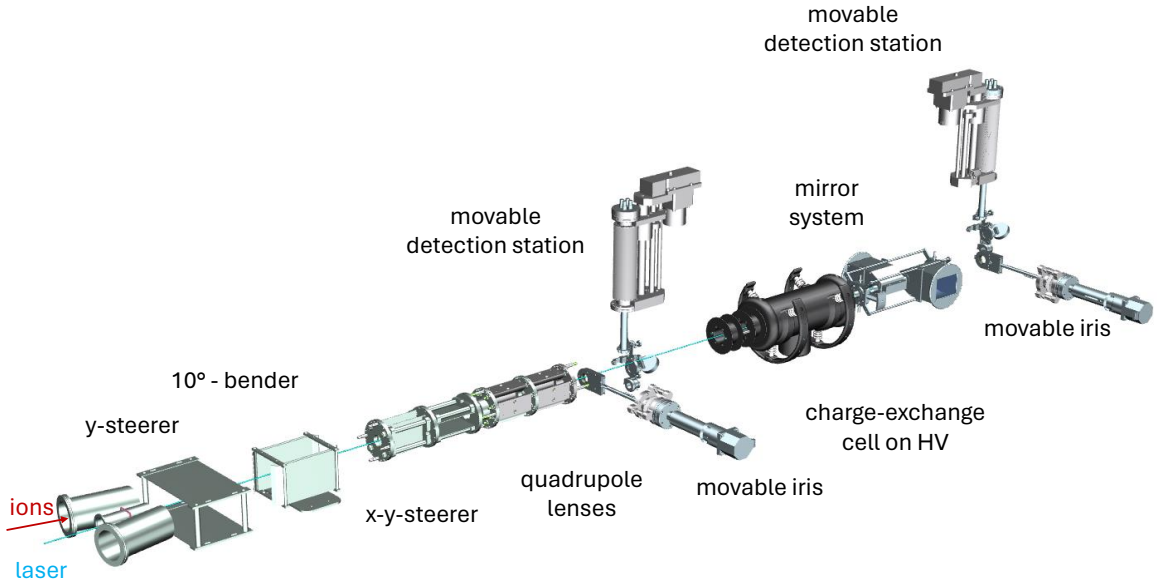

Figure 4.6: Schematic drawing of the interior part of ATLANTIS. The ion beam enters the beamline from the left through a y-steerer and the $10°$-bender and are overlapped with a collinear or anti-collinear laser beam. It is tuned and focused by the following electrostatic ion optics. The ion beam can be monitored on an MCP or a silicon detector, which are included in the movable detection station.To optimize the beam overlap and laser background, two irises can be opened and closed within the beam path. The ions are neutralized in the Mg-filled charge-exchange cell, which is on the scanning potential. At the end of the beamline, a second detection station allows to monitor the beam. It also includes a deflection electrode, such that any residual ions after charge exchange can be deflected off-axis to be monitored continuously during the spectroscopy measurement. The fluorescence detection region consists of two elliptical mirror systems, focusing the emitted photons onto PMTs outside of the beamline.

4.3.5 Comissioning of the Radio-Frequency Quadrupole Cooler-and-Buncher

The ion bunch extracted from the RFQCB can be characterized by its energy and time-of-flight (ToF) distribution. Both depend strongly on the amount of ions in the RFQCB and on the trapping and extraction fields. For the RFQCB commissioning, singly ionized zirconium ions from the offline ion source were used. For the investigation of bunch length and energy distribution, CLS was performed on the $4d^2 5s\,{}^4\mathrm{F}_{3/2} \rightarrow 4d^2 5p\,{}^4\mathrm{G}_{5/2}$ transition at $357.3\,\mathrm{nm}$. Zirconium was chosen since ${}^{90}\mathrm{Zr}$ is a stable even-even isotope that does not exhibit hyperfine structure and has the largest natural abundance of about $50\,\%$. Moreover it can be studied on the ionic transition and does not require the operation of the CEC additionally.

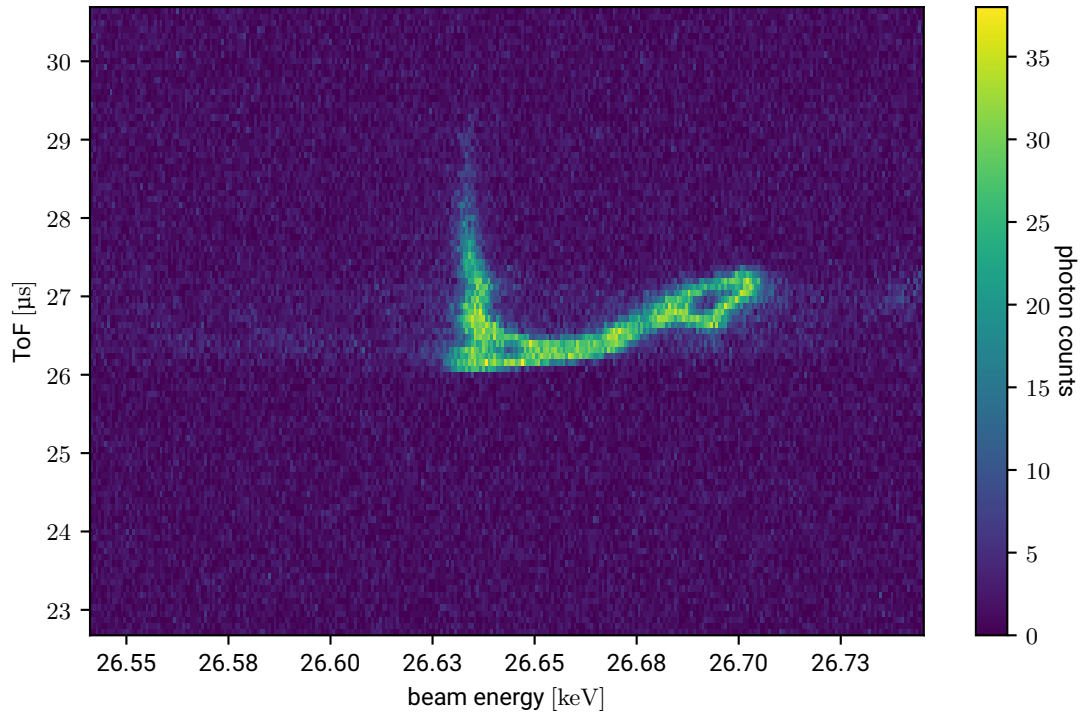

Figure 4.7: Resonance spectrum of ^{90}Zr before the RFQCB was tuned. The horizontal axis represents the ion beam energy in keV and the vertical axis the time-of-flight in µs between the RFQCB and the detection region. The detected photon counts are color-coded. Ions of different initial velocities require different Doppler-tuning voltages to show resonant fluorescence. Therefore, resonances appear at different acceleration voltages, depending on the ions' initial velocities, and the bunch shows a strong distortion in time and energy.

The first spectrum taken is presented in Fig. 4.7. The plot shows the total acceleration voltage (RFQCB-potential + Doppler-tuning potential) on the horizontal axis and the ToF on the vertical axis. The number of detected photons is color-coded in this time-energy plane. If all ions in the bunch have the same energy, the resonance appears for all ions at the same acceleration voltage. A different ion velocity requires a different Doppler-tuning potential to be in resonance. Thus, the horizontal axis represents the ion velocity distribution while the vertical axis encodes the arrival time of the ions at the detection region. Optimally, the different velocity classes should be homogeneously distributed in the ejected ion bunch, yielding a symmetric resonance shape in the time-energy plane. Space-charge effects and detuned trapping and extraction voltages can cause a separation of the different velocity classes within the ion bunch and to leaking off the trap. Both effects lead to a distorted shape of the resonance as observed in Fig. 4.7.

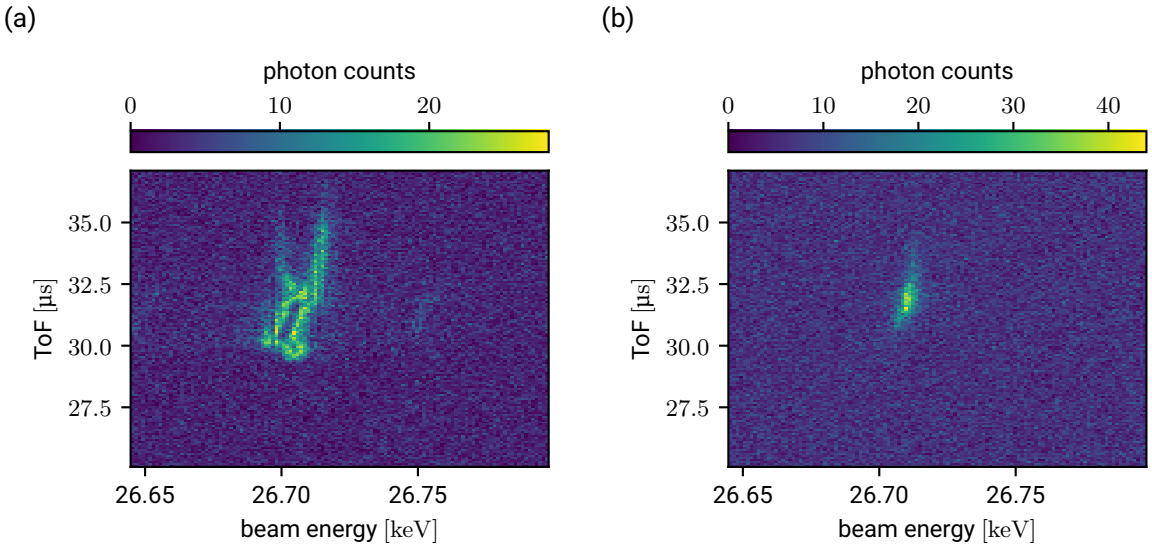

Figure 4.8: Time-resolved ^{90}Zr spectra of bunched ions with different RFQCB fillings. (a) The incoming ion bunches from the laser-ablation source were not time gated, leading to an overfilled RFQCB. In the time-energy plane, the resonance is distorted to an asymmetric and very broad distribution. (b) The overfilling of the RFQCB was efficiently reduced by time gating the incoming ion bunch and selecting the Zr^+ ions. The distortion is significantly reduced.

Overfilling of the RFQCB is the main reason for the strong distortion. Thus, reducing the ion current from the offline source reduces the distortion, but it is difficult to eliminate the overfilling completely while maintaining a spectroscopy signal of the isotope of interest simply by reducing the ablation-pulse power. This is because laser ablation produces a mixture of different elements, isotopes, molecules and charge states, which are all guided into the buncher. All of them contribute to the charge load of the trap. Contrary, no effects from overfilling have been observed with the online beam, since CARIBU provides a mass-to-charge-separated beam and the beam rates are too low to overfill the RFQCB.

Instead of reducing the ablation power of the offline source, a scheme was implemented to gate out the unwanted ions from the primary beam. By monitoring the ion bunch time-resolved on the MCPs before and after the RFQCB, the Zr peak (and later the Pd peak) could be identified in the ToF spectrum. To gate out higher masses, a fast switch was used on the diverter voltage, triggered relative to the ablation laser pulse. In Fig. 4.8, Zr spectra with and without gating on the diverter are compared to show the large effect of the contaminating particles on the RFQCB performance. Even with an adequate charge load, the shape of the bunch strongly depends on the trapping and extraction field at the end of the RFQBC. Fig. 4.9 shows the difference of the time-energy distribution of an ion bunch with the different pulling

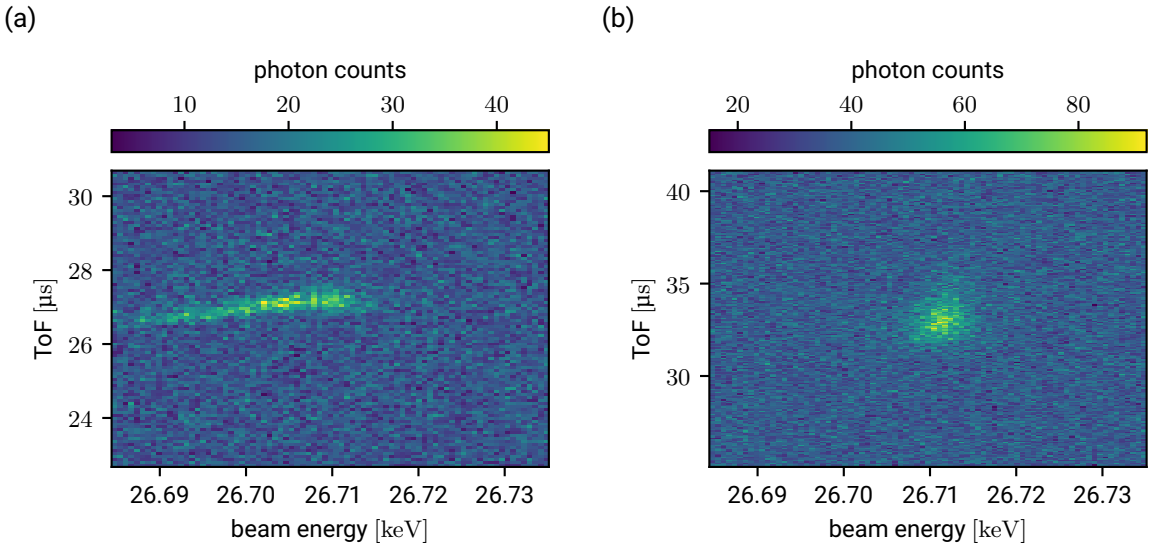

Figure 4.9: Time-resolved Zr spectra of ToF preselected and bunched ions with different voltage settings of the pulling and kicking electrodes according to Tab. 4.2. (a) The time-energy spectrum with maladjusted RFQCB potentials shows a broad and distorted shape. (b) Optimized pulling and kicking voltages lead to a symmetric resonance with a strongly reduced energy width.

and kicking voltages in extraction mode listed in Tab. 4.2.

Table 4.2: Voltages applied to the the kicker, trap and puller electrodes of the RFQCB for Zr^+ during accumulation (accum.) and during ion bunch extraction (extr.) according to Fig.4.9. The optimized accumulation and extraction voltages for Pd^+ ions are listed in the last two rows.

mode	A: kicker [V]	B: trap [V]	C: puller [V]
accum. Zr	-55.3	-59.2	-35
extr. Zr Fig. 4.9(a)	44.7	-59.2	-135
extr. Zr Fig. 4.9(b)	-45.3	-59.2	-75
accum. Pd	-55.3	-60	-35
extr. Pd	-40.3	-60	-110

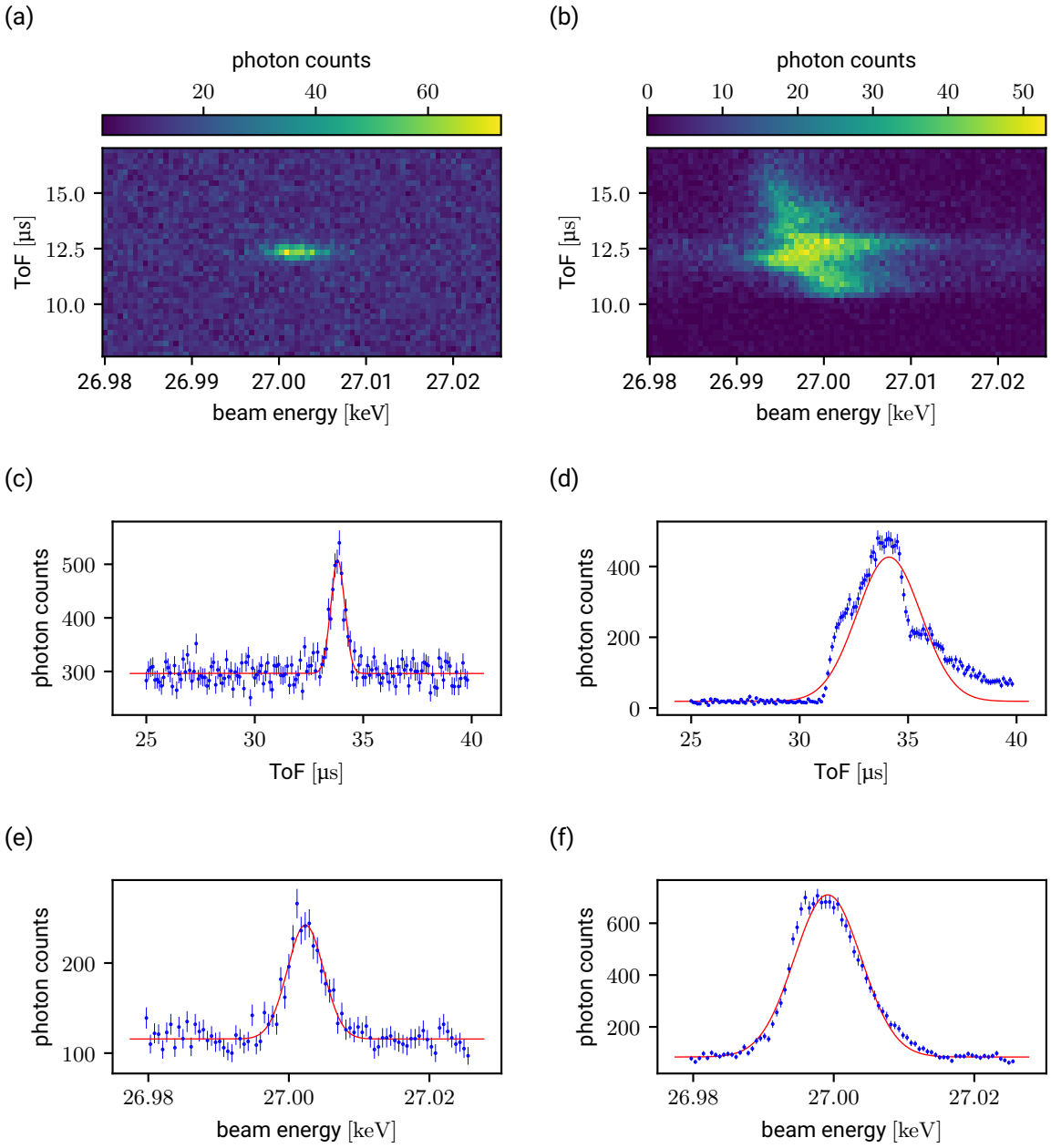

Figure 4.10: Resonance spectra of bunched ^{108}Pd ions with different RFQCB fillings. (a) In the time-energy plane, the resonance with a low filling is narrow and symmetric, compared to (b) an overfilled RFQCB that leads to a distorted resonance. The time projections (ToF spectra) of these resonances are plotted in (c,d), where the red curves represent a Gaussian profile fitted to the data. For (c) low filling, the data is well described by a symmetric Gaussian with FWHM of $0.8\,\mu s$, whereas (d) the overfilled RFQCB exhibits a strongly distorted non-Gaussian ToF spectrum with a much broader FWHM of $3.5\,\mu s$. The energy projections of the resonances (e,f) are also fitted with Gaussian profiles (red lines). For (e) low filling, a symmetric lineshape with FWHM of $6\,eV$ is observed, whereas (f) an overfilled RFQCB distorts the energy spectrum and broadens the FWHM to $11\,eV$.

Time-Energy distribution

As described in the previous section, the amount of injected ions into the RFQCB strongly influence the time-energy distribution of the ejected ion bunches. It is therefore crucial that CLS measurements are not taken on ion bunches coming from an overfilled RFQCB.

Figure 4.10 (a) and (b) show exemplary time-resolved spectra of the $4d^9(^2\mathrm{D}_{5/2})5s\ ^2[5/2]_3 \rightarrow 4d^9(^2\mathrm{D}_{5/2})5p\ ^2[3/2]_2$ transition in ^{108}Pd atoms produced in the offline ion source, injected into the RFQCB with optimized extraction-electrode settings, and neutralized in the CEC. The two spectra were taken with low and with maximum laser-ablation power and the ions are ToF pre-selected, like in Fig. 4.8 (b). The amount of ions injected into the RFQCB strongly influences the resulting resonance shape. For a low filling of the RFQCB the time-energy distribution is symmetric and has a small width while it is broad and asymmetric for an overfilled RFQCB.

Figure 4.10 (c) and (d) show the time projections (ToF spectra) of the same measurements. It is clearly visible that an overfilled RFQCB leads to a very broad distribution in time and that the ToF spectrum cannot be assumed to be Gaussian-like for an overfilled RFQCB. The shoulders in the ToF spectrum are formed from ions with very different kinetic energies. If the CLS spectrum of one isotope and its reference isotope show different ToF profiles, i.e., contain different kinetic energy classes, they cannot be used to derive a precise isotope shift.

The projection of the resonance spectra onto the energy axis are presented in Fig. 4.10 (e) and (f). While (e) shows a symmetric and narrow resonance profile, the overfilled RFQCB in (f) causes an asymmetric profile with a flat top and a longer tail at higher energies.

For the best resolution, it is therefore necessary to use an appropriate ablation laser power. The resulting widths of the time and energy projections and the reduced χ^2 of a Gaussian fit to the ToF spectrum were investigated for different RFQCB fillings. Therefore, pulse power of the ablation laser was varied. For comparison, the same parameters were determined for online ^{114}Pd measurements from CARIBU, which filled the RFQCB only to a very low level. The results are summarized in Fig. 4.11.

Based on these, a "threshold-parameter" was chosen, which is indicated in Fig. 4.11: For all ^{108}Pd spectra, the ToF spectrum was fitted with a Gaussian. If $\chi^2_{\mathrm{red}} > 1.28$, the measurement was assumed to be performed with an overfilled RFQCB and not used for further analysis.

To ensure that the filling of the RFQCB does not have any influence on the measured isotope shift, the center position of the resonance was also determined for different ablation laser powers. They do not show any dependence on the ablation power, as can be seen in Fig. 4.12. It is therefore concluded that the RFQCB characteristics do not lead to a systematic uncertainty, as long as the reduced χ^2 of the ToF distribution is smaller than the threshold .

The RFQCB together with a time-gate for the voltage projection enables a typical enhancement of the resonance signal-to-background ratio in time-resolved CLS of about 10^6 by accu-

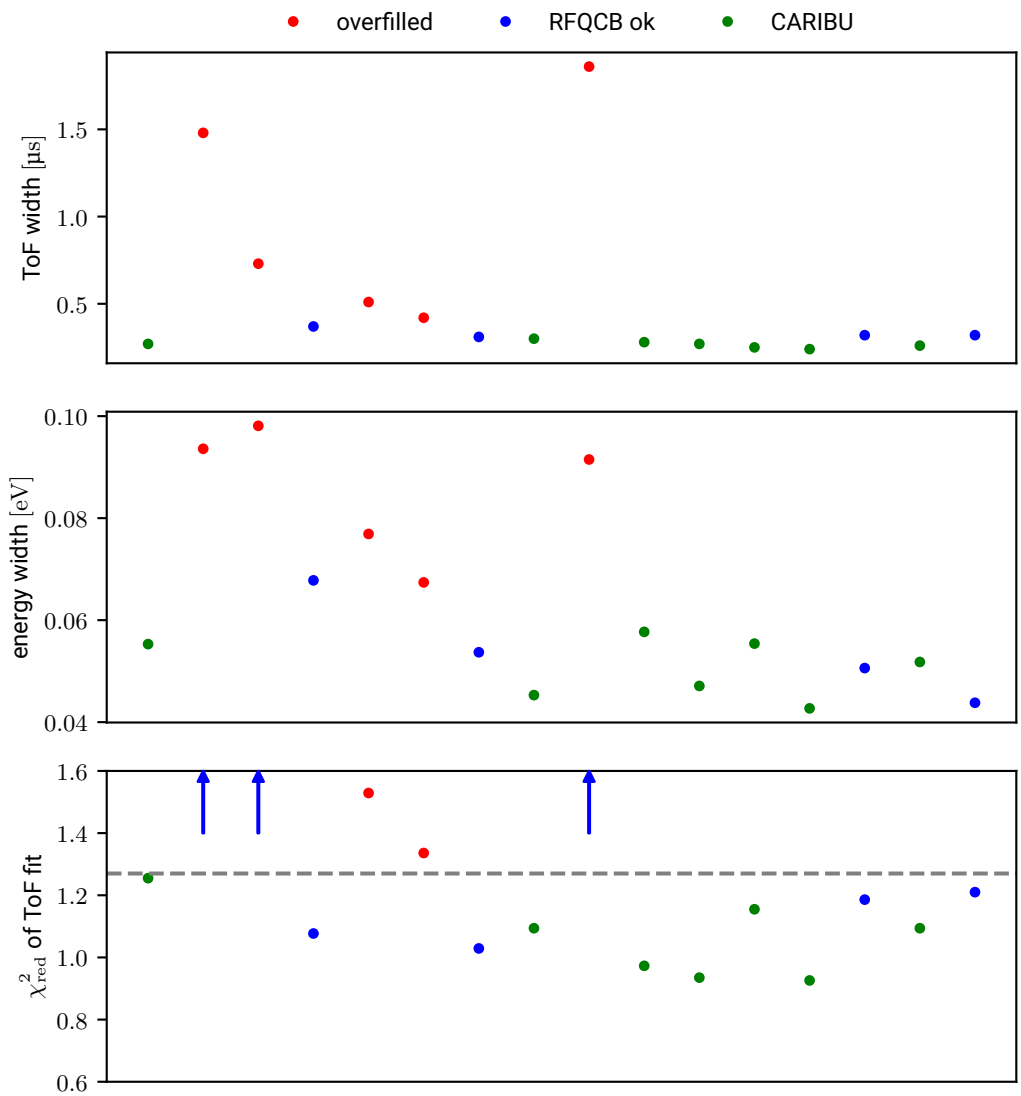

Figure 4.11: Characteristics of resonances for different RFQCB fillings. The top plot shows the width of the time-of-flight (ToF), the middle plot shows the energy width and the bottom plot the reduced χ^2 of a Gaussian fit to the ToF spectrum. In the bottom plot three datapoints from an overfilled RFQCB, indicated by arrows, are out of the range of the vertical axis ($\chi^2 > 3$). Blue data points indicate ^{108}Pd measurements with overfilled RFQCB. Red data points indicate ^{108}Pd measurements with low filling of the RFQCB. Green data points indicate ^{114}Pd measurements from CARIBU with very low filling of the RFQCB. The grey dashed line indicates the "threshold" between overfilled and acceptable filling (see text for more details).

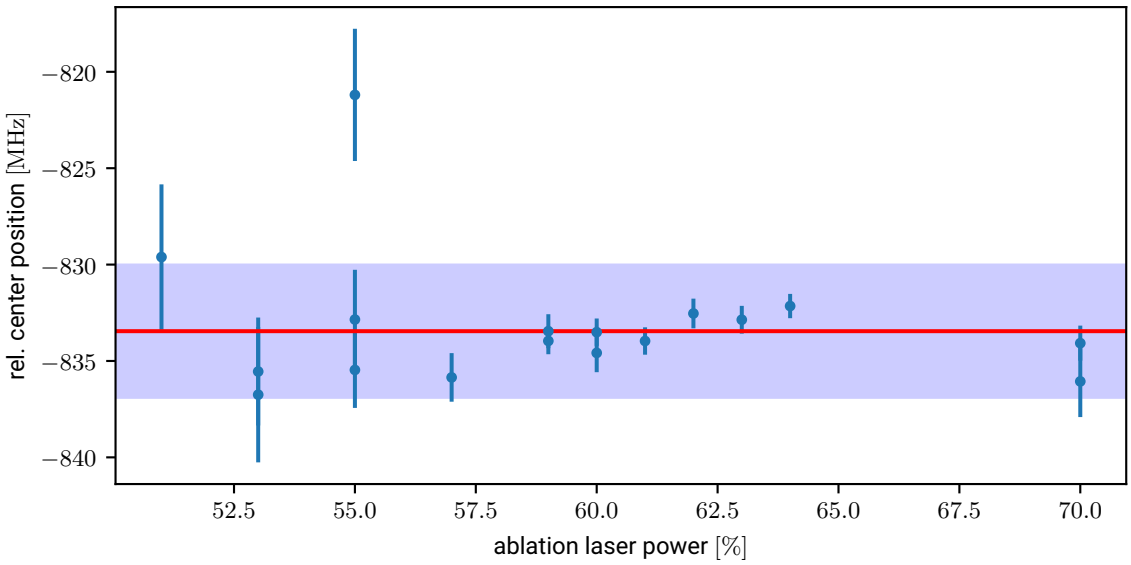

Figure 4.12: Center position of ^{108}Pd spectra using different ablation-laser powers. The red line is the weighted average of all center positions with the standard deviation marked as a blue shaded band. Typically, references were taken around a laser power of $60\,\%$ ($\sim 12\,\mathrm{mJ}$), and the scatter of the reference measurements is much smaller than the standard deviation shown here.

mulating ions for $1\,\mathrm{s}$ and ejecting ion bunches of $1\,\mu\mathrm{s}$ width. For very low ion yields, the accumulation time was increased even further to unprecedented $30\,\mathrm{s}$, i.e., increasing the signal-to-background ratio by 30×10^6.

4.3.6 Charge-Exchange Cell

For palladium, the collision process $\mathrm{Pd}^+ + \mathrm{Mg} \rightarrow \mathrm{Pd} + \mathrm{Mg}^+$ with magnesium was chosen (see Sec. 2.2.2). For the vaporization of magnesium, a new charge-exchange cell was commissioned. A Mg vapor pressure of $1\,\mathrm{Pa}$ requires the Mg to be heated up to at least $428\,^\circ\mathrm{C}$ [113] while standard CEC temperatures stay below $300\,^\circ\mathrm{C}$. The new CEC can be operated at $400 - 500\,^\circ\mathrm{C}$ and is based on the design described in [46], which already fulfilled the requirement of confining the vapor pressure of $10^{-2}\,\mathrm{mbar}$ inside the cell without compromising the vacuum outside ($\sim 10^{-7}\,\mathrm{mbar}$). In a standard CEC, this is enabled by a temperature gradient between the hot cell containing the reservoir of the alkaline metal and the entrance and exit regions. In these regions the vapor condenses and can be recycled by capillary action back to the cell center.

The high melting point of Mg ($650\,^\circ\mathrm{C}$ [113]) disallows this recycling process. To still enable

the confinement of the vapor pressure inside the cell the entrance and exit holes of the cell were cooled to lower temperatures to decrease the vapor pressure at these points to very low values. To reduce the loss of Mg during operation, the entrance and exit pipe diameters were reduced. Although the previous design by [46] could be used to perform charge exchange with Mg on calcium ions [46], it needed improvement as the Mg vapor condensed at the cooled entrance and exit apertures and blocked the beam path.

In the optimized design shown in Fig. 4.13, the central reservoir is heated to create the vapor for neutralization. The apertures are close to the heated center and prevent fast depletion of the reservoir. Due to their high temperature the Mg vapor cannot condensate, which would clog the apertures. The entrance and exit pipes are cooled down to $90\,^{\circ}$C to reduce the vapor pressure and secure the vacuum in the rest of the beamline.

Commissioning of the Charge-Exchange Cell

The efficiency of charge-exchange of Pd ions with Mg was measured with respect to the CEC's temperature. For this, radioactive beam of ^{114}Pd from CARIBU was used. To reduce isobaric contamination from the other strong beam components ^{114}Ag ($t_{1/2} = 4.6\,$s) and ^{114}Rh ($t_{1/2} = 1.85\,$s), the bunching time of the RFQCB was set to $10\,$s, giving the contaminants time to decay. The activity from ^{114}Pd ($t_{1/2} = 2.42\,$min), which predominantly accumulates in the trap, was

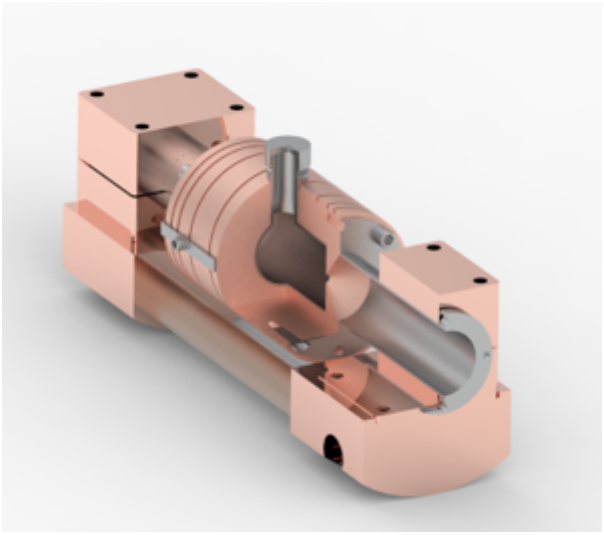

Figure 4.13: New design of the charge-exchange cell suitable for charge-exchange with magnesium. The reservoir and the entrance and exit apertures in the central part can be heated up to 400 - $500\,^{\circ}$C. The tubes along the axis are liquid-cooled to reduce the residual partial magnesium pressure in the entrance and exit regions.

measured on the last silicon detector, at the end of the beamline. The deflector electrode placed in front of this detector, was turned on to deflect all remaining ions, such that only the decay of neutral palladium atoms was detected. During the heating process of the CEC, the activity generated from Pd atoms on the silicon detector increased due to the increasing charge-exchange efficiency. The temperature-dependent charge-exchange efficiency is

$$\eta = \frac{c_{\text{max}} - c(T)}{c_{\text{max}}} \tag{4.6}$$

with the maximum count rate c_{max} on the silicon detector when the CEC is cool and the count rate $c(T)$ at a CEC temperature T. The resulting efficiency curve is shown in Fig. 4.14. A plateau at a maximum efficiency of $87\,\%$ was reached at about $380\,°\text{C}$. The temperature on the horizontal axis gives the temperature measured at the cell's surface, read out with a thermocouple. Spectroscopy measurements were typically performed with temperatures between 350 and $370\,°\text{C}$, which corresponds to $50 - 80\,\%$ neutralization efficiency.

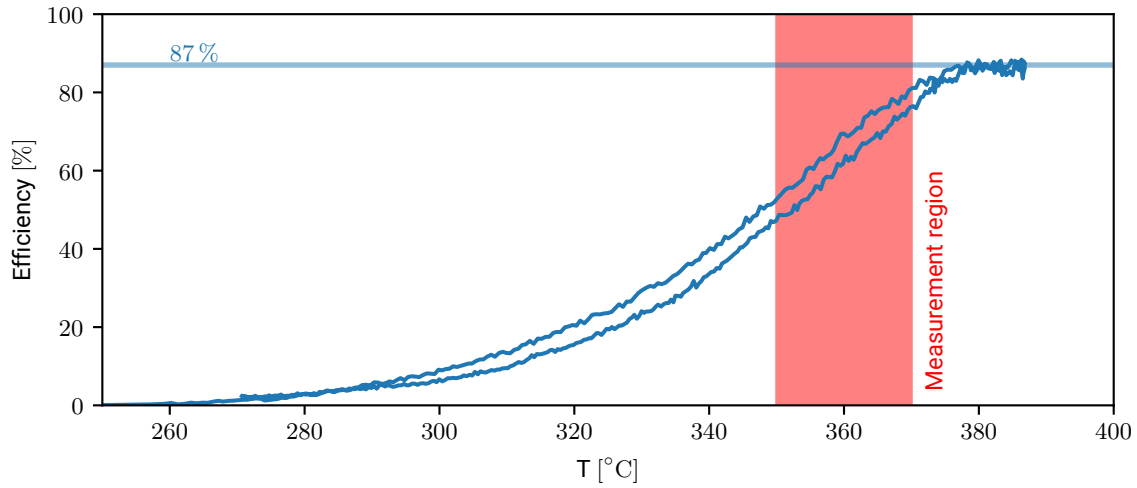

Figure 4.14: Neutralization efficiency of the magnesium charge-exchange cell on Pd^+ measured for different temperatures. The lower curve was measured during the heating process of the cell, while the upper curve was measured during the cooling process. The spectroscopy measurements were performed at temperatures marked by the red shaded area. The difference between the curves can be explained by thermal hysteresis and gives an impression of the margin of uncertainty.

5 Data Analysis

The lead data from COLLAPS and the palladium data from ATLANTIS were recorded and analysed using the same methods. This chapter gives a general overview about how spectra are extracted from the raw data sets, and how laser spectroscopic observables are determined. Details on the analysis of lead or palladium are presented in the subsequent chapters, where the specific procedures are explained in detail and the differential nuclear charge radii, isomer shifts and nuclear moments are extracted.

5.1 Data Sets

The data acquisition system TILDA [114] was used in both experiments. Therefore, the analysis was based on the tool PolliFit, which is distributed together with TILDA.

The complete data set of each beamtime consists of different measurements, called *runs*. A single laser spectroscopy data set contains all information required for the analysis of a run, i.e., the laser frequency and the main acceleration voltage during the measurement, the investigated isotope, the direction of the laser beam (collinear or anticollinear), the amplification factor for the Doppler-tuning voltage and the binned photon data. Typically, each run covers the resonance spectrum of a single isotope. Some runs were performed for tests, or cannot be used due to technical or user errors. These runs have to be excluded from the data analysis. For isotopes with very low yields, in many cases a run was directly added onto previous runs to increase the statistics. These previous runs, even though saved independently, also have to be excluded in order not to use them several times for the data analysis[1].

The main part of a stored run is the binned photon data. The Doppler-tuning voltage applied by TILDA (DAQ voltage), which is scanned and fed to a voltage amplifier, and the photon counts are stored time-resolved in 100 ns bins. The runs contain a separate list of binned counts for each PMT. Thus, the PMTs can be evaluated separately or summed up in any combination. TILDA allows to fragment a run into different *tracks*, where each track covers a specific scan

[1] The advantage of having them individually saved is that in post-beamtime analysis, individual runs can still be excluded in case of a mistake happened during a run (e.g. a blocked laser beam, no protons on target) which is only registered later on.

range. Using tracks can be very efficient in wide-spread hyperfine structures, as regions without resonances can be skipped. Each track is saved separately in the run. For each run, the stabilized pre-acceleration voltage and laser frequency are measured and stored, along with the investigated isotope, the start and stop times of the run, the direction of the laser beam, the number of scans and measurement steps performed, and, if applicable, the runs to which the current one was added on.

Figure 5.1 shows an example of a recorded spectrum. The two-dimensional histogram shows the number of photon counts within 300 ns period color-coded in the time-energy plane. A projection to the time of flight (ToF) axis reveals the ToF spectrum relative to a chosen trigger delay on the RFQCB ejection, and a projection to the beam-energy axis represents the resonance spectrum since the Doppler-tuned energy is in first order linear to the change of laser frequency in the ion's rest frame.

5.1.1 Time Gates

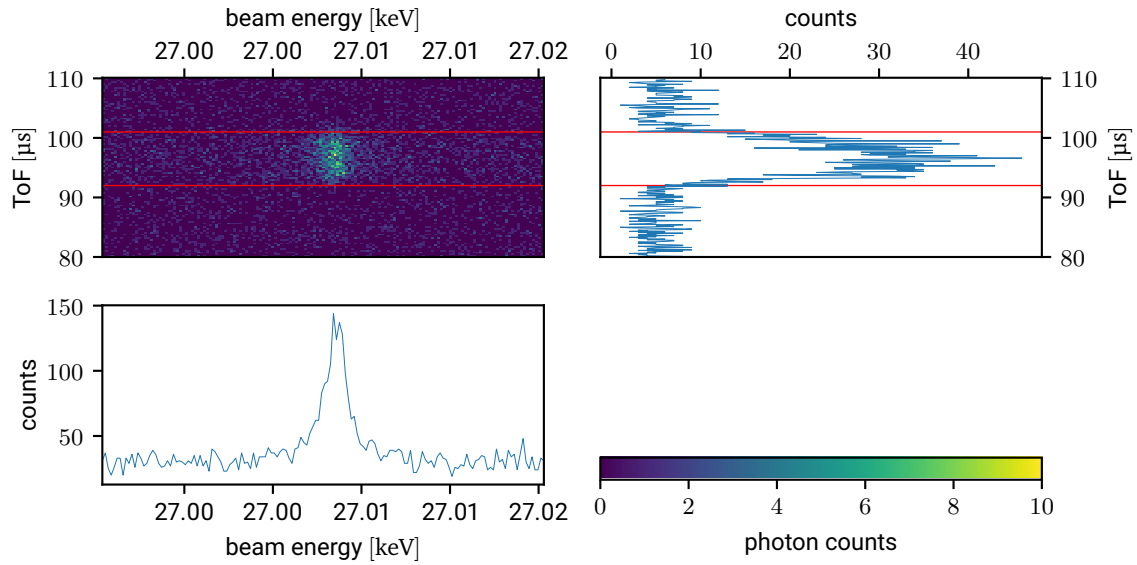

Figure 5.1: Example of the time-resolved counts registered by a single PMT in a reference measurement at COLLAPS. In the top left, the number of counts is color coded in a two-dimensional histogram with the horizontal axis representing the beam energy and the vertical axis representing the time of flight with an arbitrary offset. The projection of the counts onto the energy axis is shown in the bottom plot and the projection of the counts onto the time axis is shown on the right. In order to reduce laser induced background on the voltage projection, only the counts registered within the time gate marked by the red lines were used.

The time-resolved data acquisition allows for the application of timing windows in the post-beamtime analysis instead of hardware gates during the beamtime. The two red lines in Fig. 5.1 indicate the chosen timing window. Their correct setting is crucial for the signal-to-background and, thus, the signal-to-noise ratio of the resonance. Laser-induced fluorescence can only be detected while the atom bunches pass through the detection region. During the remaining time, the PMTs only detect a background signal, mainly produced by laser stray light. Exclusion of these periods reduces the background to the stray light within the short periods and beam-induced background caused by inelastic collisions of the atoms with residual gas and the de-excitation of longer-lived atomic states that have been populated in charge-exchange reactions. An important part of the palladium data analysis was the determination of an unbiased time window for each isotope, as discussed in Sec. 7.1.3.

5.2 Fitting Spectra

The fitting of the spectra was performed using PolliFit[114], a python-based software module distributed with and tailored to the data sets generated by TILDA. The program can load one or more runs at once and fit them either individually or simultaneously with or without shared parameters.

5.2.1 Voltage to Frequency Conversion

In a first step, the total acceleration voltage U_{tot} has to be converted into the Doppler-shifted laser frequency in the particle rest frame. For this, the main acceleration voltage U_{acc}, monitored with a high-precision high-voltage divider at the RFQCB, and the additionally applied Doppler-tuning voltage U_{scan} at the CEC are required. To derive U_{scan} from the value applied by TILDA to an amplifier that generates the CEC voltage, the amplification factor has to be determined. Therefore, U_{scan} is measured with another high-precision high-voltage divider as a function of the value set by TILDA. These measurements are referred to as *Kepco measurements* and an example is shown in Fig. 5.2. The amplification factor is determined by fitting a linear function to a Kepco measurement.

This amplified voltage U_{scan} is added to the main acceleration voltage to $U_{\text{tot}} = U_{\text{acc}} + U_{\text{scan}}$ to calculate the total acceleration voltage of each measurement step. U_{tot} is transformed to a laser frequency ν in the particle rest-frame by the Doppler formula and according to the relation of the acceleration voltage and the particle velocity, i.e., by

$$\nu = \nu_{a/c} \cdot \frac{eU + mc^2 \pm \sqrt{eU(eU + 2mc^2)}}{mc^2} \tag{5.1}$$

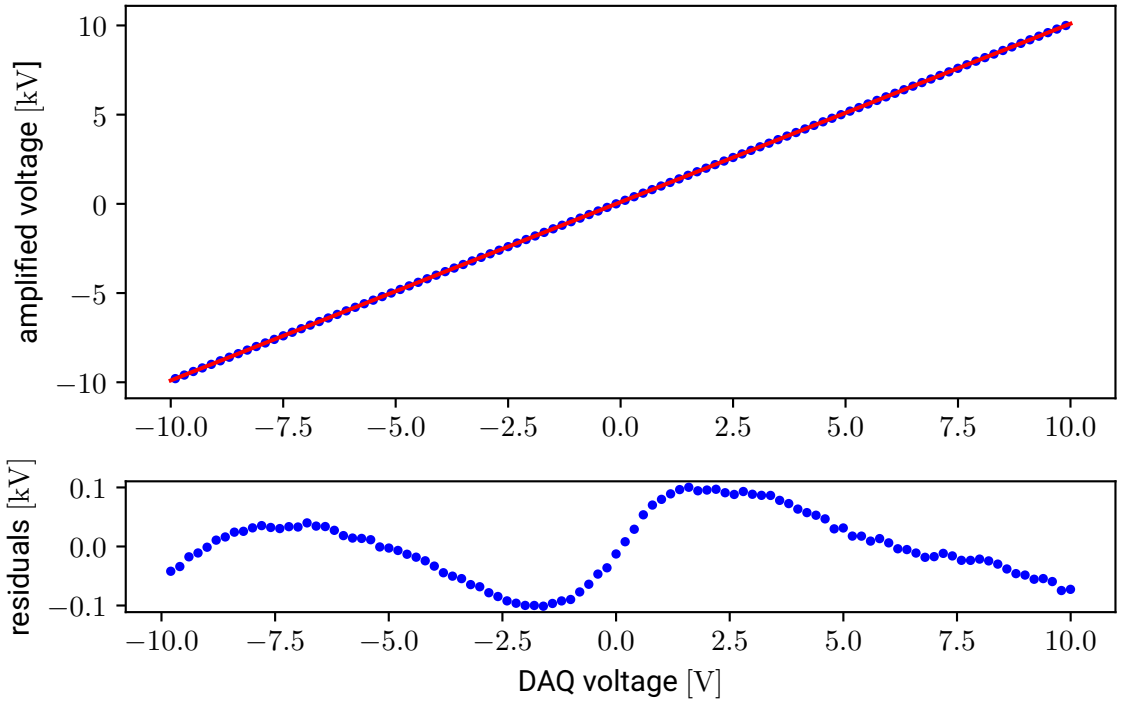

Figure 5.2: The top plot shows an example of a Kepco measurement performed at COLLAPS with the set DAQ-voltage on the horizontal axis and the measured Doppler-tuning voltage on the vertical axis. A linear function is fitted to the data to determine the amplification factor. The bottom plot shows the residuals of the data to the fitted function. With an amplification factor of 999.9, the residuals range from 7 to $70\,\mathrm{ppm}$ of the amplified voltage, depending on the applied DAQ voltage.

with the laboratory laser frequency $\nu_{a/c}$ in anti-/collinear geometry, the mass m and the charge q of the ions and the speed of light c.

5.3 Fit Parameters

The resonance spectra are fitted with a function depending on the center of gravity of the transition frequency, i.e., the fine-structure transition frequency, the width and height of the resonance and, additionally for $I \neq 0$ isotopes, the hyperfine parameters A and B of both atomic levels, the relative intensities of the resulting hyperfine peaks and the background count rate.

5.3.1 Lineshapes

Additionally to the natural line width $\delta\nu_{\text{nat}}$ introduced in Sec. 4.1, collisional broadening [88] and saturation power broadening [115] are homogeneous broadening effects, that lead to a Lorentzian resonance profile $L(\nu)$ with increased widths.

The Doppler broadening is an inhomogeneous broadening effect, where the transition probability depends on external degrees of freedom [115]. In this case it depends on the particle's velocity. Inhomogeneous broadening is additionally correlated to the distribution of the external degree of freedom. In the case of a thermal velocity distribution this includes a Gaussian lineshape $G(\nu)$. Since both categories of broadening are present in collinear laser spectroscopy, both profiles are convoluted to the Voigt profile [115]

$$I(\nu) = I_0 \int G(\nu')L(\nu - \nu')\,\mathrm{d}\nu' \tag{5.2}$$

$$I(\nu) = C \int \frac{\exp(-(\nu' - \nu_0)^2/2\sigma^2)}{(\nu - \nu')^2 + (\gamma/2)^2}\,\mathrm{d}\nu' \tag{5.3}$$

with the central frequency ν_0, the Lorentzian full width at half maximum (FWHM) γ, the Gaussian standard deviation σ of the Maxwell-Boltzmann distribution and the total intensity C. Such a Voigt profile is fitted to the atomic spectra.

5.3.2 Spin-Zero-Nuclei

For isotopes without nuclear spin, the free fitting parameters are the Voigt width parameters σ and γ, the center position, the background, coming from stray light and collisions, and the signal intensity, which is related to the number of atoms interacting with the laser, the transition strength and the laser power, which is assumed to be constant during a run. With the necessary transformations described in this section, the center position directly allows to extract the fine structure transition frequency.

5.3.3 Hyperfine Splitting

As described in Sec 2.2.3, the spectra of isotopes with a non-zero nuclear spin show hyperfine splitting. For the extraction of observables from a hyperfine spectrum, a sum of several Voigt profiles is fitted to the data. The position of the hyperfine peaks is defined by the hyperfine parameters A and B, introduced in Eqs. (2.44) and (2.46), for both participating atomic levels. The hyperfine formulas are incorporated into the fitting routine, such that the hyperfine parameters of the upper (A_u, B_u) and lower (A_l, B_l) atomic level are free fitting parameters. It

is essential to carefully identify the hyperfine structure ”by hand”, since often, the assignment of quantum numbers to the individual peaks is not unambiguous (especially if the nuclear spin is not known a priori). The relative intensities of the hyperfine peaks are, in principle, defined by the Racah W-coefficients, but optical pumping during seceral transition cycles can shift the relative intensities and, thus, they have been adopted as free parameters in all cases with sufficient statistics. In some cases, however, statistics required to reduce the number of free parameters and the line intensities were fixed to the theoretical expectation.

Typically, the hyperfine spectra of each isotope were measured in several runs. The spectra of these runs were fitted simultaneously with shared hyperfine parameters. The B-ratio ${}^{B_u}/_{B_l}$ derived from an isotope measured with the best statistics achieved, was fixed during the fitting of all other isotopes, removing B_l from the free fitting parameters. In the cases where isomeric states where observed, the hyperfine parameter ratios ${}^{A_u}/_{A_l}$ and ${}^{B_u}/_{B_l}$ of the isomeric states were shared with the ratios of the ground states, ignoring a possible (small) hyperfine structure anomaly.

For some isotopes and isomers, the nuclear spins are not known from literature. In order to assign the spin, the fits were performed using different hypothetical spin values which generate different hyperfine structures and thus, fit functions $\mathrm{cts}(\nu)$. The resulting reduced χ^2_{red} values of these fits

$$\chi^2_{\mathrm{red}} = \frac{\chi^2}{N} = \frac{1}{N}\sum_{\nu}\frac{(\mathrm{cts}_\nu - \mathrm{cts}(\nu))^2}{\sigma^2}, \tag{5.4}$$

with measured counts cts_ν for each frequency ν, the standard deviation of the counts $\sigma = \sqrt{\mathrm{cts}_\nu}$ and the number N of measurement points, i.e., the number of voltage steps in a run, gives information about the goodness of the fit. The closer χ^2_{red} is to 1, the better is the fit. Therefore, the comparison of χ^2_{red} for different nuclear spins can give a hint to the right spin assignment. The spin assignment can also be verified by checking the hyperfine parameters and their ratios as well as the resulting isotope shifts for plausibility.

5.4 Isotope Shifts

Since the isotope shift is calculated by $\delta\nu^{A,A_{\mathrm{ref}}} = \nu^A - \nu^{A_{\mathrm{ref}}}$, each isotope shift measurement consists of a set of runs which includes spectra of the reference isotope A_{ref} and spectra of the isotope of interest A. They were measured in the order $A_{\mathrm{ref}} - n \cdot A - A_{\mathrm{ref}}$, where n indicates the number of runs performed on the isotope of interest. From each of the $n \cdot A$ runs, a center frequency can be extracted and a corresponding reference center position $\nu^{A_{\mathrm{ref}}}$ was extracted from the previous and subsequent reference runs A_{ref}. Since voltage drifts or laser frequency drifts can lead to drifts in the extracted center positions over time, the reference

center position is linearly interpolated by

$$\nu^{A_{\text{ref}}} = \nu_0 + (t - t_0)\frac{\nu_1 - \nu_0}{t_1 - t_0}, \tag{5.5}$$

from the two reference positions ν_0, ν_1 measured before (t_0) and after (t_1) the isotope of interest, which was measured at the time t. This interpolated reference center position was subtracted from the fitted center position of A to calculate the isotope shift. If more than one run for isotope A was performed, the weighted mean was calculated to determine the final isotope shift.

5.5 King Plot Analysis

As described in Sec. 2.2.3, one portion of the isotope shift is caused by the difference in the nuclear charge radii. Therefore, the differential ms nuclear charge radius between two isotopes can be extracted from the measured isotope shift by Eq. (2.42). With the help of a King-plot procedure, i.e., by fitting Eq. (2.41) to known differential ms nuclear charge radii and measured isotope shifts, the field shift and mass shift factors F and K_{MS} can be extracted. The isotope shifts of the stable isotopes measured within this work are used while the corresponding differential ms nuclear charge radii are taken from literature.

The fitting of the linear function to the modified isotope shifts and modified differential nuclear charge radii (see Eq. (2.2.3)) was performed using the python package qspec [116]. To reduce the correlation between the offset and slope parameters of this linear fit, the axis of the modified radius was shifted by a constant α, as proposed by [117]:

$$\widetilde{\delta\nu} = K_\alpha + F\left(\widetilde{\delta\langle r_c^2\rangle}^{A,A'} - \alpha\right) \tag{5.6}$$

K_α can be calculated back to the actual mass shift factor by $K_{\text{MS}} = K_\alpha - F\alpha$.

5.5.1 Literature Nuclear Charge Radii

Fricke and Heilig have compiled nuclear charge radii of all investigated stable isotopes in [55]. For the stable isotopes of lead and palladium, the Barret equivalent radii $R_{k\alpha}$ from muonic x-ray spectroscopy data are listed as well as the V_2 ratios, derived from high energy elastic electron scattering. The differential ms nuclear charge radius between two isotopes A and

A' can be calculated from these listed values with the help of Eq. (2.5) by

$$\begin{aligned}\delta\langle r_c^2\rangle^{A,A'} =& \langle r_c^2\rangle^{A} - \langle r_c^2\rangle^{A'} \\ =& \left(\frac{R_{k\alpha}^{A}}{V_2^{A}}\right)^2 - \left(\frac{R_{k\alpha}^{A'}}{V_2^{A'}}\right)^2 \\ =& \left(\frac{R_{k\alpha}^{A}}{V_2^{A}} - \frac{R_{k\alpha}^{A'}}{V_2^{A'}}\right)\left(\frac{R_{k\alpha}^{A}}{V_2^{A}} + \frac{R_{k\alpha}^{A'}}{V_2^{A'}}\right). \end{aligned} \tag{5.7}$$

The uncertainties can be approximated by

$$\Delta\delta\langle r_c^2\rangle^{A,A'} \approx \frac{\Delta\delta R_{k\alpha}^{A,A'}}{V_2^{A}}\left(\frac{R_{k\alpha}^{A}}{V_2^{A}} + \frac{R_{k\alpha}^{A'}}{V_2^{A'}}\right), \tag{5.8}$$

with the uncertainty of the differential Barret radius $\Delta\delta R_{k\alpha}^{A,A'}$, which is also listed in [55]. For this approximation, $V_2^{A'} \simeq V_2^{A}$ is assumed, which is often sufficiently accurate, and the term in the first parentheses of Eq. (5.7) is about two orders of magnitude smaller than the term in the second parentheses. The contribution of the V_2-uncertainties would be of the order of 10^{-4} [55] and can therefore be neglected.

This procedure yields at least two pairs of differential ms nuclear charge radii and corresponding uncertainties, which are necessary to perform a king fit. The uncertainty of the differential radii contributes significantly to the uncertainty of the extracted mass shift and field shift factors and is usually the limiting factor for the accuracy of the charge radii, rather than the isotope-shift uncertainty.

6 Lead

This section provides a detailed evaluation of the lead data. The extracted isotope shifts and hyperfine parameters are presented and the differential nuclear charge radii and the nuclear moments are extracted. The section concludes with a discussion of the results in comparison to the semi-magic tin isotopes and theoretical caculations.

6.1 Data Analysis Specifics

6.1.1 Dataset

The measurements on lead were performed during one beamtime at COLLAPS. All stable isotopes ^{208,207,206}Pb were investigated, with ^{208}Pb, the naturally most abundant isotope, serving as the reference for the isotope shift measurements. For an extensive investigation of the lead isotopic chain, collinear laser spectroscopy was also performed on the radioactive isotopes $^{187-205}$Pb including isomeric states with half-lifes down to $4\,$s. Each measurement targeted a single isotope but can also include an isomeric state. The main acceleration voltage between ISCOOL and the COLLAPS beamline is measured before and after each spectroscopy measurement and stored in the measurement file. The wavemeter used to stabilize the spectroscopy laser was calibrated before each isotope-shift measurement. Therefore, the complete measurement routine consisted of: *wavemeter calibration* $-$ A_{ref} $-$ $n \cdot A$ $-$ A_{ref}. For all isotopes the laser was stabilized to the same frequency of $(414\,893\,775 \pm 1)\,$MHz. It should be noted that the uncertainty is systematic and does not represent statistical variations that are rather on the $< 1\,$MHz scale.

6.1.2 Scanning Voltages

As described in Sec. 5.2.1, the amplification factor for the Doppler-tuning voltage is extracted from a linear fit to a Kepco measurement (see Sec. 5.2.1). The amplification factor was repeatedly measured during the beamtime. Figure 6.1 shows that the resulting offset and amplification factor drifted over time. A linear function was fitted to both and used to interpolate

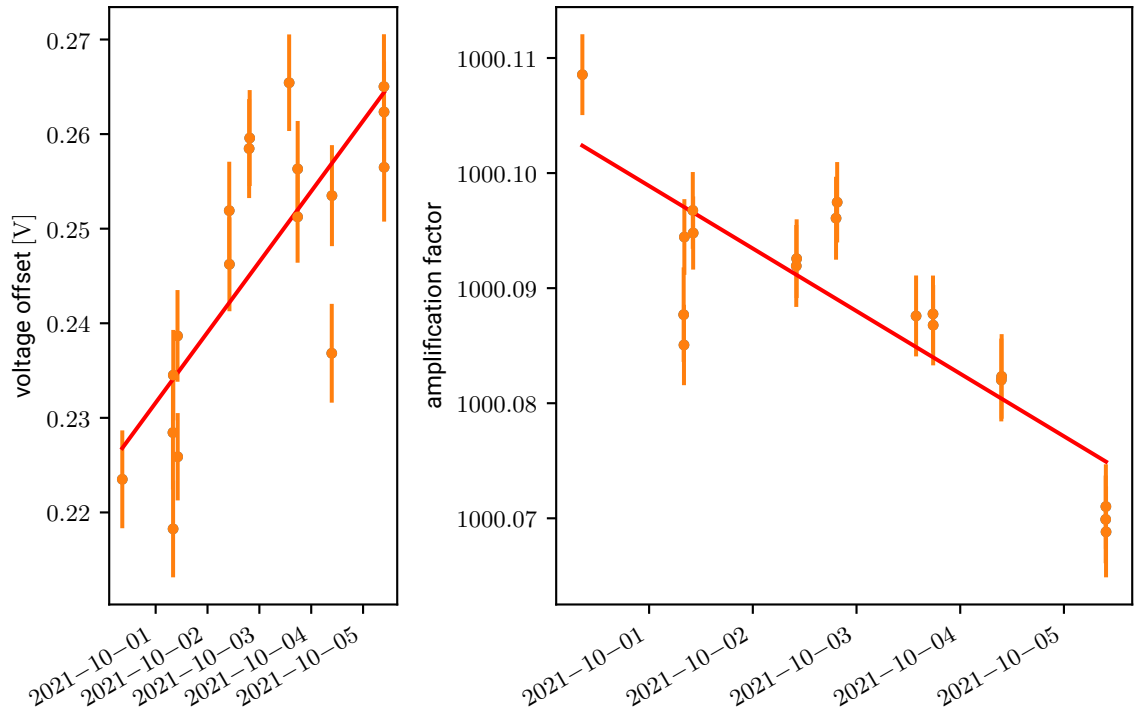

Figure 6.1: Voltage offset and amplification factors derived from the different amplification-factor measurements performed during the beamtime. A linear function in time is fitted to the offset and to the amplification factor for interpolation.

the voltage offset and amplification factor for each run.

6.1.3 Fitting

For the evaluation of the data, the counts measured on all four PMTs were summed into a single spectrum and fitted with Voigt profiles.

Hyperfine Splitting

The first spectra analyzed were the hyperfine spectra of ^{197}Pb and ^{199}Pb, which had the best statistics and highes signal rates, in order to extract the B-ratio $^{B_u}/_{B_l}$ from these two isotopes with $I > {}^1/_2$. Each isotope was fitted individually. For ^{197}Pb, six runs were evaluated, and for ^{199}Pb, four runs were analyzed. For each isotope all runs were fitted simultaneously and the hyperfine parameters for the ground and isomeric state were shared between the different runs. The B ratio was shared between the ground and isomeric states. The ratio

was calculated for each isotope and from these two values, the mean was determined to be ${}^{B_u}/_{B_l} = -0.0938 \pm 0.0034$.

In the next step, all isotopes and isomers were fitted with the B-ratio of the ground and isomeric state fixed to ${}^{B_u}/_{B_l} = -0.0938$. Again, for each isotope, all runs were fitted simultaneously while all A-parameters of ground and isomeric state and the B-parameter of the lower atomic level of ground and isomeric state were shared between different runs. The results are shown in Tab. 6.1.

Table 6.1: A and B parameters for the $6s^2 6p 7s\ ^3\mathrm{P}_1$ (upper) and $6s^2 6p^2\ ^1\mathrm{D}_2$ (lower) levels along the isotopic chain of lead, including observed isomeric states. The statistical uncertainties are given in parentheses. For B_u, they include the uncertainties from B_l and from the B-ratio.

Isotope	I	A_u [MHz]	A_l [MHz]	B_l [MHz]	B_u [MHz]
^{207}Pb	1/2	8805.89 (60)	609.83 (33)		
^{205}Pb	3/2	2111.8 (25)	144.9 (15)	282 (11)	-26.5 (14)
^{203}Pb	5/2	2039.90 (65)	140.77 (34)	133.8 (18)	-12.55 (48)
^{203m}Pb	13/2	-1171.54 (24)	-80.32 (13)	641.4 (23)	-60.2 (22)
^{202m}Pb	9	-187.92 (24)	-12.46 (12)	713.7 (37)	-66.9 (25)
^{201}Pb	5/2	2008.36 (70)	139.11 (42)	-41.2 (23)	3.86 (26)
^{201m}Pb	13/2	-1196.60 (15)	-81.782 (81)	651.8 (15)	-61.1 (22)
^{199}Pb	3/2	-5311.59 (97)	-363.83 (57)	41.5 (16)	-3.90 (21)
^{199m}Pb	13/2	-1227.723 (90)	-83.861 (58)	622.2 (13)	-58.4 (21)
^{197}Pb	3/2	-5325.8 (13)	-364.32 (80)	-79.5 (19)	7.46 (32)
^{197m}Pb	13/2	-1262.167 (94)	-86.055 (57)	544.0 (11)	-51.0 (19)
^{195}Pb	3/2	-5361.1 (20)	-369.2 (11)	-147.5 (22)	13.84 (54)
^{195m}Pb	13/2	-1293.55 (10)	-88.096 (61)	434.6 (12)	-40.8 (15)
^{193}Pb	3/2	-5381.9 (27)	-368.7 (15)	-193.2 (28)	18.12 (71)
^{193m}Pb	13/2	-1320.93 (15)	-90.200 (95)	304.1 (18)	-28.5 (10)
^{191}Pb	3/2	-5405.1 (20)	-369.8 (12)	-222.5 (33)	20.87 (82)
^{191m}Pb	13/2	-1342.99 (14)	-91.578 (78)	144.1 (14)	-13.51 (51)
^{189}Pb	3/2	-5467.1 (17)	-373.2 (10)	-233.8 (25)	21.93 (83)
^{189m}Pb	13/2	-1362.31 (33)	-92.70 (19)	-31.7 (33)	2.97 (33)
^{187}Pb	3/2	-5553.3 (30)	-378.3 (18)	-221.1 (51)	20.73 (89)
^{187m}Pb	13/2	-1382.26 (89)	-94.25 (53)	-201 (11)	18.8 (12)

Verification of Spins

Although the nuclear spins of the investigated lead isotopes are already reported in [51], alternative spins were tested while fitting the measured hyperfine spectra. A reduced χ^2-analysis confirmed the previously known spins. Figure 6.2 shows as an example the χ^2 for the isomeric state of ^{197}Pb.

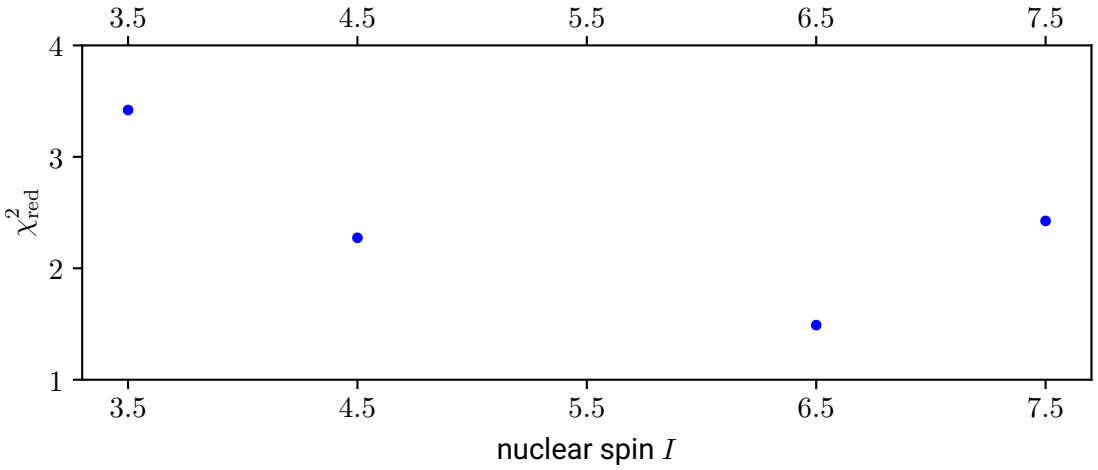

Figure 6.2: χ^2-analysis of ^{197m}Pb. The spectra were fitted for different isomeric spins. The χ^2 of each fit is plotted over the assigned nuclear spin. For $I = {}^{13}/_{2}$ the best χ^2 is achieved. $I = {}^{11}/_{2}$ has not been tested, since the $N = 126$ shell does not include a level with a total angular momentum of ${}^{11}/_{2}$.

6.1.4 Isotope and Isomeric Shifts

The isotope shifts were determined following the procedure described in Sec. 5.4. The isomeric shift is an additional fit parameter of the total fit function, defining the position of the fine-structure transition in the isomer relative to the one in the nuclear ground state. For each isotope, it is set as a shared variable between the available runs during simultaneous fitting.

6.1.5 Uncertainties

The center positions of both the reference and the isotope of interest, come with a fit uncertainty from the least-squares analysis. Since Eq. (5.5) interpolates the center position of the reference, the uncertainty of the reference center-position is calculated by

$$\Delta\nu_{\mathrm{ref}} = \sqrt{\left(\frac{t_1 - t}{t_1 - t_0}\Delta\nu_0\right)^2 + \left(\frac{t - t_0}{t_1 - t_0}\Delta\nu_1\right)^2} \tag{6.1}$$

with the fit uncertainties $\Delta\nu_0$ and $\Delta\nu_1$ of the two individual center positions. This uncertainty $\Delta\nu_{\mathrm{ref}}$ is added quadratically to the fit uncertainty of the center position of a single run on the isotope of interest. This yields the total fit uncertainty $\Delta\delta\nu_i^{A,A'}$ of the isotope shift, determined by a single run. For the isotopes, where more than one run was used to determine the isotope shift, the final statistical uncertainty was conservatively chosen to be the maximum of the

standard deviation and the mean of the fit uncertainties $\Delta\delta\nu_i^{A,A'}$.

Since the isomeric shift was a shared variable in the fitting routine, its fit uncertainty can directly be used as the total statistical uncertainty.

In addition to these statistical uncertainties, there are also systematic effects contributing to the total uncertainty. For the determination of the systematic uncertainty, the procedure described in [43] is used. It takes into account that the ion velocity comes with an uncertainty due to the ISCOOL-voltage uncertainty, the Doppler-tuning-voltage uncertainties and the mass uncertainties. The ISCOOL voltage U_{acc} is read out over a high-voltage divider with a scaling ratio of $M = 5963.39$ and its uncertainty $\frac{\Delta M}{M} = 1 \cdot 10^{-5}$, which defines the ISCOOL-voltage uncertainty.

The uncertainty of the Doppler-tuning voltage comes from the uncertainty in the evaluation of the Kepco measurements. The standard deviation of the residuals is taken as the amplification factor uncertainty, leading to a relative Doppler-tuning-voltage uncertainty of $5 \cdot 10^{-6}$. This uncertainty can be neglected compared to the uncertainty of the ratio $\frac{\Delta R}{R}$ of the voltage divider, used to perform the Kepco measurements. The relative uncertainty of the scanning voltage is therefore considered to be $\frac{\Delta U_{\text{scan}}}{U_{\text{scan}}} = \frac{\Delta R}{R} = 9.997 \cdot 10^{-5}$. The systematic uncertainty of the isotope shift coming from the acceleration voltages and masses can be estimated by [43]

$$\Delta\delta\nu^{A,A'} = \nu_L \sqrt{\frac{eU_{\text{acc}}}{2mc^2}} \left[\frac{1}{2} \left(\frac{U_{\text{scan}}}{U_{\text{acc}}} + \frac{\delta m}{m} \right) \frac{\Delta M}{M} + \frac{U_{\text{scan}}}{U_{\text{acc}}} \frac{\Delta U_{\text{scan}}}{U_{\text{scan}}} + \frac{\Delta m_A}{m} + \frac{\Delta m_{A'}}{m} \right], \tag{6.2}$$

with the assumptions $m \simeq m_A \simeq m_{A'}$ and $\delta m = m_A - m_{A'}$ and with the mass uncertainties Δm_A, $\Delta m_{A'}$.

From the laser frequency stabilization by the wavemeter, an uncertainty of 1 MHz, coming from the calibration laser, can be assumed [118, 119], which is added quadratically to the systematic uncertainties. The isotope and isomeric shifts with all uncertainties are listed in Tab. 6.2.

6.1.6 Nuclear Moments

The nuclear magnetic and electric moments of lead are calculated from the measured A and B parameters according to Eq. (2.48). The magnetic moment of ^{207}Pb, with a known value of $\mu_{207} = (0.591\,02 \pm 0.000\,18)\,\mu_{\text{N}}$ [61] and measured by nuclear magnetic resonance spectroscopy, was used as a reference to calculate the nuclear magnetic moments of all investigated isotopes and isomers. The calculation was performed twice, once using the A parameters of the upper atomic level and once of the lower level. The results are given in Tab. 6.3. Since the relative uncertainties of the A-parameter of the upper level are smaller by almost an order of

Table 6.2: Measured isotope shifts $\delta\nu^{A,208}$ relative to ^{208}Pb and isomeric shifts $\delta\nu^{m,g}$ relative to the ground state along the lead isotopic chain. Statistical uncertainties are given in parentheses, systematic uncertainties in square brackets.

Isotope	$\delta\nu^{A,208}$ [MHz]	$\delta\nu^{m,g}$ [MHz]
^{187}Pb	$-22804.3(26)[1.9]$	$-728.5(37)[19]$
^{188}Pb	$-21355.8(19)[18]$	
^{189}Pb	$-20590.4(03)[18]$	$-598.5(17)[17]$
^{190}Pb	$-19259.9(14)[17]$	
^{191}Pb	$-18689.9(08)[17]$	$-405.5(16)[16]$
^{192}Pb	$-17431.4(13)[16]$	
^{193}Pb	$-17050.9(07)[15]$	$-133.6(18)[15]$
^{194}Pb	$-15698.4(12)[15]$	
^{195}Pb	$-15505.7(04)[14]$	$220.7(12)[14]$
^{196}Pb	$-13926.7(08)[14]$	
^{197}Pb	$-13890.6(08)[13]$	$705.1(10)[14]$
^{198}Pb	$-11994.0(01)[13]$	
^{199}Pb	$-11849.2(03)[12]$	$983.5(09)[13]$
^{200}Pb	$-9860.4(19)[12]$	
^{201}Pb	$-9419.5(04)[11]$	$1060.5(09)[12]$
^{202}Pb	$-7544.0(21)[11]$	$-49.3(14)[11]$
^{203}Pb	$-7008.2(09)[11]$	$1239.8(16)[11]$
^{204}Pb	$-5130.5(21)[10]$	
^{205}Pb	$-4528.3(37)[10]$	
^{206}Pb	$-2715.5(09)[10]$	
^{207}Pb	$-1696.0(05)[10]$	

magnitude than the ones of the lower level, which also leads to smaller uncertainties in the extracted magnetic dipole moments, the nuclear magnetic dipole moments extracted from the upper level are further discussed in Sec. 6.2.

The electric quadrupole moments can be calculated from the field-gradient and the hyperfine parameter B (see Eq. (2.47)), according to [120]

$$Q(^{A}\mathrm{Pb}) = -0.00868(52) \cdot B(^{A}\mathrm{Pb}; 6p7s\ ^{3}P_1)\ \frac{\mathrm{b}}{\mathrm{MHz}}. \tag{6.3}$$

This is used to calculate the electric quadrupole moments from the B parameters of the upper level in MHz. The results are also provided in Tab. 6.3.

Table 6.3: Nuclear magnetic dipole moments determined from the A parameters of the upper (μ_u) and of the lower (μ_l) level and nuclear electric quadrupole moments determine from the B parameter of the upper level.The statistical uncertainties are given in parentheses.

Isotope	μ_l [μ_N]	μ_u [μ_N]	Q [b]
^{187}Pb	$-1.099(5)$	$-1.1174(9)$	$-0.180(11)$
^{187m}Pb	$-1.187(7)$	$-1.2053(11)$	$-0.163(10)$
^{189}Pb	$-1.084(3)$	$-1.1001(7)$	$-0.109(11)$
^{189m}Pb	$-1.167(3)$	$-1.1879(8)$	$-0.026(2)$
^{191}Pb	$-1.074(4)$	$-1.0876(8)$	$-0.181(11)$
^{191m}Pb	$-1.153(1)$	$-1.1710(7)$	$0.117(7)$
^{193}Pb	$-1.071(5)$	$-1.0829(8)$	$-0.157(9)$
^{193m}Pb	$-1.136(2)$	$-1.1519(7)$	$0.248(15)$
^{195}Pb	$-1.073(3)$	$-1.0788(8)$	$-0.120(7)$
^{195m}Pb	$-1.109(1)$	$-1.1279(7)$	$0.354(21)$
^{197}Pb	$-1.059(2)$	$-1.0716(7)$	$-0.065(4)$
^{197m}Pb	$-1.084(1)$	$-1.1005(7)$	$0.443(27)$
^{199}Pb	$-1.057(2)$	$-1.0688(7)$	$0.034(2)$
^{199m}Pb	$-1.056(1)$	$-1.0705(6)$	$0.507(30)$
^{201}Pb	$0.674(2)$	$0.6735(5)$	$-0.034(2)$
^{201m}Pb	$-1.030(1)$	$-1.0434(6)$	$0.531(32)$
^{202m}Pb	$-0.217(2)$	$-0.2269(3)$	$0.581(35)$
^{203}Pb	$0.682(2)$	$0.6841(5)$	$0.110(7)$
^{203m}Pb	$-1.011(2)$	$-1.0215(6)$	$0.522(31)$
^{205}Pb	$0.702(7)$	$0.7082(9)$	$0.230(14)$
^{207}Pb	$0.5910(5)$	$0.5910(2)$	

6.1.7 Nuclear Charge Radii

All charge radii information of the stable isotopes required for the King-plot analysis is summarized in Tab. 6.4. It includes the Barret equivalent radii, the uncertainties of the differential Barret radii, and the V_2-ratios of stable isotopes, all taken from [55]. The resulting differential ms charge radii in the last column were calculated according to Eq. (5.7) and their uncertainties were derived from the uncertainties of the differential Barret radii using Eq. (5.8).

King-Plot Analysis

The corresponding isotope shifts from Tab. 6.2 and charge radii from Tab. 6.4 are fitted with the function given in Eq. (5.6), yielding $K_\alpha = (55\,452 \pm 301)$ u GHz and $F = (18.6 \pm 1.9)$ GHz/fm^2. The remaining correlation between K_α and F is -0.0006 for $\alpha = 2622.8375$ u fm^2. The mass shift factor K is calculated as $K = K_\alpha - F\alpha = (6668 \pm 4992)$ u GHz, which is in agreement

Table 6.4: Barret radii $R_{k\alpha}$, uncertainties of the differential Barret radii $\Delta\delta R_{k\alpha}$ and the corresponding V_2 ratios taken from [55]. They are used to calculate the differential ms charge radii $\delta\langle r_c^2\rangle^{A,208}$ for the King-plot analysis. Their uncertainties are given in parentheses and are calculated from the differential Barret radii uncertainties $\Delta\delta R_{k\alpha}$ from [55] according to Eq. (5.8).

Isotope	$R_{k\alpha}$ [fm]	V_2	$\Delta\delta R_{k\alpha}^{A,208}$ [10^{-3}fm]	$\delta\langle r_c^2\rangle^{A,208}$ [fm^2]
^{204}Pb	7.0036 (3)	1.27808	0.2	-0.2420 (17)
^{206}Pb	7.0169 (2)	1.27811	0.2	-0.1293 (17)
^{207}Pb	7.0222 (3)	1.27809	0.3	-0.0828 (26)
^{208}Pb	7.0316 (1)	1.27805		

with the mass shift factor $K = (6625 \pm 4976)$ u GHz derived with a fixed $\alpha = 0$ u fm^2. Figure 6.3 illustrates the King plot, with the fitted data points in black and all measured isotopes shifts from Tab. 6.2 marked on the fitted linear function to visualize the extraction of their ms nuclear charge radii relative to ^{208}Pb. The extracted differential charge radii of all isotopes

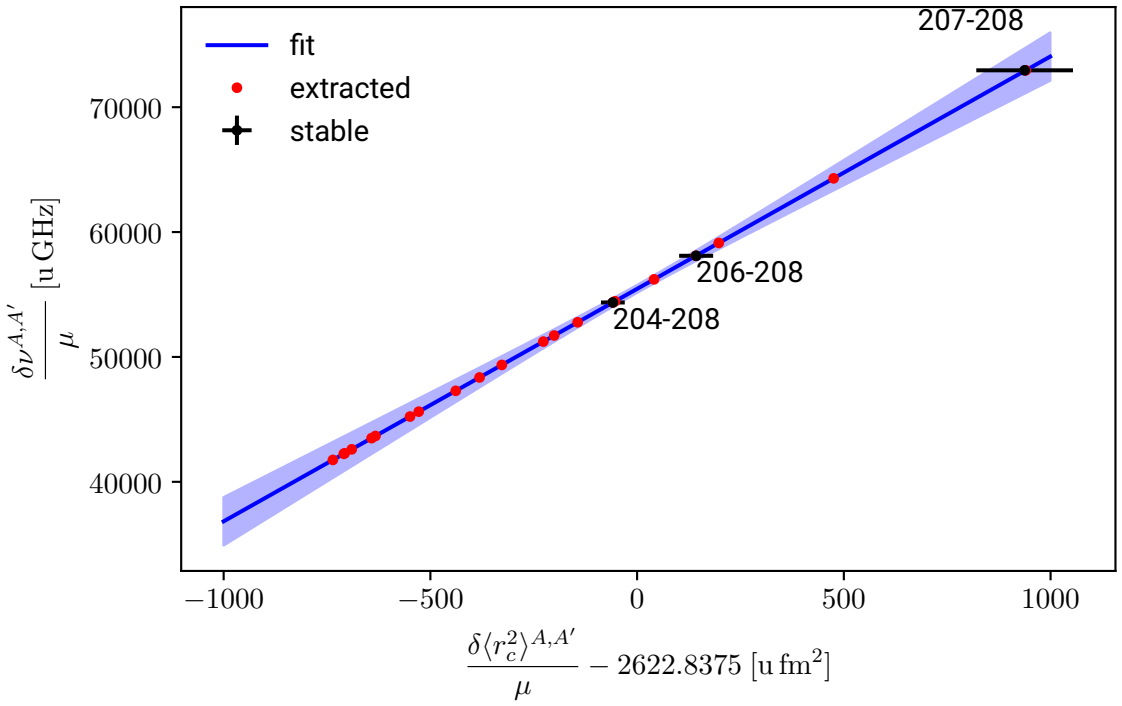

Figure 6.3: King plot for lead. The used reference values of stable isotopes are marked in black. A linear function is fitted to the data. Red data points illustrate the extraction of the differential ms nuclear charge radii from the measured isotope shifts.

and isomers are presented in Tab. 6.5.

Table 6.5: Mean-square nuclear charge radii of ground state nuclei $\delta\langle r_c^2\rangle^{A,208}$ and isomers $\delta\langle r_c^2\rangle^{A^m,208}$ relative to ^{208}Pb and isomer shifts $\delta\langle r_c^2\rangle^{m,g}$. The statistical uncertainties are given in parentheses and the systematic uncertainties from the King-plot procedure in brackets.

Isotope	$\delta\langle r_c^2\rangle^{A,208}$ [fm^2]	$\delta\langle r_c^2\rangle^{A^m,208}$ [fm^2]	$\delta\langle r_c^2\rangle^{m,g}$ [fm^2]
187	$-1.03278(22)[4003]$	$-1.07191(29)[3615]$	$-0,03916(20)[400]$
188	$-0.96507(18)[3926]$		
189	$-0.93398(9)[3491]$	$-0.96612(13)[3173]$	$-0,03218(9)[323]$
190	$-0.87240(14)[3337]$		
191	$-0.85159(11)[2848]$	$-0.87338(14)[2634]$	$-0,02180(9)[223]$
192	$-0.79378(13)[2704]$		
193	$-0.78285(9)[2103]$	$-0.79003(13)[2033]$	$-0,00718(9)[73]$
194	$-0.71969(11)[2025]$		
195	$-0.71875(7)[1352]$	$-0.70690(9)[1464]$	$0.01187(6)[121]$
196	$-0.64324(9)[1402]$		
197	$-0.65053(8)[703]$	$-0.61266(10)[1034]$	$0.03791(6)[387]$
198	$-0.55777(4)[903]$		
199	$-0.55904(5)[372]$	$-0.50621(7)[747]$	$0.05288(5)[540]$
200	$-0.46114(13)[545]$		
201	$-0.44632(5)[279]$	$-0.38936(7)[580]$	$0.05702(5)[582]$
202	$-0.35435(13)[313]$	$-0.35699(15)[296]$	$-0.00265(8)[27]$
203	$-0.33426(7)[305]$	$-0.26766(11)[481]$	$0.06665(9)[681]$
204	$-0.24199(13)[163]$		
205	$-0.21817(20)[358]$		
206	$-0.12923(6)[101]$		
207	$-0.08283(3)[225]$		

The field-shift factor and isomeric shifts can also be utilized to compute the isomeric differential ms charge radii relative to the ground state by

$$\delta\langle r^2\rangle^{m,g} = \frac{\delta\nu^{m,g}}{F}. \tag{6.4}$$

Their values are also included in Tab. 6.5. It is important to note that selecting the correct V_2 ratios from the literature is crucial. A King plot performed with V_2 ratios averaged from various available literature values yielded a field-shift factor of (20.4 ± 2.3) GHz/fm^2 and a mass-shift factor of (1605 ± 6025) GHz u. However, the extraction of the nuclear charge radii turned out to be largely tolerant to these variations and the extracted $\delta\langle r_c^2\rangle^{A,208}$ in both attempts agreed within their uncertainties.

For a cross-verification with isotope shifts measured in other transitions (summarized in

[121]), multidimensional linear fits for different sets of transitions were conducted. These fits encompass the ratio of field shifts between different transitions i and j by

$$\widetilde{\delta\nu_i} = \frac{F_i}{F_j}\widetilde{\delta\nu_j} + \left(K_i - \frac{F_i}{Fj}K_j\right). \tag{6.5}$$

The resulting field shifts of the 723 nm transition investigated in this work, were in the range of $18.8 - 18.9\,\mathrm{GHz/fm^2}$ with an uncertainty of $2\,\mathrm{GHz/fm^2}$, demonstrating excellent agreement with the previous results. Likewise, the mass shifts, varying between $5890 - 6243\,\mathrm{GHz\,u} \pm 5200\,\mathrm{GHz\,u}$, corroborate the King plot results derived solely from the data of this work.

6.2 Discussion

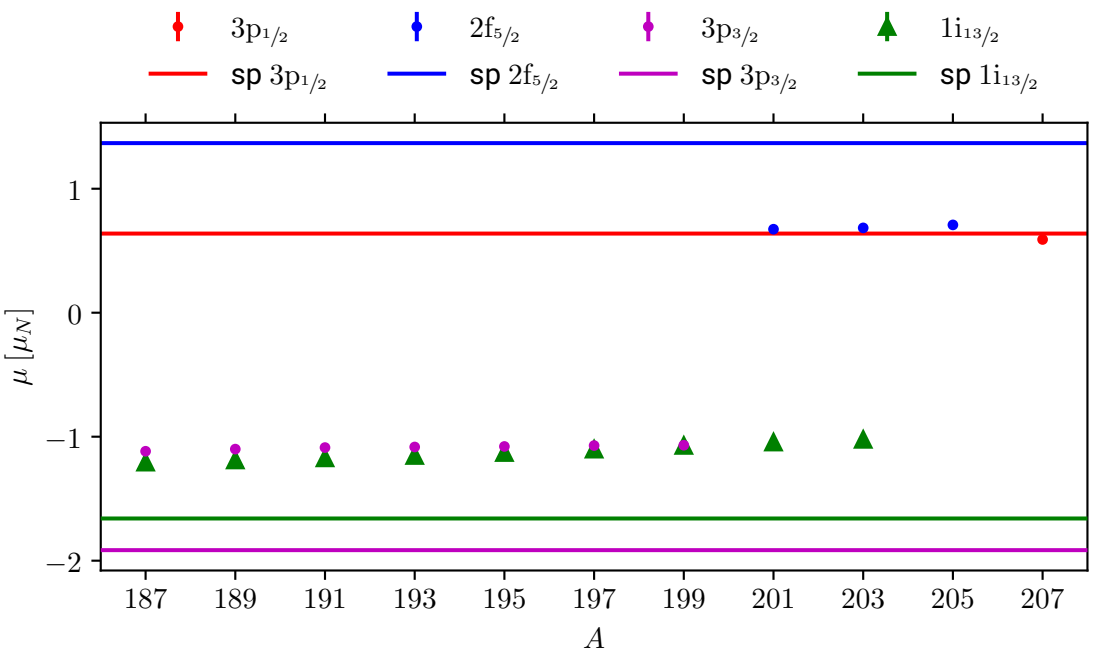

Figure 6.4: Magnetic dipole moments of ground states and isomeric states of lead. The horizontal lines show the single-particle magnetic moments, or Schmidt lines, for the different spin configurations without any quenching.

The magnetic dipole moments of the lead ground states and isomeric states are plotted in Fig. 6.4 alongside the Schmidt lines. For the ground states ($p_{3/2}$, $f_{5/2}$, $p_{1/2}$), from ^{199}Pb to ^{201}Pb,

a jump in the magnetic dipole moment is observed, coinciding with the observed change in the nuclear spin from $I = 3/2$ to $I = 5/2$. Approaching the neutron-shell closure, from $N = 118$ up to higher neutron numbers, neutrons populate the $2f_{5/2}$ level until $N = 124$, after which neutrons start filling the $3p_{1/2}$ level. For this change of nuclear spin, a much smaller jump is observed and the experimental nuclear magnetic dipole moment of ^{207}Pb agrees well with the single-particle Schmidt value.

For the isomeric $i_{13/2}$ states, a nearly constant trend in the nuclear magnetic dipole moments extends along all investigated odd isotopes from $N = 105$ up to $N = 121$, even though the $1i_{13/2}$ level has only a capacity for 12 neutrons. The deviation from the expected Schmidt values is slightly smaller for the isomeric states compared to the $3p_{3/2}$ and $2f_{5/2}$ ground states. This smaller deviation can be attributed to the unique-parity character of the intruder $1i_{13/2}$ level, which constrains the unpaired neutron to this level. As the other levels within this neutron shell have the same parity, their states are expected to mix into the many-body wave function of the entire nucleus, resulting in larger deviations of the experimental magnetic dipole moments from the single-particle Schmidt values.

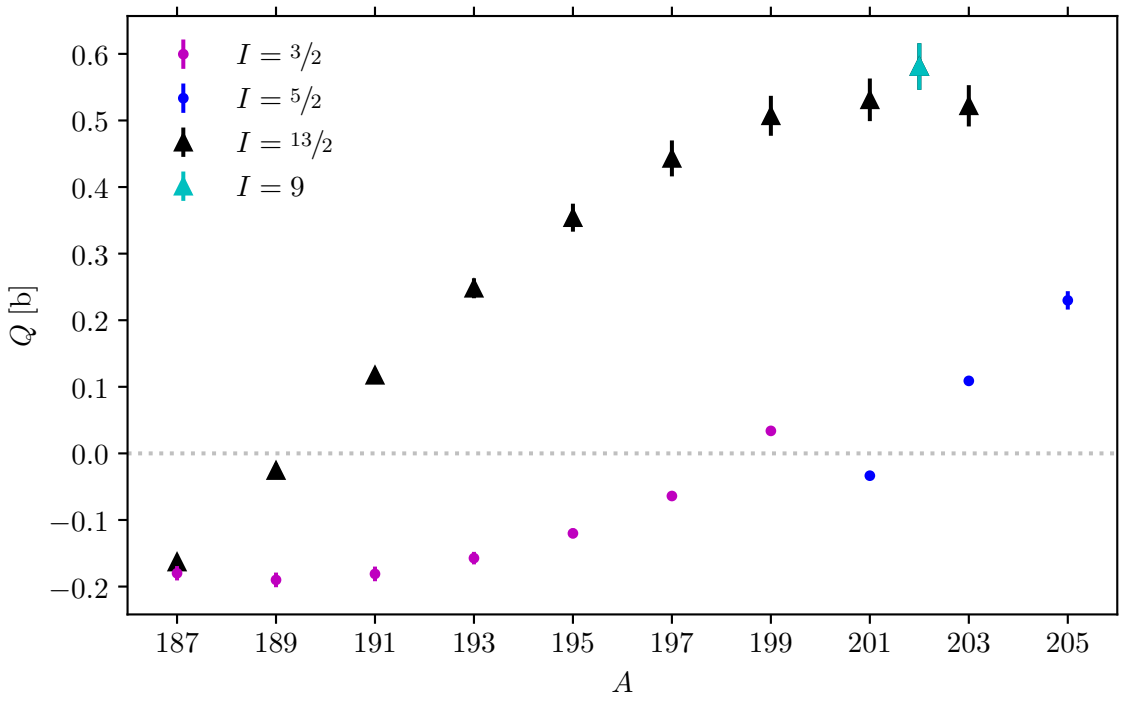

Figure 6.5: Electric quadrupole moments of lead isotopes (•) and isomers (▲). The different colors refer to the different nuclear spins. With the spin change in the ground states, a sign flip in the quadrupole moment is observed.

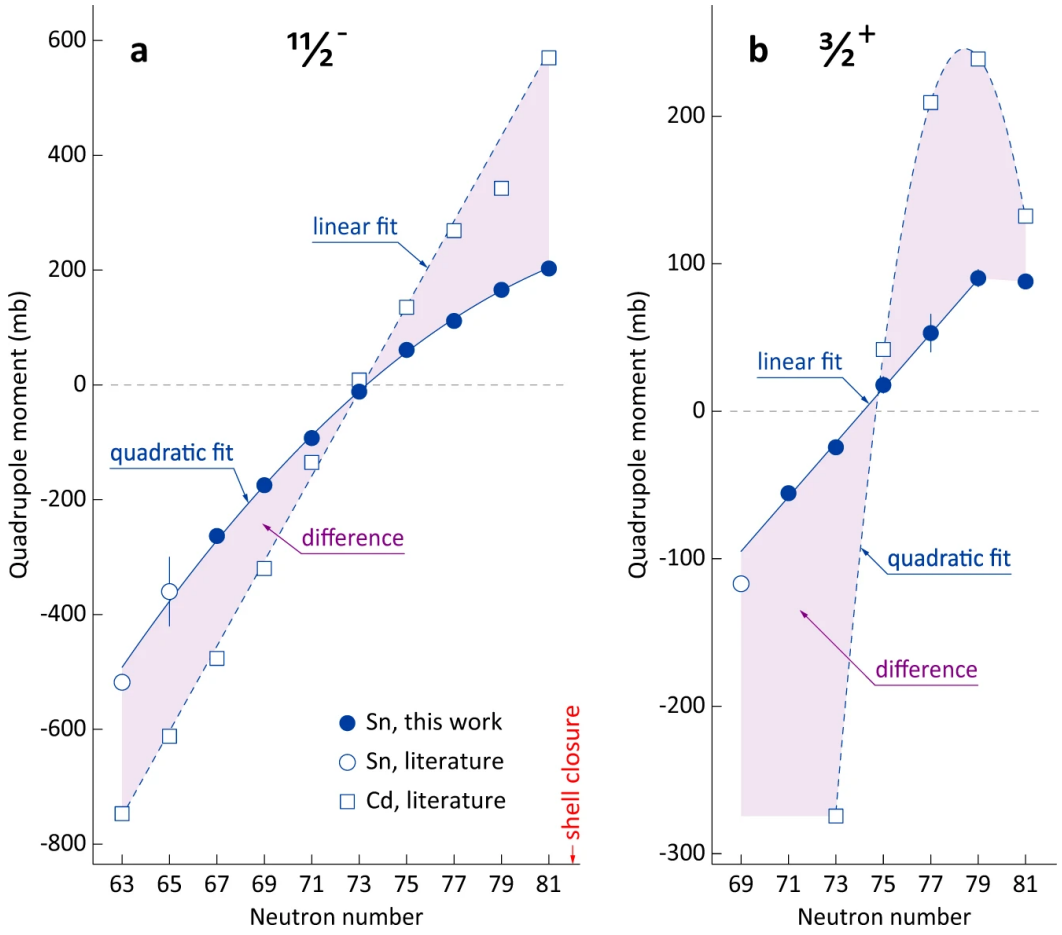

Figure 6.6: Isomeric ($I = {}^{11}/_{2}$) and ground state ($I = {}^{3}/_{2}$) quadrupole moments of Sn and Cd below the neutron shell closure at $N = 82$. Figure taken from [27]. Used under CC by 4.0, cropped from original.

The quadrupole moments of the ${}^{3}/_{2}^{-}$ ground states show a quadratic trend with a wide minimum around ^{189}Pb. From ^{199}Pb to ^{201}Pb, the spin of the ground state changes to ${}^{5}/_{2}$ and a switch of the sign of the quadrupole moment is observed as it is expected in the single-particle shell model, when the filing of a new (sub-) shell starts as discussed in the theory chapter. The three obtained quadrupole moments of the ${}^{5}/_{2}^{-}$ states rise linearly and already ^{203}Pb has a positive quadrupole moment. The sign flip can be interpreted in the way that the quadrupole moment of ^{199}Pb is defined by an unpaired hole while the quadrupole moment of ^{201}Pb is defined by an unpaired particle.

The quadrupole moments of the ${}^{13}/_{2}^{+}$ isomeric states in Fig. 6.5 exhibit a somehow quadratic trend, crossing zero at $N = 108$, but could also be interpreted as a linear increase from ^{187}Pb to ^{193}Pb, which then softly flattens out. The quadrupole moments of the ${}^{3}/_{2}^{+}$ states in Sn

were observed to exhibit also a linear increase along five isotopes but then abruptly stayed constant. This is visible in Fig. 6.6 taken from [27]. In comparison to the trend in quadrupole moments of the magic tin isotopes below the neutron shell closure, both, the slopes of the trends of the ground-state and isomeric-state quadrupole moments are intensified in lead by approximately a factor of two. While the general trend of the ground state moments differs significantly between lead and tin, the quadrupole moments of the isomeric states show at least some similarities.

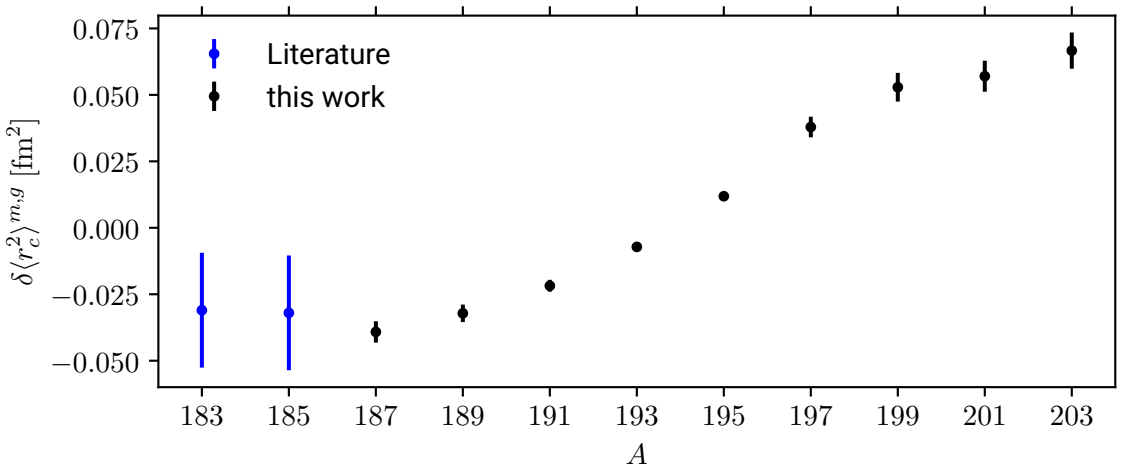

Figure 6.7: Isomer shifts in lead isotopes. Black values are derived from measurements performed within this work while blue values are taken from [93].

The isomer shift of the nuclear charge radius, i.e. its change between the ground state and the isomeric state is plotted in Fig. 6.7. Up to ^{193}Pb, where the quadrupole moment of the $^{13}/_{2}^{+}$ isomers increases linearly (see Fig. 6.5), the isomer shift follows a flat, parabolic trend. When the trend in the quadrupole moment starts flattening, the isomer shift increases only linearly from ^{195}Pb up to ^{199}Pb. For ^{201}Pb and ^{203}Pb, where the change in the ground-state spins occurs, the slope in the isomer shift changes again. Although the parabolic trends observed in the isomer shifts of magic tin [27] and cadmium isotopes [28] are absent in lead, slight resemblances can be noted. While in cadmium, the quadratic behavior was linked to the linear trend in the isomeric quadrupole moments (see Ch. 1 and [28]), such a linear trend is absent in tin and even less prominent in the lead isomers. It would be interesting to extend the investigations to other isotopic chains with unique-parity isomers.

Figure 6.8 illustrates and summarizes the differential ms nuclear charge radii of ground state nuclei and isomers. The experimental values are compared to EDF calucaltions using a Fayans functional extended by isovector pairing terms (IVP) (see [122] for details) and to

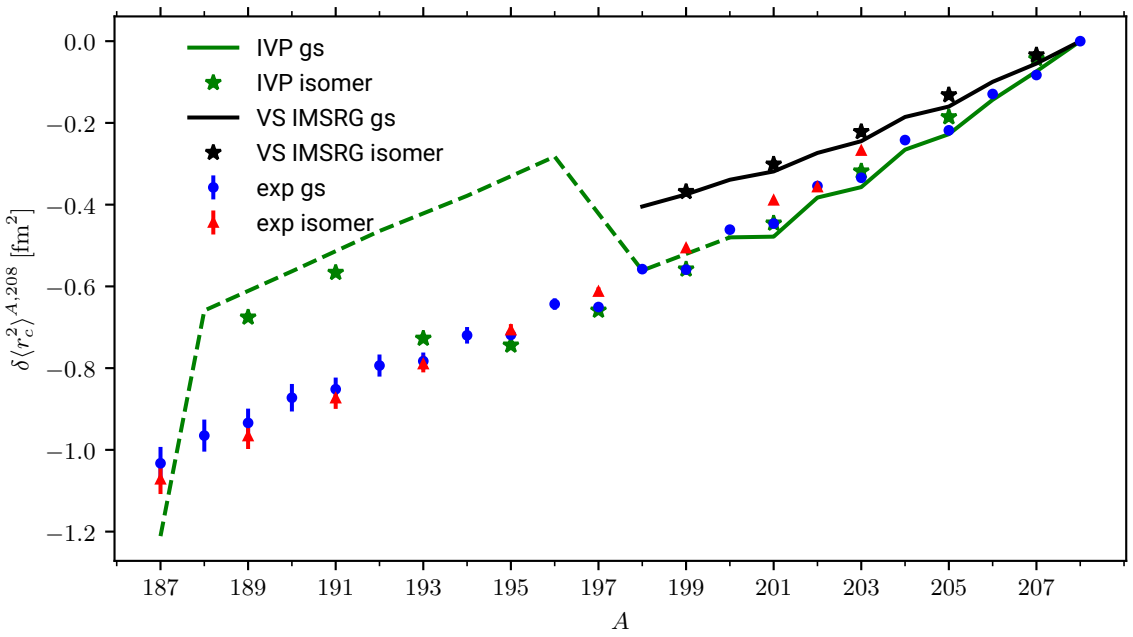

Figure 6.8: Differential ms nuclear charge radii of lead. Experimental values of the ground state nuclei are marked with blue circles and of the isomeric states with red triangles. Values for ground states (gs) derived from Fayans calculations (IVP) [P.-G. Reinhard, L.V. Rodríguez, private communication] are presented by a green line and the isomeric states are marked as green stars. For the mass region with the dashed line, only values for the even isotopes have been calculated. Values derived from ab initio calculations (VS IMSRG) [T. Miyagi, L.V. Rodríguez, private communication] are presented in black, with the isomeric states marked as stars.

ab initio valence-space in-medium similarity renormalization group (VS IMSRG) calculations. From the neutron shell closure $N = 126$ down to $N = 116$, the EDF calculations show an overall better agreement with the experimental data compared to the ab initio calculations. However, for lower neutron numbers, the EDF calculations also fail to accurately describe the differential ms nuclear charge radii.

With the definition of the staggering parameter

$$\mathrm{OES}_A = \frac{\delta\langle r^2\rangle^{A,108} - \delta\langle r^2\rangle^{A-1,108}}{1/2\left(\delta\langle r^2\rangle^{A+1,108} - \delta\langle r^2\rangle^{A-1,108}\right)} \tag{6.6}$$

the pattern of odd-even staggering can be investigated and visualized in detail. For odd isotopes normal OES would imply an OES parameter < 1, for even isotopes it implies an OES parameter > 1.

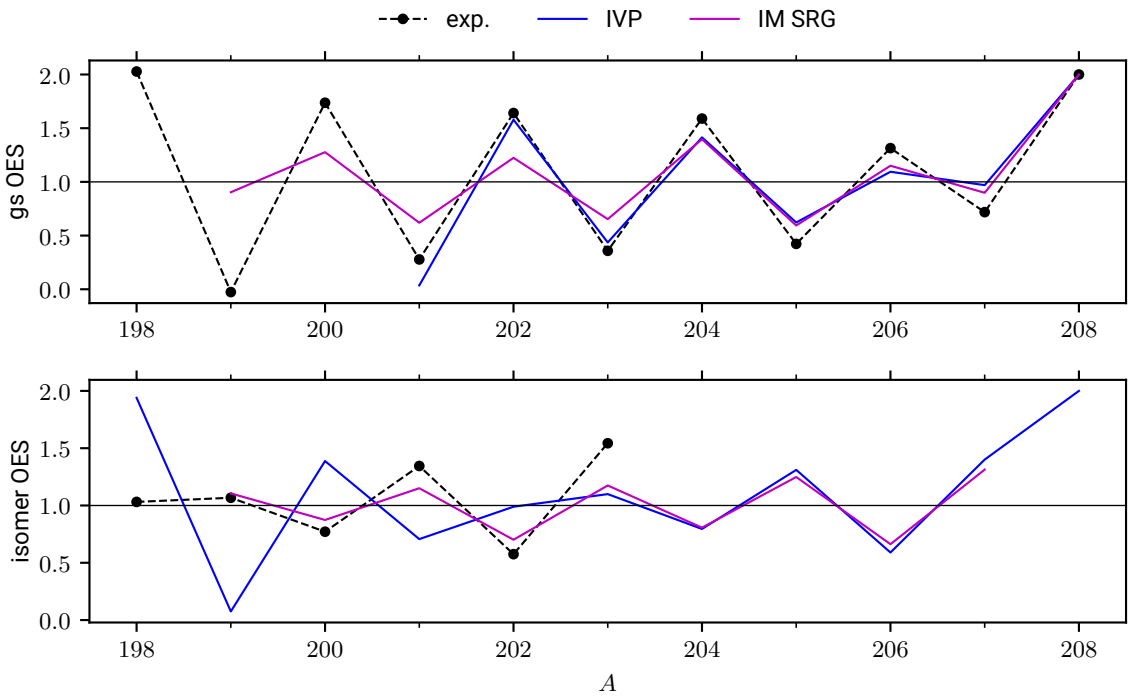

Figure 6.9: Experimental odd-even staggering (OES) in lead ground states (gs) and isomeric states in comparison to EDF (IVP) [P.-G. Reinhard, L.V. Rodríguez, private communication] and ab initio (VS IMSRG) calculations [T. Miyagi, L.V. Rodríguez, private communication]. Both theoretical calculations can describe the ground state OES observed experimentally. The isomeric OES is better described by the ab initio calculations, while the Fayans calculations predict inverse OES.

The OES of lead is compared to theoretical calculations in Fig. 6.9. In the ground states, the OES is well described by the Fayans and the ab initio calculations. The good agreement with the Fayans calculations is remarkable, as the OES is supposed to be related to small-scale effects. It is, therefore, not surprising, that the isomeric OES is only well described by the ab initio calculations, while the Fayans EDF calculations predict an inverted OES compared to the experimental values.

7 Palladium

This chapter covers the detailed analysis of the palladium data and concludes with a discussion of the new results acquired in the palladium isotopic chain. The isotope shifts and hyperfine parameters extracted from the data sets are presented and the differential nuclear charge radii and the nuclear moments are extracted.

7.1 Data Analysis

7.1.1 Data set

The measurements of palladium were the very first online-experiment conducted at ATLANTIS. Consequently, this experiment also served as the online commissioning run for the new setup.

Beamtime 1 - Hyperfine Spectra

In a first beamtime, CLS on all stable Pd isotopes as well as the neutron-rich $^{112-116,118}$Pd isotopes and, potentially, isomeric states was performed. The stable isotopes were produced by the offline ion source. Since the performance of the offline source varied over time, owing to the ablation process changing the target surface, different ablation laser powers were used during the beamtime. The data analysis of this beamtime exhibited a strong dependency of the resonance width and position on the ablation laser power (see. Sec. 4.3.5). In addition, the stabilization of the RFQCB high-voltage platform broke during the beamtime and a constant logging of the high-voltage and wavemeter readout was not implemented yet. Therefore, the data of this first beamtime was not used to determine the isotope shifts but only to extract the hyperfine parameters A and B of the odd isotopes. The hyperfine spectra of the ground states of ^{113}Pd and ^{115}Pd were recorded, while the isomeric states and other odd isotopes could not be ovserved with the given rate and sensitivity. During this beamtime the RFQCB potential and laser frequency were read out and stored once for each run. In Tab. 7.1 for each odd isotope the measurement times and number of scans performed, as well as the number of accumulated CARIBU bunches for one filling of the ATLANTIS-RFQCB are listed.

Table 7.1: For each odd isotope measured during the first and second beamtime, the total number of scans and of accumulated bunches in the RFQCB, and the total times spend on the measurement are listed. The number of scans and measurement time is always referring to the smallest observed hyperfine peak.

beamtime	isotope	scans	Accumulation	time [h : min : s]
1	^{105}Pd	200	1	00 : 17 : 09
	^{113}Pd	210	100	10 : 22 : 60
	^{115}Pd	67	500	3 : 21 : 51
2	^{112}Pd	25	500	6 : 41 : 54
	^{113}Pd	83	500	18 : 29 : 57
	^{114}Pd	63	500	8 : 33 : 17
	^{115}Pd	40	250	5 : 12 : 20
	^{116}Pd	16	200	1 : 51 : 30
	^{118}Pd	790	69	18 : 18 : 24

Beamtime 2 - Isotope Shifts

In a second beamtime, the isotope shifts were measured. During this beamtime, the high-voltage of the RFQCB platform and laser frequency were continuously recorded with time-stamps. This allowed a more accurate treatment of the main acceleration voltage and laser frequency for each run and also to check for irregularities that would compromise the isotope-shift measurements. Since the hyperfine structure of the neutron-rich odd isotopes ^{113}Pd and ^{115}Pd is known from the first run, only the two largest hyperfine peaks were scanned and the isotope shift was determined based on the known hyperfine structure. The same information as for beamtime 1 is included in Tab. 7.1.

Beamtime 3 - King Plot

The third beamtime was performed for a precise investigation of the isotope shifts in stable Pd. Each run consists of two isotopes, each measured in a separate track. The scan alternated between the two tracks, cancelling any temporal drifts in the high voltage or in the laser frequency. Since both isotopes were measured with the same laser set frequency, the wavemeter uncertainty is eliminated and the remaining uncertainty is mostly the uncertainty originating from the high-voltage amplifier used for the Doppler-tuning voltage. The RFQCB voltage and laser frequency were again recorded continuously during a measurement. In total the following isotope pairs were investigated: ^{102}Pd $-$ ^{104}Pd, ^{104}Pd $-$ ^{105}Pd, ^{104}Pd $-$ ^{106}Pd, ^{106}Pd $-$ ^{108}Pd, ^{108}Pd $-$ ^{110}Pd. These isotope shifts were used to perform the King Plot analysis, described in Sec. 7.1.10 to extract the atomic isotope-shift parameters.

7.1.2 Line Shape

The line shape of the spectra is assumed to be a Voigt profile. With the spontaneous transition probability A_i tabulated in [123], the natural linewidth for the used transition is

$$\Delta\nu_{\text{nat}} = \frac{A_i}{2\pi} = 19.8\,\text{MHz}. \tag{7.1}$$

The power broadening effects can be estimated from the saturation intensity [76]

$$I_{\text{sat}} = \frac{\pi hc}{3\lambda^3\tau} \tag{7.2}$$

by

$$\Delta\nu_{\text{sat}} = \Delta\nu_{\text{nat}}\sqrt{1 + \frac{I_{\text{L}}}{I_{\text{sat}}}}. \tag{7.3}$$

For the observed transitions and the applied laser power of about $300\,\mu\text{W}$ and a beam diameter of $1\,\text{mm}$ this results in a saturation broadening factor of 1.085 such that the power-broadened Lorentzian linewidth is $\Delta\nu_{\text{L}} = 21.5\,\text{MHz}$. Since the powers used in the experiment were generally not higher than that, the effect of power broadening cannot be distinguished in the convoluted Voigt profile.

According to [112], the beam extracted from the ATLANTIS-RFQCB has an energy FWHM of typically $\Delta U = 5\,\text{eV}$. With [124]

$$\Delta\nu_{\text{Dopp}} = \nu_0\frac{\Delta v}{c} = \nu_0\sqrt{\frac{eU}{2mc^2}}\frac{\Delta U}{U} \tag{7.4}$$

this leads to a reduced Doppler broadening of $\Delta\nu_{\text{Dopp}} = 60\,\text{MHz} = \Delta\nu_G$. The total FWHM of the expected Voigt profile can then be estimated by [125]

$$\Delta\nu_{\text{V}} \approx \frac{1}{2}\left(1.0692\gamma + \sqrt{0.86639\gamma^2 + 4\Delta\nu_{\text{G}}^2}\right) = 71.8\,\text{MHz} \tag{7.5}$$

with the Lorentzian FWHM γ and the Gaussian FWHM $\Delta\nu_{\text{G}} = 2\sqrt{2\ln 2}\sigma$. In contrast to the analysis of the COLLAPS data, the Lorentzian linewidth was assumed be constant, as all measurements were performed with the same laser power. In a first step all reference runs (^{108}Pd), used to determine isotope shifts, were fitted simultaneously with a shared Lorentzian width γ. This procedure results in $\gamma = (45.7 \pm 1.2)\,\text{MHz}$, with the uncertainty coming from the fit. For the final fitting of all spectra, γ was fixed to this value. The resulting weighted average of the Gaussian standard deviation of all reference runs is $\sigma = 13.1\,\text{MHz}$ with a standard deviation of $4.4\,\text{MHz}$ (see Fig. 7.1). This is smaller by a factor of 4.6 than the expected Doppler

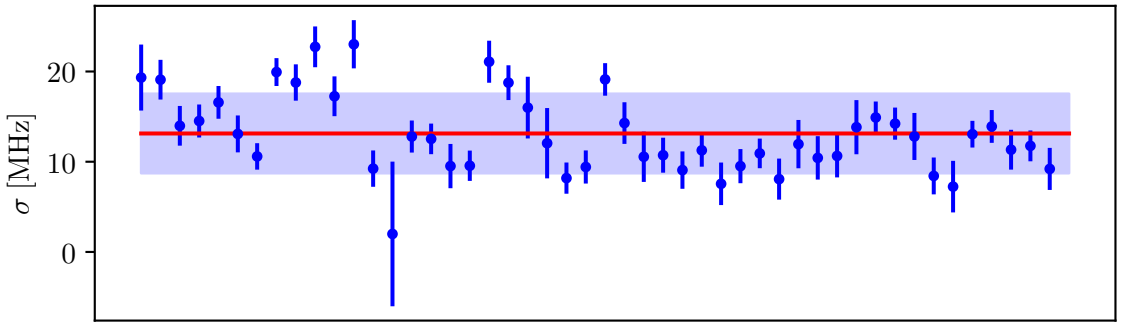

Figure 7.1: The Gaussian width σ for all reference runs on ^{108}Pd used to extract isotope shifts for a fixed Lorentzian linewidth of $45.7\,\mathrm{MHz}$. It varies around the weighted average of $13.1\,\mathrm{MHz}$ (red line) with a standard deviation of $4.4\,\mathrm{MHz}$ (blue shaded area).

broadening while the Lorentzian width γ is larger by a factor of 2 than expected. The resulting FWHM of the Voigt profile is $62\,\mathrm{MHz}$, which is slightly smaller than the expected width. This hints to a better cooling performance of the RFQCB with energy FWHM of $\sim 3-4\,\mathrm{eV}$. The robustness of the extracted center position of a resonance is illustrated in Fig. 7.2, where the center position is plotted against different fixed values of γ for one of the reference runs. The small influence on the center position can be neglected compared to the fit uncertainties and would additionally cancel in the calculation of the isotope shifts.

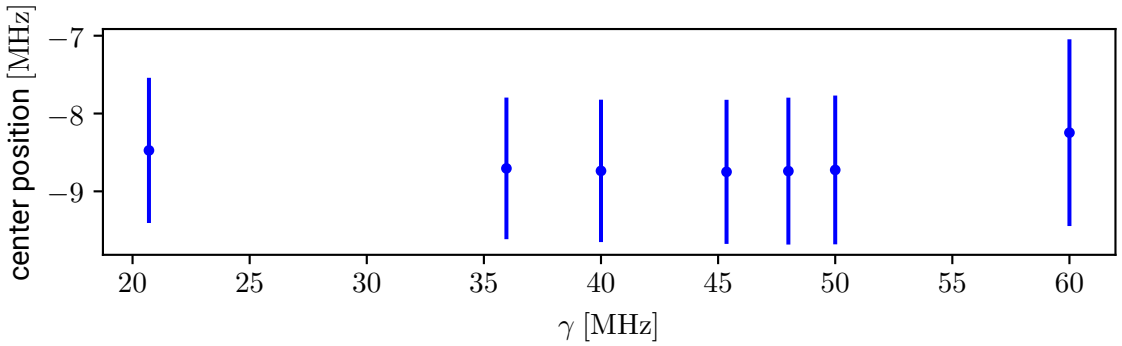

Figure 7.2: The center position of a single reference run on ^{108}Pd for different fixed values of the Lorentzian linewidth γ. The plotted error bars are the statistical uncertainties from the fit.

7.1.3 Time Gates

To choose a time gate, a Gaussian profile was fitted to the time projections of all analyzed runs. Figure 7.3 shows an example for ^{106}Pd. The upper two plots refer to the first two PMTs located in the first, while the lower two plots show the data from the other two PMTs located in the second detection region. Due to the different positions along the beamline, the time-of-flight to the second detection region is slightly longer. The plot also shows that the background signal in the second detection region is about three times lower than in the first one, providing a better signal-to-noise ratio.

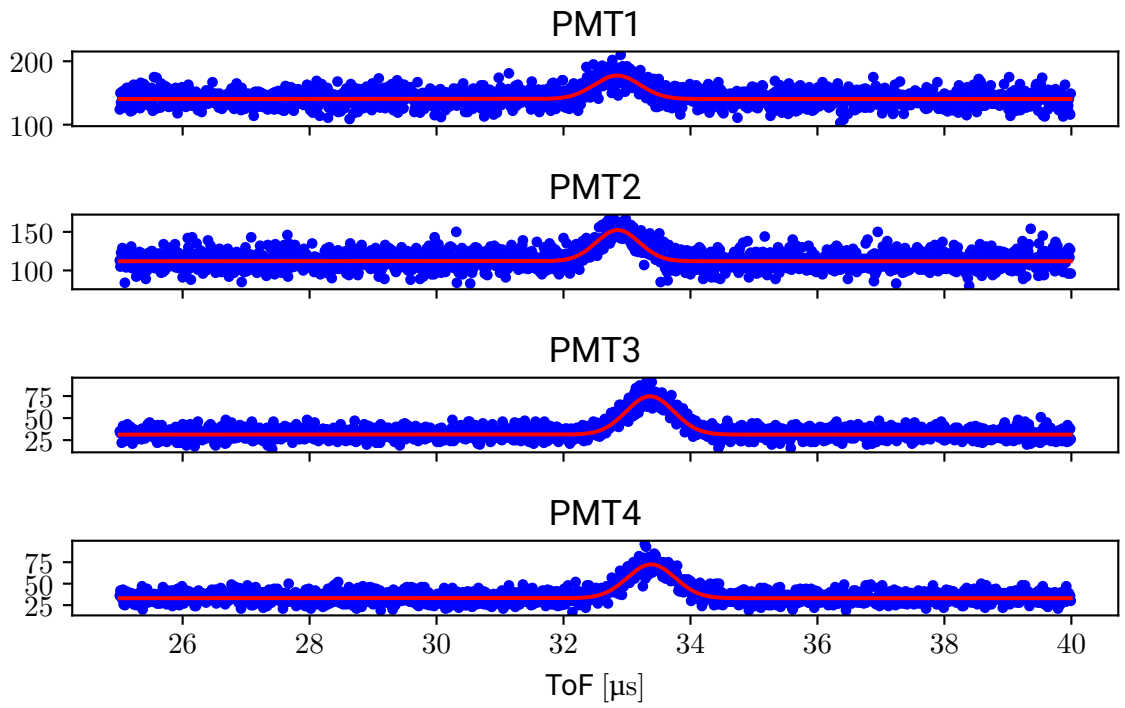

Figure 7.3: Time projection of an example measurement on ^{106}Pd for each PMT. To each time projection a Gaussian profile was fitted to determine the time-of-flight and the bunch width in time. A small shift of the mid time-of-flight can be seen between the upper two PMTs (first detection region) and the lower two PMTs (second detection region). The statistics in the second detection region are better than in the first detection region.

After fitting the time projections for each run, the average time-of-flight and average width of the Gaussian profile were calculated for each isotope and each detection region and plotted against the mass number. The spectra of ^{102,113}Pd and ^{118}Pd have too low statistics for fitting in the ToF projection, and have been excluded from this analysis. For each detection region,

the two PMTs were evaluated together. As Fig. 7.4 shows, a linear function can be fitted to the calculated ToF.

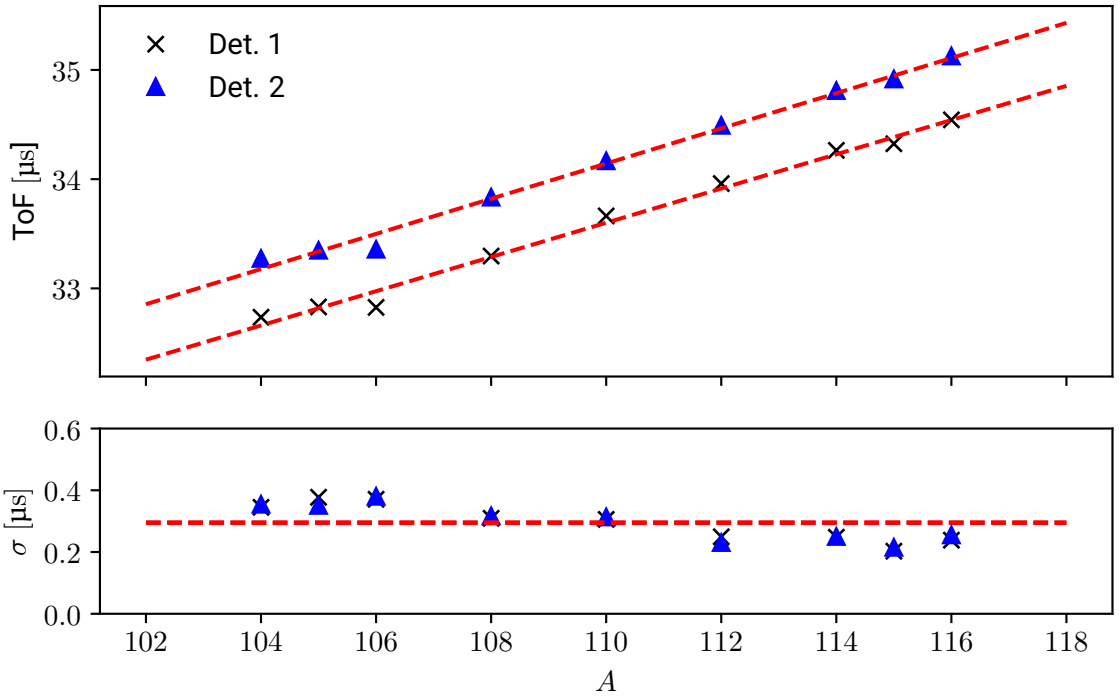

Figure 7.4: The time-of-flight (ToF) from the RFQCB to the detection region for each isotope as a function of its mass number. Upper frame. ToF determined from the spectra measured by the two PMTs in the first (▲) and second (×) detection region with a corresponding linear fit. Lower frame: Fitted temporal Gaussian widths of the ion bunch as a function of its mass number. ToF spectra, from which the time-of-flight could not be extracted due to a lack of statistics, were excluded from this analysis (^{102,113,118}Pd).

From the non-relativistic kinetic energy

$$E_{\text{kin}} = \frac{1}{2}mv^2 = \frac{1}{2}m\frac{s^2}{t^2} \tag{7.6}$$

with the mass m, the velocity v, the traveled distance s and the time-of-flight t, one expects a square root dependency of the time-of-flight from the atom's mass:

$$t = \sqrt{\frac{s}{2E_{\text{kin}}}}\sqrt{m} \tag{7.7}$$

With a first order Taylor expansion of

$$\sqrt{1-u} \approx 1 + \frac{1}{2}u + \mathcal{O}(u^2) \tag{7.8}$$

and

$$\sqrt{m} = \sqrt{m_0}\sqrt{1 - \frac{m_0 - m}{m_0}}, \tag{7.9}$$

where $m = m_0 + \delta m$, in first order the time-of-flight depends linearly on the atom's mass for $m \approx m_0$:

$$t \approx \sqrt{\frac{s^2 m_0}{8Ue}} + \sqrt{\frac{s^2}{8Uem_0}}m \tag{7.10}$$

To set an unbiased time-gate for each isotope in the further analysis, the linear fit function is used to choose a consistent ToF and time-gate width. The fit function

$t = 16.364\,\mu\text{s} + 0.1567\,\mu\text{s}A$

is used for the PMTs in the first detection region, and

$t = 16.433\,\mu\text{s} + 0.1610\,\mu\text{s}A$

for the PMTs in the second detection region. The resulting ToFs are shown in Tab. 7.2. The time-gate width for the evaluation is chosen as a 2σ from the Gaussian fit. It is chosen equally for both detection regions, as the bunch width is identical in the two detection regions, as observed in Fig. 7.4. For all PMTs and for all isotopes a time-gate width of $1.2\,\mu\text{s}$ is therefore used.

Table 7.2: Chosen time-gate centers in µs for the investigated Pd isotopes. The time-gate centers are determined from the linear fit shown in Fig. 7.4. For the first (DR 1) and second (DR 2) detection region different times are used, since their location along the beamline leads to different times of flight.

isotope	DR 1 [µs]	DR 2 [µs]
^{102}Pd	32.35	32.86
^{104}Pd	32.66	33.18
^{105}Pd	32.82	33.34
^{106}Pd	32.97	33.50
^{108}Pd	33.29	33.82
^{110}Pd	33.60	34.14
^{112}Pd	33.91	34.47
^{113}Pd	34.07	34.63
^{114}Pd	34.23	34.79
^{115}Pd	34.38	34.95
^{116}Pd	34.54	35.11
^{118}Pd	34.85	35.43

Figure 7.1.3 shows an example of the robustness of the results with respect to the chosen time gates. The center position of a single run of a ^{106}Pd and a ^{108}Pd resonance as well as the resulting isotope shift are plotted as obtained from fits with different time-gate positions (left column) and with different time-gate widths (right column). Both, the time-gate position and the time-gate width lead to negligible changes in the center positions , at least within a range of $\sim 0.5\,\mu s$ which corresponds to approximately 1σ of the Gaussian ToF width. A small shift is observed for relative large variations of the time-gate center that is still within the statistical uncertainty but might lead to a systematic uncertainty. However, the tolerated range is much larger than the largest deviation of the ToF centers from the linear fit in Fig. 7.4 and a significant influence is not expected within this range of isotopes.

7.1.4 Beam Energy Calibration

The RFQCB potential was continuously monitored and the trapping potential applied to the trapping electrode of the RFQCB is added to determine the kinetic energy of the probed beam. Since a slightly higher potential is applied to the kicking and pulling electrodes of the RFQCB, it can be assumed, that the beam energy is slightly higher. To gauge this offset, a calibration measurement of the beam energy was performed. Such a calibration is based on the measurement of the absolute transition frequency as described in Sec. 4.2.3 and was performed on the reference isotope ^{108}Pd. It was assumed that the laser frequency was measured correctly within the uncertainties of the wavemeter, while the literature value of the transition frequency and the beam energy need to be calibrated. Note that a discrepancy from the literature value is most likely due to a wavemeter offset.

Before calibration, two different rest-frame frequencies are found for the collinear and anti-collinear measurement when using the multimeter and the wavemeter read-out. If only the voltage had an offset, the resonances would appear symmetrically shifted away from the absolute transition frequency. An additional offset of the wavemeter causes it to be centered around a different value. This is shown in Fig. 7.6.

In a first step, the wavemeter offset is compensated by shifting the literature transition frequency in the voltage-to-frequency transformation. For this, the difference of the resonance positions in voltage space $\Delta U = U_{\text{col}} - U_{\text{acol}}$ and the differential Doppler shift $\frac{\mathrm{d}\nu}{\mathrm{d}U}$ are calculated and used to correct the collinearly measured resonance frequency by $\Delta\nu = \Delta U \cdot \frac{\mathrm{d}\nu}{\mathrm{d}U}$. With this correction the absolute transition frequency for the used wavemeter can be calculated by $\nu_0 = \sqrt{(\nu_{\text{col}} - \Delta\nu) \cdot \nu_{\text{acol}}}$ and this value is from now on used for further transformations. The resonances now appear around $824\,574\,218.9\,\text{MHz}$ which is illustrated in the second row of Fig. 7.6. The resonances are not perfectly located symmetrically around $0\,\text{MHz}$ since the transformation from voltage to frequency space is only in first approximation linear and the

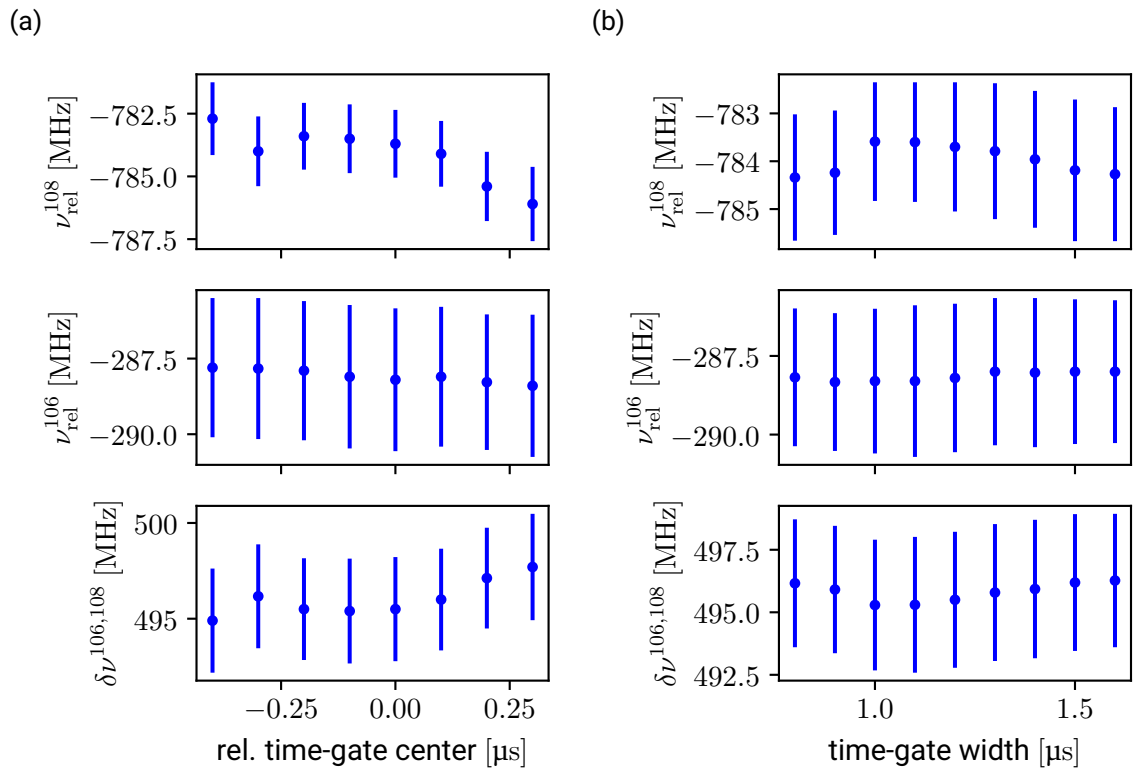

Figure 7.5: Influence of the chosen time gates on the center position of a resonance and on the isotope shift. (a) The relative center positions of ^{106}Pd and ^{108}Pd and the isotope shift are plotted over the chosen center of the time gate. The $0\,\mu s$ refers to the actual chosen time-gate position in the final analysis. The time-gate position has a small influence on the center position of the resonances, but the statistical uncertainties from the fit make this influence negligible for both, the center position of a single isotope and the isotope shift. (b) The relative center positions of ^{106}Pd and ^{108}Pd and the isotope shift are plotted over the chosen width of the time gate. The influence of the time-gate width is also negligible compared to the statistical uncertainties.

frequency correction with $\approx$200 MHz is rather large.

In a second step, the beam energy is calibrated. The calibration offset is added to the measured acceleration voltage, chosen such that the collinearly and anticollinearly measured resonances both appear at ≈ 0 MHz in Fig. 7.6. This correction can be calculated by

$$E_{\mathrm{kin,corr}} = \frac{mc^2}{2}\frac{(\nu_0 - \nu_{\mathrm{a/c}})^2}{\nu\nu_{\mathrm{a/c}}} = (3.5 \pm 0.5)\,\mathrm{V} \tag{7.11}$$

and leads to an offset in the beam energy from the measured acceleration voltage of $(3.5 \pm$

$0.5)$ V, which is also in agreement with similar calibration measurements performed at ATLANTIS on ^{102}Ru [B. Maaß, private communication].

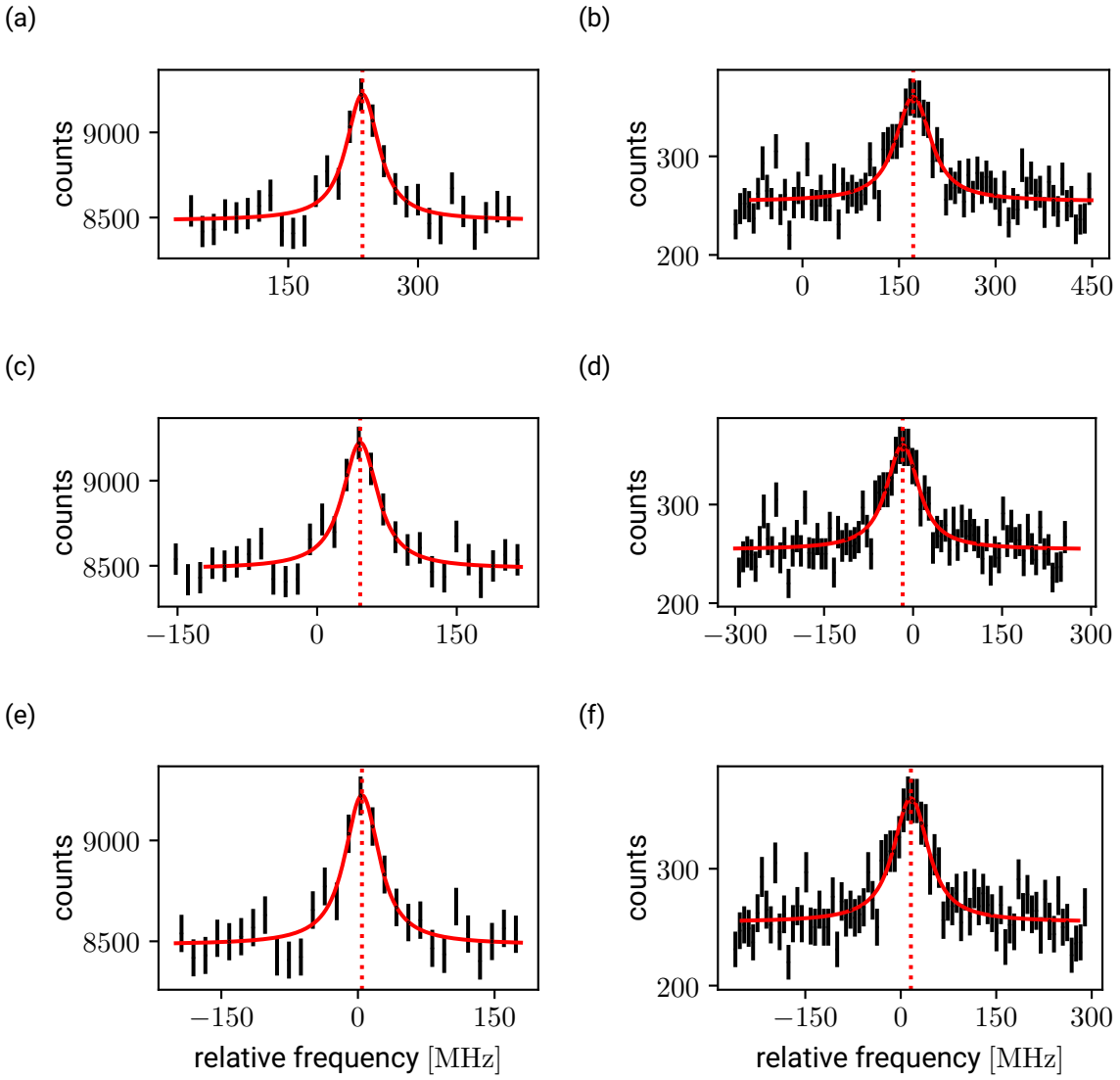

Figure 7.6: The resonance signal for a collinear (left) and anti-collinear (right) measurement of ^{108}Pd (a), (b) before calibration, (c), (d) after transition frequency calibration and (e), (f), after beam energy calibration. The x-axis shows the transition frequency with an offset. (a), (b): The offset is chosen such that $0\,\mathrm{MHz}$ refers to the literature transition frequency $824\,574\,029\,\mathrm{MHz}$ [90]. Owing to the uncertainties of the absolute transition frequency and the acceleration voltage, the resonances appear at different frequencies that are also not centered around 0. (c), (d): After handling the wavemeter offset (see text for more details), the x-axis offset is chosen such that $0\,\mathrm{MHz}$ refers to $824\,574\,219\,\mathrm{MHz}$. Due to the unknown beam energy the resonances appear at different frequencies but they are located, not perfectly, but much better than before, around zero. (e), (f): The x-axis offset is chosen such that $0\,\mathrm{MHz}$ refers to the calibrated frequency $824\,574\,219\,\mathrm{MHz}$. With the calibrated beam energy the resonances both appear at almost the same frequency close to $0\,\mathrm{MHz}$.

7.1.5 Fitting

The fitting of the spectra was performed in the frequency space. For this, the applied voltages had to be converted to frequencies in the atoms' rest frames.

Voltage to Frequency Conversion

The main acceleration voltage U_{acc} was continuously measured using a high-precision high-voltage divider, and a mean acceleration voltage U_{acc} is calculated for each run. This voltage was then corrected by the offset of $3.5\,\text{V}$ determined in Eq. (7.11).

For each run, the Kepco measurement performed before and the one performed after the CLS measurement are evaluated. Only the data points within the scanning region of the CLS measurement are fitted. From the two results, the amplification factor and offset are interpolated to the time, when the CLS measurement was performed, and used, to calculate the actual Doppler-tuning voltage. The conversion then follows the procedure described in Sec. 5.2.1.

Hyperfine Splitting

The hyperfine structure components of the odd isotopes ^{105,113,115}Pd measured in the first beamtime were fitted to determine the hyperfine parameters A and B. The ratios of the hyperfine parameters are determined in a first step by fitting the spectrum of the stable isotope ^{105}Pd. The ^{105}Pd run was fitted with A and B of the lower level fixed to the well known literature values $A = (-391.178 \pm 0.001)\,\text{MHz}$ [126] and $B = (-652.906 \pm 0.015)\,\text{MHz}$ [126] within their uncertainties. The ratios were used as free fitting parameters, resulting in ${}^{A_u}/_{A_l} = 0.2099 \pm 0.0005$ and ${}^{B_u}/_{B_l} = 0.4668 \pm 0.0031$. The hyperfine parameters of the upper level A_u and B_u are calculated from the literature values and the fitted ratios.

These ratios were then fixed for the two neutron-rich isotopes ^{113}Pd and ^{115}Pd.^{113}Pd was scanned six times, using different scan ranges and track settings, which cover most of the hyperfine peaks. All runs were fitted simultaneously with common hyperfine parameters ^{115}Pd was scanned in five runs, also using different scan ranges and track settings. All runs were fitted simultaneously with shared A_l. Since ^{115}Pd was assigned a spin $I = {}^1/_2$, it has no spectroscopic electric quadrupole moment and therefore the hyperfine parameter B is 0. Figure 7.7 shows example spectra for ^{113}Pd and ^{115}Pd.

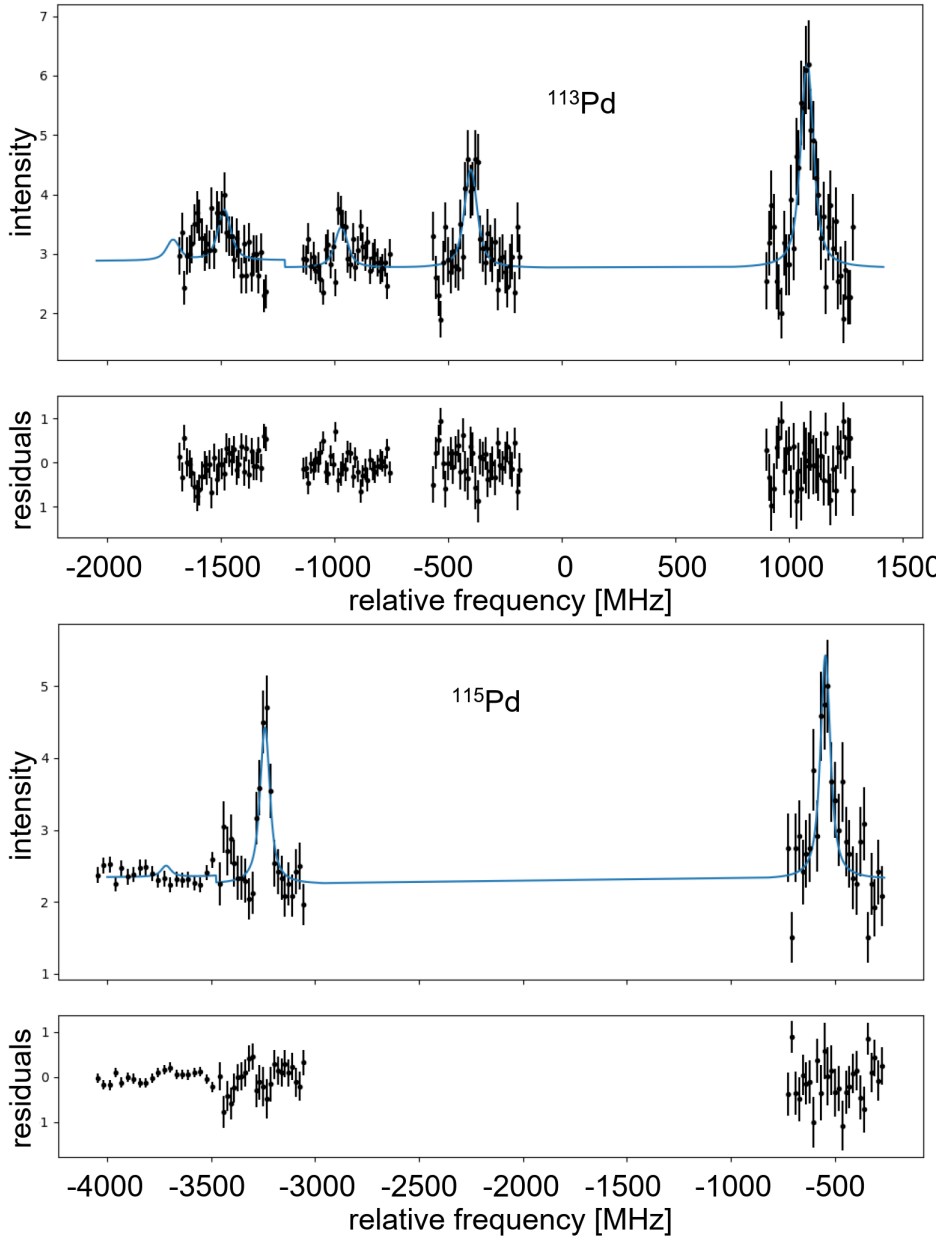

Figure 7.7: Example spectra of ^{113}Pd (upper frame) and ^{115}Pd (lower frame). The hyperfine peaks were recorded in separate tracks and with different number of scans. For this representation the measured counts are normalized to the number of scans. The frequency axis has an offset with $0\,\mathrm{MHz}$ representing the transition frequency of the reference isotope ^{108}Pd.

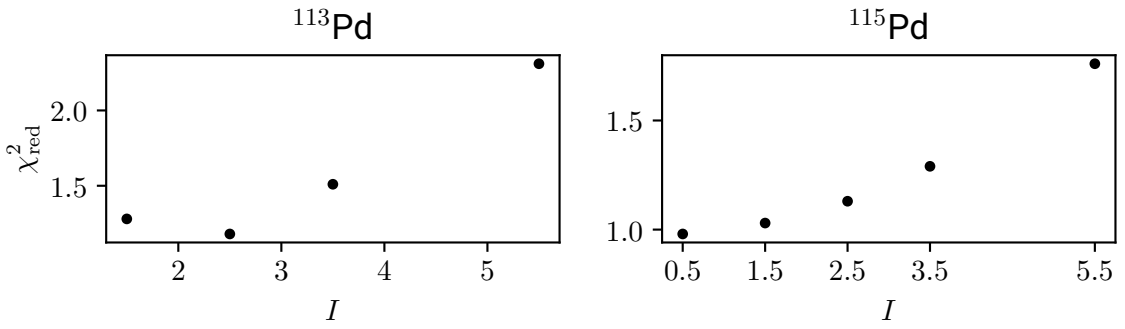

Figure 7.8: The reduced χ^2 of the fit is plotted over the assigned nuclear spin. For ^{113}Pd (top) a nuclear spin of $5/2$ results in the best reduced χ^2 while for ^{115}Pd (bottom) the reduced χ^2 analysis proposes a nuclear spin of $1/2$.

7.1.6 Spin Assignment

During the fit of the spectra, the nuclear spin is fixed. It therefore has to be either known, or, like for ^{113}Pd and ^{115}Pd, different possible nuclear spins have to be tested. According to the single-particle nuclear shell model [9], the odd neutron can occupy one of the following nuclear shells: $1g_{7/2}$, $2d_{5/2}$, $2p_{3/2}$, $3s_{1/2}$ or $1h_{11/2}$. In the single-particle picture, this allows nuclear spins of $^1/_2, ^3/_2, ^5/_2, ^7/_2$ and $^{11}/_2$. The National Nuclear Data Center lists the nuclear spins of ^{113}Pd and ^{115}Pd to be $^5/_2$ [51], but without definite assignment. Contrary, in the Evaluated Nuclear Structure Data File (ENSDF), the nuclear spin of ^{115}Pd is listed as $^1/_2$ [127], but also with uncertainty. The hyperfine spectra of the two neutron-rich odd isotopes can be used to determine the correct nuclear spin.

The data set of ^{113}Pd was fitted once for each possible spin ($^3/_2$ - $^7/_2$, $^{11}/_2$). The measured spectra showed five peaks, which is not compatible with a spin-$^1/_2$ structure that would result in only three peaks in the studied transition. The same was done for the data set of ^{115}Pd. In this case, only three peaks were observed which in principle is a clear signature for $I = ^1/_2$. However, to ensure that no unobserved peaks are possibly hidden in the noise due to a very small intensity or are outside the covered region, additional fits with the spins $^1/_2 - ^7/_2$ and $^{11}/_2$ were performed. The resulting reduced χ^2 of the fits are depicted in Fig. 7.8 and suggest assigning a nuclear spin of $^5/_2$ to ^{113}Pd and of $^1/_2$ to ^{115}Pd, given in Tab. 7.3.

This assignment is solidified by the resulting isotope shifts. Figure 7.9 shows the isotope shifts resulting from different spin assignments within the isotopic chain of palladium. Only the spin assignment of $^5/_2$ for ^{113}Pd and $^1/_2$ for ^{115}Pd lead to reasonable isotope shifts. Thus, these spins are finally determined in a model-independent way. The final fit results for the hyperfine parameters of the investigated odd Pd isotopes are listed in Tab. 7.3.

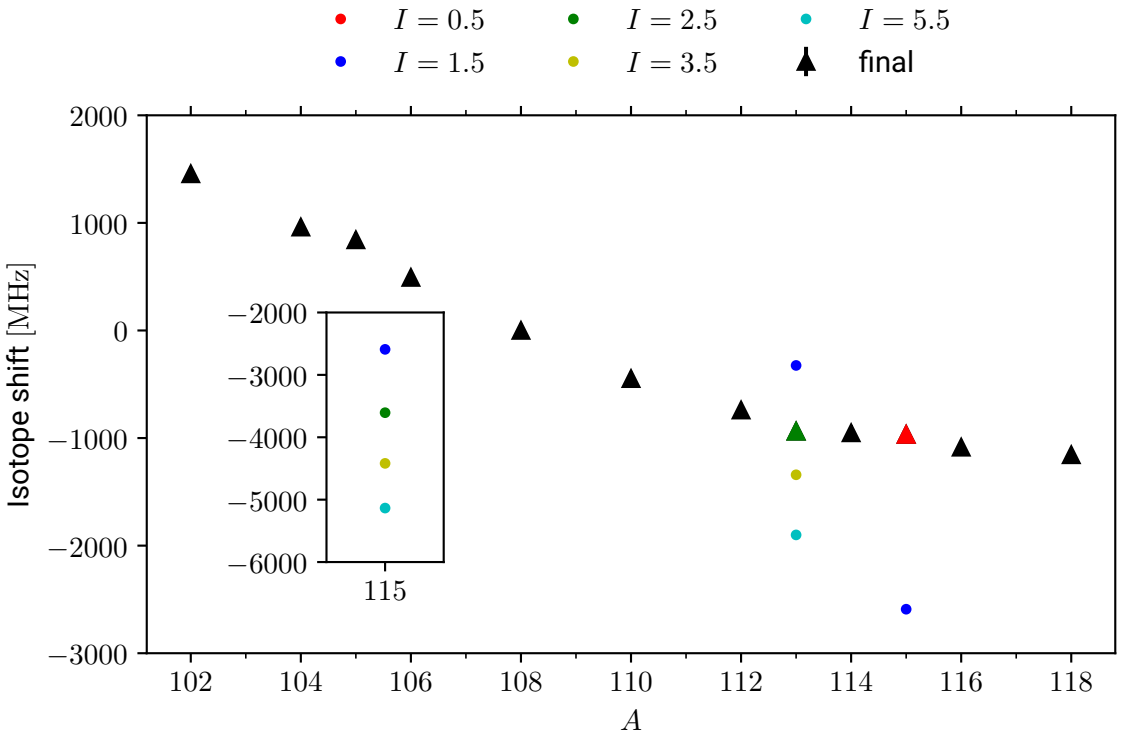

Figure 7.9: Isotope shifts along the isotopic chain of palladium determined in this work as a function of the mass number. For the neutron-rich isotopes ^{113}Pd and ^{115}Pd, different nuclear spins lead to different isotope shifts, which are plotted in different colors. The final values are presented as ▲. The inset shows the isotope shifts in MHz for the different spins of ^{115}Pd, which lie outside the range of the main chart.

7.1.7 Isotope Shifts

The isotope shifts of all isotopes were determined as described in Sec. 7.1.6 and are plotted in Fig. 7.9. For each isotope, the isotope shift was measured relative to ^{108}Pd, generated from the offline source.

To ensure, that the resonances from the offline source show the same shape and no systematic shifts compared to the resonances obtained with ions delivered from CARIBU, the center position of ^{110}Pd was determined once using ions from the offline laser ablation source, and once using ions from CARIBU. Figure 7.10 shows three different sets of online-offline measurements. For each run, the fitted center position is plotted. The sets have been recorded at different times during the second beamtime. The variation of the measured transition frequency within each set between online and offline measurement is in the same order as the

Table 7.3: Fit results of the hyperfine parameters with the assigned spins I. A_l and B_l are the hyperfine parameters of the $4d^9(^2\mathrm{D}_{5/2})5s\ ^2[5/2]_3$ (lower) state and A_u and B_u are the hyperfine parameters of the $4d^9(^2\mathrm{D}_{5/2})5p\ ^2[3/2]_2$ (upper) state. The uncertainties of the lower level, given in parentheses, are derived directly from the fit. The uncertainties of the upper level are propagated from the fit uncertainties of the lower levels and the ratios.

Isotope	I	A_l in MHz	B_l in MHz	A_u in MHz	$B_\mathrm{u}$in MHz
^{105}Pd	2.5	-391.178(1)	-652.91(2)	-82.1(2)	-305(2)
^{113}Pd	2.5	-292(1)	-1073(20)	-61.2(3)	-501(13)
^{115}Pd	0.5	-906(3)	0	-190.2(8)	0

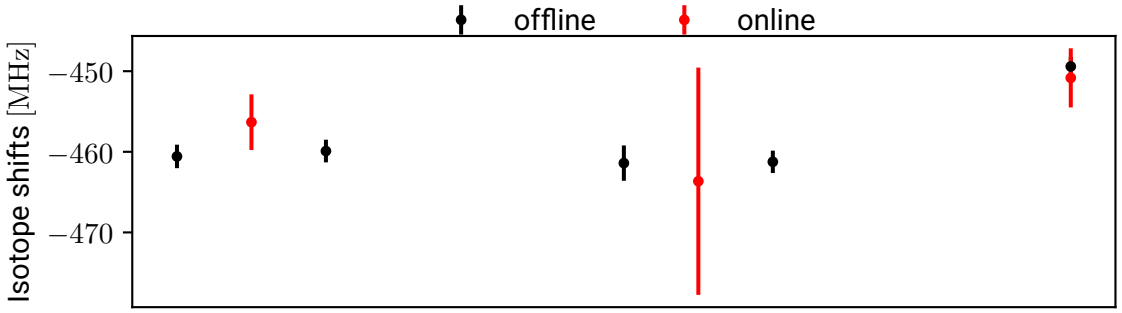

Figure 7.10: Isotope shifts of ^{110}Pd determined using offline (black) and online (red) beams. The first group of measurements was performed within 5 hours, the next group within 20 minutes and the last two measurements were performed within 20 minutes. For both measurement times, no major drifts, that could compromise the test of online-offline influence, are observed.

total variation of all runs. No systematic difference in the center position depending on online or offline beam is observed.

Comparing the residuals, the resonance shape, plotted in Fig. 7.11, does not show an observable difference between online and offline beam, but, since the ion yields from CARIBU are much smaller than those from the offline source, the statistics of the online resonance is too low for an accurate comparison of the shape. The shape parameters of the fitted Voigt profiles are for the offline resonance $\gamma_\mathrm{off} = (24.0 \pm 4.3)$ MHz and $\sigma_\mathrm{off} = (4.8 \pm 8.6)$ MHz, and for the online resonance $\gamma_\mathrm{on} = (20 \pm 813)$ MHz and $\sigma_\mathrm{on} = (0 \pm 73\,000)$ MHz. This yields a total FWHM of the Voigt profiles of (24.5 ± 4.5) MHz for the offline and (20 ± 813) MHz for the online beam. The large uncertainties for the online spectrum is due to the low statistics. A simple Gaussian fit yields comparable standard deviations of $\sigma_\mathrm{off} = (24 \pm 1)$ MHz and $\sigma_\mathbf{on} = (16 \pm 3)$ MHz.

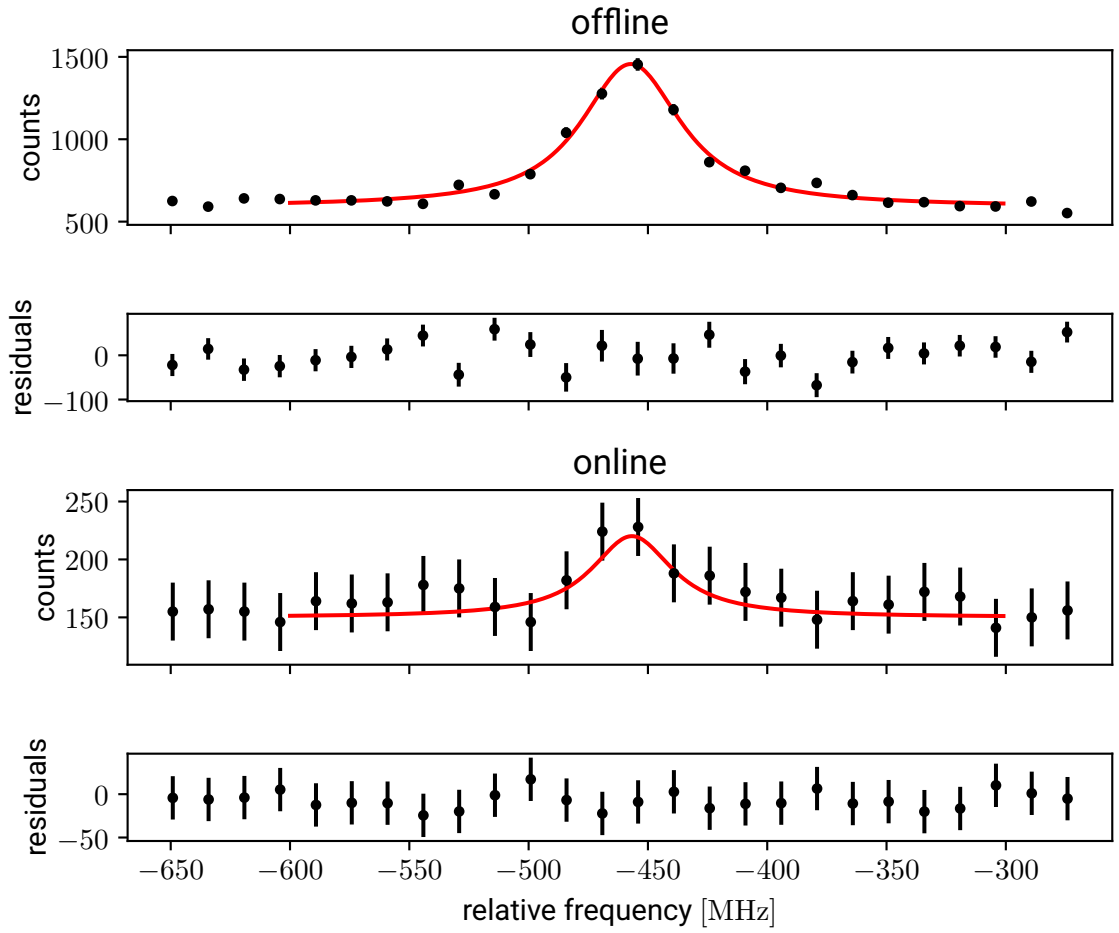

Figure 7.11: Resonance spectrum of ^{110}Pd taken with online and offline beam. Voigt profiles are fitted to the data, yielding $\gamma_{\text{off}} = (24.0 \pm 4.3)\,\text{MHz}$ and $\gamma_{\text{on}} = (20 \pm 813)\,\text{MHz}$, and with $\sigma_{\text{off}} = (4.8 \pm 8.6)\,\text{MHz}$ and $\sigma_{\text{on}} = (0 \pm 73\,000)\,\text{MHz}$, and the residuals are plotted.

7.1.8 Uncertainties

Both the center position of the reference and of the isotope of interest have a fit uncertainty from the least squares analysis. As Eq. (5.5) interpolates the center position of the reference, its uncertainty is calculated by

$$\Delta\nu_{\text{ref}}(t) = \sqrt{\left(\frac{t_{i+1} - t}{t_{i+1} - t_i}\Delta\nu_i\right)^2 + \left(\frac{t - t_i}{t_{i+1} - t_i}\Delta\nu_{i+1}\right)^2} \tag{7.12}$$

with the uncertainties $\Delta\nu_i$ and $\Delta\nu_{i+1}$ of the two reference measurements. This uncertainty of the reference position is added quadratically to the uncertainty of the center position of the isotope of interest. This propagation of the statistical fit uncertainty is done individually for each run, before the weighted mean is calculated for the final isotope shift. For the isotopes, for which more than one run was used to determine the isotope shift, the final statistical uncertainty was conservatively chosen to be the maximum of the standard deviation and the mean of the fit uncertainties.

Additionally to the statistical uncertainty from the fit, there are also some systematic effects contributing to the uncertainty. One of the main contributions is the uncertainty of the acceleration and Doppler-tuning voltages U_{acc} and U_{scan}. As the main acceleration voltage is measured with a high-voltage divider with a scaling ratio of $M = 5961.43$ the uncertainty of this ratio of $\frac{\Delta M}{M} = 1 \cdot 10^{-5}$ contributes to the uncertainty of the velocity of the ions. Since the used multimeter was, unfortunately, uncalibrated during the beamtimes, the absolute voltage might have an additional offset, but the beam-energy calibration described in Sec. 7.1.4 takes care of this offset.

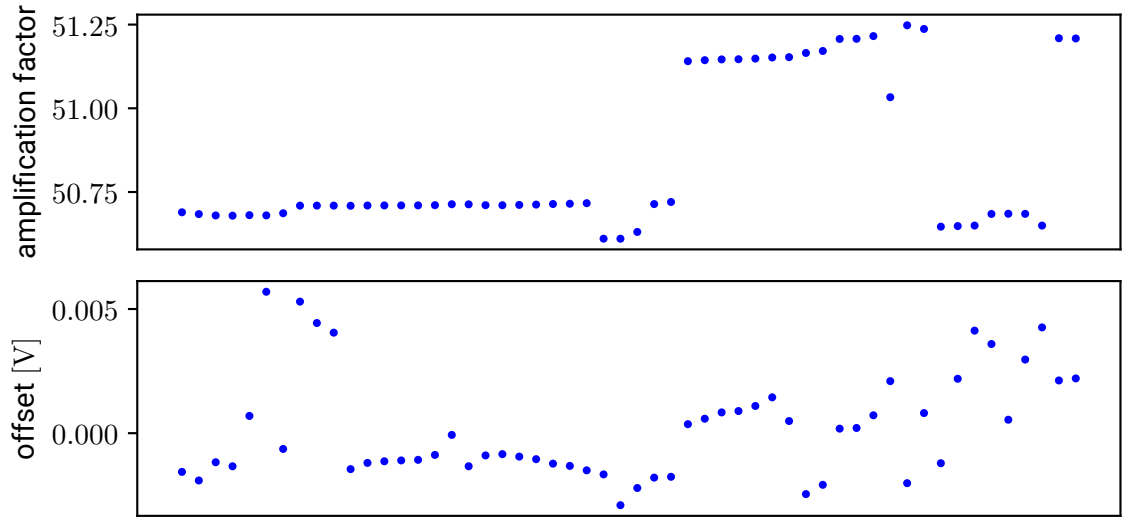

Figure 7.12: Amplification factors and offsets of the Doppler-tuning voltage interpolated for example runs. The amplification factor scatters by $\approx \pm 0.5$ and the offset by $\approx \pm 0.004\,\text{V}$.

The uncertainty of the Doppler-tuning voltage comes from the uncertainty of the amplification factor and offset which is interpolated from two measurements, as described in Sec. 7.1.5. The corresponding uncertainty is calculated from the fit uncertainties similarly as in Eq. (7.12), leading to uncertainties of the amplification factor in the order of 10^{-8} and uncertainties of the offset of the Doppler-tuning voltage in the order of $10^{-7}\,\text{V}$. Comparing the amplification

factor and offset during the second beamtime in Fig. 7.12 shows that the factor is scattering by ± 0.5 and the offset by ± 0.004 V, making the uncertainties from the interpolation negligible. With the amplification factor of of ≈ 51, the contribution of the offset uncertainty is small compared to the one of the amplification factor. The relative uncertainty of the scanning voltage is therefore approximately $\Delta U_{\text{scan}}/U_{\text{scan}} \approx 0.5/51 = 0.0098$.

The relative uncertainties of the masses are of the order of $10^{-12} - 10^{-8}$ leading to completely negligible uncertainties of $10^{-7} - 10^{-3}$ MHz. The wavemeter used for the laser frequency measurement was continuously calibrated on a He:Ne reference laser. The wavemeter stability in this configuration was extensively investigated in [119, 89] and a upper bound of the drift between reference and online isotope of < 1 MHz can be expected. Uncertainties coming from the non-linearity of the setpoint in the wavemeter were also investigated in [119] and an uncertainty of < 2 MHz can be expected. This uncertainty contributes to each isotope shift measurement, as the laser frequency was changed between isotope and reference measurement by several 100 MHz. Since the spectroscopy laser is frequency doubled, a final laser frequency uncertainty of $\Delta\nu_{\text{L}} = 2$ MHz is assumed for the estimation of the systematic uncertainty of the isotope shift.

The chosen time-gate width also introduces a systematic uncertainty. To investigate its contribution, for a set of randomly chosen ^{108}Pd measurements, the time-gate width was varied between 1 and 3σ of the Gaussian fit, i.e. between 0.6 and 1.8 µs. For each measurement, the standard deviation of the resulting center positions was calculated. The mean of all standard deviation of 0.66 MHz is considered as the systematic uncertainty $\Delta\nu_{\text{tg}}$, coming from the chosen time-gate width.

The total systematic uncertainty can be estimated by

$$\Delta\delta\nu^{A,A'} = \sqrt{\left(\Delta\delta\nu^{A,A'}_{U_{\text{b}}}\right)^2 + \left(\Delta\delta\nu^{A,A'}_{U_{\text{s}}}\right)^2 + (\Delta\delta\nu_{\text{L}})^2 + \left(\Delta\delta\nu_{\text{tg}}\right)^2} \tag{7.13}$$

where

$$\Delta\delta\nu^{A,A'}_{U_{\text{b}}} = C\frac{\Delta M}{M}\left|\nu^A_{\text{L}} - \nu^{A'}_{L} - \frac{1}{2}\left[\nu^A_{\text{L}}\frac{\delta m}{m} + \frac{\nu^{A'}_{\text{L}}U^{A'}_{\text{scan}} - \nu^A_{\text{L}}U^A_{\text{scan}}}{U_{\text{acc}}}\right]\right| \tag{7.14}$$

$$\Delta\delta\nu^{A,A'}_{U_{\text{s}}} = C\sqrt{(\nu^A_{\text{L}})^2 + (\nu^{A'}_{\text{L}})^2}\,\frac{U_{\text{scan}}}{U_{\text{acc}}}\,\frac{\Delta U_{\text{scan}}}{U_{\text{scan}}} \tag{7.15}$$

$$C = \sqrt{\frac{eU_{\text{acc}}}{2mc^2}}. \tag{7.16}$$

with $\delta m = m_{\text{A}} - m_{\text{A}'}$. The derivation of this formula can be performed analogously to the one presented in[43], but considering the different laser frequencies that were applied. This

total systematic uncertainty is calculated for each individual isotope shift measurement and for the final systematic uncertainty, the average value is taken. All isotope shifts, their statistical uncertainties and their systematic uncertainties determined within this work are listed in Tab. 7.4.

Table 7.4: Measured Isotope shifts of palladium. The statistical uncertainties are given in parentheses and systematic uncertainties in brackets.

Isotope	$\delta\nu^{A,108}$ [MHz]
^{102}Pd	$1455.6(38)[74]$
^{104}Pd	$960.4(61)[205]$
^{105}Pd	$842.0(23)[96]$
^{106}Pd	$492.5(19)[159]$
^{110}Pd	$-448.0(30)[27]$
^{112}Pd	$-740.2(64)[21]$
^{113}Pd	$-937.1(100)[21]$
^{114}Pd	$-952.0(26)[21]$
^{115}Pd	$-966.8(53)[21]$
^{116}Pd	$-1085.6(22)[21]$
^{118}Pd	$-1155.0(210)[21]$

7.1.9 Nuclear Moments

The magnetic dipole moment and electric quadrupole moment of a nucleus can be extracted from the hyperfine-structure parameters according to Eqs. (2.48) with respect to the moments of a reference nucleus. For the stable odd isotope ^{105}Pd, the nuclear moments are known to be $\mu_{\text{ref}} = (-0.639 \pm 0.003)\,\mu_{\text{N}}$ [128] and $Q_{\text{ref}} = (0.660 \pm 0.011)\,\text{b}$ [129]. The results for the calculated nuclear moments will be the same for the upper and the lower level, since the ratios A_u/A_l and B_u/B_l where fixed during the fit. This neglects a possible hyperfine-structure anomaly. In the neighboring chain of ruthenium this is about $2 \cdot 10^{-4}$ for ^{99,101}Ru [130], which both have the same spin ($5/2^+$). Since the spin of ^{113}Pd is identical to that of ^{105}Pd, it is assumed that the hyperfine-structure anomaly is also smaller than the assigned uncertainty of about $0.5\,\%$. For ^{115}Pd, one must be a bit more careful due to the different spin. In these cases, the hyperfine-structure anomaly can be an order of magnitude larger as observed, e.g. in the silver isotopes ^{107,103,109}Ag [130]. But even then, the additional uncertainty would be just $20\,\%$ of our statistical uncertainty. The nuclear moments were calculated from the parameters of the lower levels, as the uncertainty can then be directly extracted and is independent of the uncertainties of the A- and B-ratios. The results are presented in Tab. 7.5.

Table 7.5: Nuclear magnetic dipole moments μ and electric quadrupole moments Q of the odd isotopes. The statistical uncertainties are given in parentheses. The value for the magnetic dipole moment of ^{105}Pd is taken from [128] and for the electric quadrupole moment from [129].

Isotope	μ [μ_N]	Q [b]
^{105}Pd (ref.)	-0.639(3)	0.660(11)
^{113}Pd	-0.477(3)	1.08(3)
^{115}Pd	-0.296(2)	

7.1.10 Nuclear Charge Radii

For the stable isotopes of palladium the differential ms nuclear charge radii can be calculated from the Barret radii $R_{k\alpha}$ listed in [55] according to Eq. (5.7). In this calculation the V_2-ratios can be treated without uncertainties, which are expected to be of the order of 10^{-4} [55]. The literature values for palladium calculated by Eq. (5.7) and from the Barret radii listed in [55], and their uncertainties calculated by Eq. (5.8) are listed in Tab. 7.6 and were used for the King-Plot analysis.

Table 7.6: Differential ms nuclear charge radii $\delta\langle r^2\rangle$ calculated from Barret radii from [55] and isotope shifts measured within this work.

Isotope pair	$\delta\langle r^2\rangle$ [fm^2]	$\delta\nu^{A,A'}$ [MHz]
102-104	$-0.2312(60)$	$489.7(41)$
104-105	$-0.0700(75)$	$118.7(12)$
105-106	$-0.1533(35)$	$346.1(32)$
104-106	$-0.2233(55)$	$465.2(30)$
106-108	$-0.2239(54)$	$495.0(16)$
108-110	$-0.2045(58)$	$442.1(8)$

King-Plot Analysis

As described in Sec. 7.1.1, separate measurements of the stable Pd isotopes were performed for the King-Plot analysis during a third beamtime. For each pair of isotopes listed in Tab. 7.6, the isotope shift was measured. Like for the King plot for lead, Eq. (2.41) is modified by the fitting constant α such that the function

$$\widetilde{\delta\nu}^{A,A'} = K_\alpha + F \cdot (\widetilde{\delta\langle r^2\rangle}^{A,A'} - \alpha) \tag{7.17}$$

can be fitted to the data points. The fit results give a mass shift factor of $K_{\mathrm{MS}} = K_\alpha - F \cdot \alpha = (-2756 \pm 259)$ u GHz and a field shift factor of $F = (-2.7 \pm 0.2)$ GHz/fm^2.

Figure 7.13 shows the King Plot with the stable isotope pairs used for the fitting. Additionally, the measured isotopes shifts of the second beamtime are marked in red to illustrate the extraction of the differential ms nuclear charge radii of all isotopes relative to ^{108}Pd. Their values are tabulated in Tab. 7.7 and are discussed in Sec. 7.2.

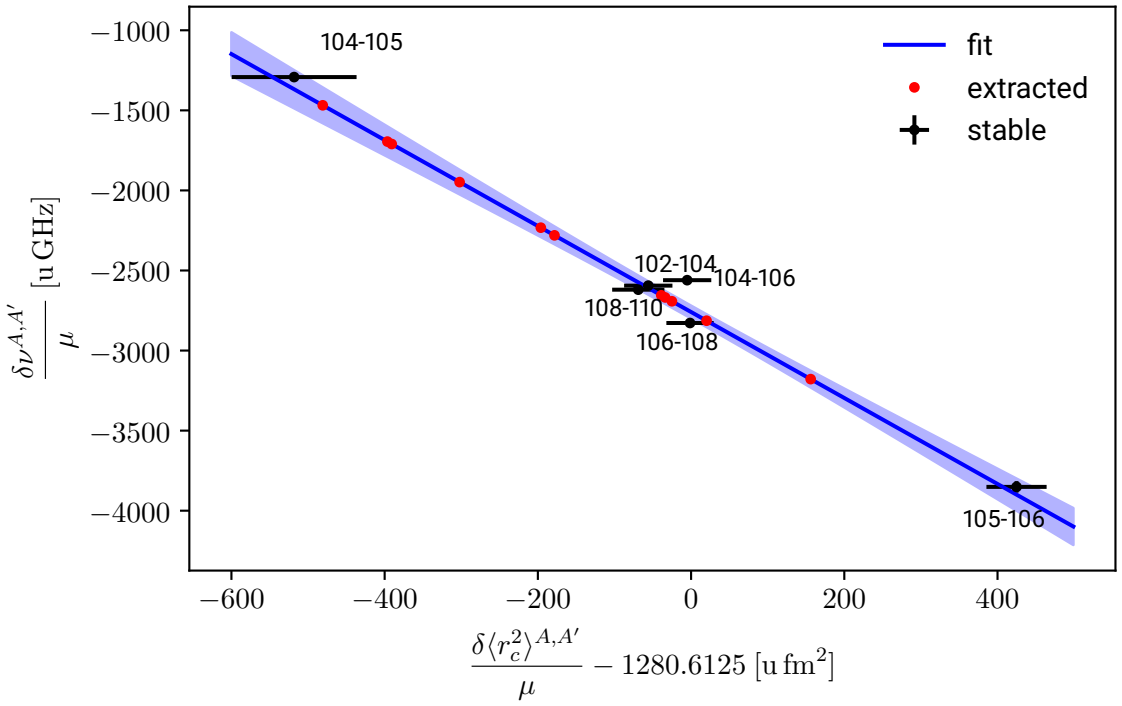

Figure 7.13: King-Plot with the literature values of the differential ms charge radii and measured isotope shifts of the stable isotopes. A linear function is fitted to the data according to the King-Plot procedure. The red data points illustrate the extraction of the differential ms nuclear charge radii of all investigated isotopes from the measured isotope shifts.

7.2 Discussion

7.2.1 Nuclear Moments

From the nuclear magnetic dipole moments, the experimental g-factors are calculated using $\mu = gI\mu_N$ and are plotted in Fig. 7.14 in comparison to the neighboring even-Z isotopic chains. For all isotopes with the odd neutron in the $2d_{5/2}$ level, the experimental g-factors show an

Table 7.7: Differential ms nuclear charge radii $\delta\langle r^2\rangle^{A,108}$. The uncertainties given in parentheses include the statistical uncertainties from the isotope shift and the systematic uncertainties from the King-plot procedure.

Isotope	$\delta\langle r^2\rangle^{A,108}$ [fm^2]
^{102}Pd	-0.6802(14)[82]
^{104}Pd	-0.4480(23)[53]
^{105}Pd	-0.3806(9)[51]
^{106}Pd	-0.2277(7)[26]
^{110}Pd	0.2096(11)[25]
^{112}Pd	0.3596(24)[71]
^{113}Pd	0.4530(37)[85]
^{114}Pd	0.4782(10)[139]
^{115}Pd	0.5031(20)[197]
^{116}Pd	0.5664(8)[226]
^{118}Pd	0.6296(78)[327]

overall constant trend along the isotopic chains. While the experimental g-factors of the magic tin isotopes agree very well with the single-particle g-factors calculated from Eq. (2.8) with $g_{\text{eff}} = 0.6 \cdot g_s$, a slightly larger deviation is observed for the other isotopic chains, hinting to an enhanced mixing of states.

According to the single-particle model, a sudden change of the nuclear g-factor is expected along the isotopic chain, when the unpaired, odd neutron occupies a different level than in the neighboring odd isotope. This behavior is very well met by the tin isotopic chain: The experimental nuclear g-factors of $^{105-109}$Sn agree very well with the expected single-particle g-factor of the $2d_{5/2}$ level, while the experimental g-factors of $^{113-119}$Sn are close to the single-particle g-factor of the $3s_{1/2}$ level, but show a linear deviation from the expected constant g-factor. This hints to a stronger mixing of the different neutron levels in the nuclear wave function in the neutron-midshell region, already for the semi-magic tin isotopes.

When moving away from the proton shell closure $Z = 50$, a very pronounced trend of the $I = 1/2$ states is observed: From Sn ($Z = 50$) over Cd ($Z = 48$) to Pd ($Z = 46$), the quenching of the g-factor increases, until for Ru ($Z = 44$) the g-factor becomes positive. Already for Pd, the change in the g-factor from ^{113}Pd ($I = 5/2$) to ^{115}Pd ($I = 1/2$) is not pronounced anymore. The same is observed for Xe isotopes ($Z = 50 + 4$, Pd: $Z = 50 - 4$): the g-factors are of very similar size and no sudden change from the $I = 5/2$ to $I = 1/2$ isotopes is observed. Before this behavior is discussed in more detail, the results of the quadrupole moments are presented.

Figure 7.15 shows the experimental quadrupole moments of palladium and those of the even-Z elements in the vicinity of Pd, over their neutron numbers N. All isotopic chains exhibit

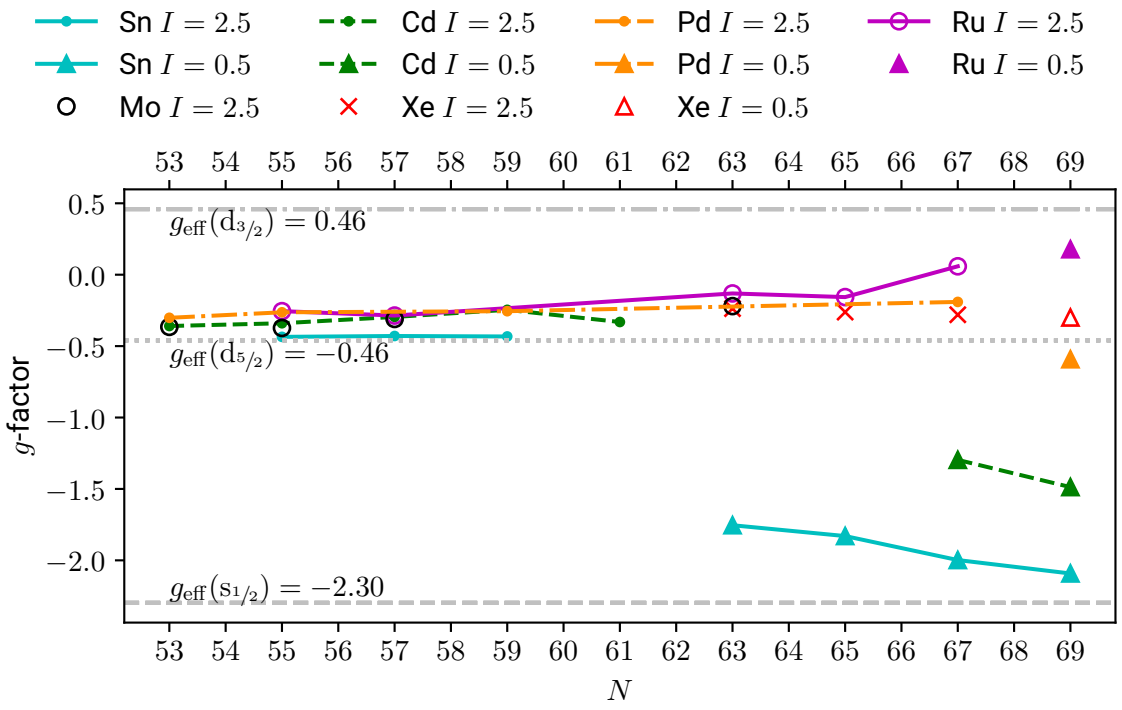

Figure 7.14: Experimental nuclear g-factors of $I = {}^1/_2, {}^5/_2$ isotopes of Pd from this work and [131, 128] and of the neighboring isotopes of Xe [132], Sn [133, 59], Cd [134, 135], Ru [B. Maaß, private communication] and Mo [132, 136] together with the single-particle effective g-factors for the $2\text{d}_{3/2}$, $2\text{d}_{5/2}$ and $3\text{s}_{1/2}$ levels in this region ($g_{\text{eff}} = 0.6 \cdot g_s$). The magnetic moments in the isotopic chains of Sn, Cd and Pd with the same spin are connected by lines for better visibility.

an increasing trend. The investigated isotopes with $N < 55$ have a negative quadrupole moment, which can still be explained in the single-particle spherical shell model with Eq. (2.13).

The trend of quadrupole moments of the magic tin isotopes can be interpreted as a sequential filling of the $2\text{d}_{5/2}$ level with a potential zero crossing at $N = 53$ [133]. At $N = 60$, the level is completely filled, which agrees with the linearly increasing trend in the Sn quadrupole moments. At $N = 61$ the linear trend is broken, which can be explained by the filling of a $1\text{g}_{7/2} \times 2\text{d}_{5/2}$ configuration with three neutrons in the $2\text{d}_{5/2}$ and one neutron-pair in the $1\text{g}_{7/2}$ level [133].

Removing two protons, i.e., looking at Cd, shows a very similar trend but larger values of the quadrupole moment. This indicates a stronger polarization effect and can be accounted for by a larger effective charge in the nuclear shell model. One has to keep in mind though, that by moving towards proton mid-shell from the proton shell closure, pronounced deformation

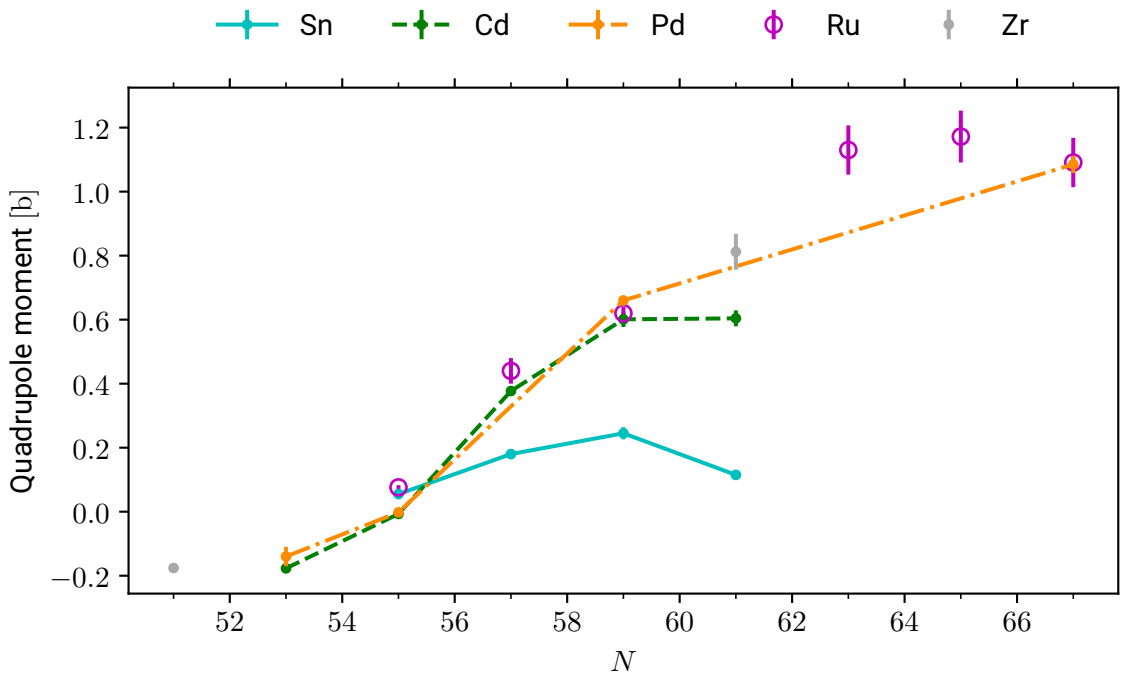

Figure 7.15: Experimental spectroscopic quadrupole moments of the ground state nuclei of palladium from this work and [131] and its neighboring isotopes Zr [36], Ru, Cd [135] and Sn [133]. For better visibility the data points of Sn, Cd and Pd are connected.

can occur, which restricts the use of the spherical shell model and will also affect the magnetic moments since level mixing will increase.

Thus, it is no surprise that two more protons away ($Z = 46$, Pd), the general trend from the now available values of Pd quadrupole moments also agree with the trend observed in Cd and Sn. Also, the size of the quadrupole moment is similar to the one observed in Cd. At $N = 57$, the size of the quadrupole moments start deviating from one element to the other. For Sn, the quadrupole moments do not increase very strongly while for the other elements with $Z < 50$, a stronger increase is observed. For the $N = 61$ isotopes, the same ordering as in the magnetic dipole moments at $N = 69$ is observed: The further away the element is from the proton shell closure, the larger is the size of the quadrupole moment. This indicates stronger mixing of the levels in the nuclear wave function for this neutron number region and agrees with the observations made in nuclear charge radii when crossing $N = 60$, which will be discussed in the next section. But in order to be able to precisely compare the evolution of the quadrupole moment in palladium, more odd-N isotopes need to be investigated. Nevertheless, the trend to relatively large quadrupole moments in the mid shell region is obvious

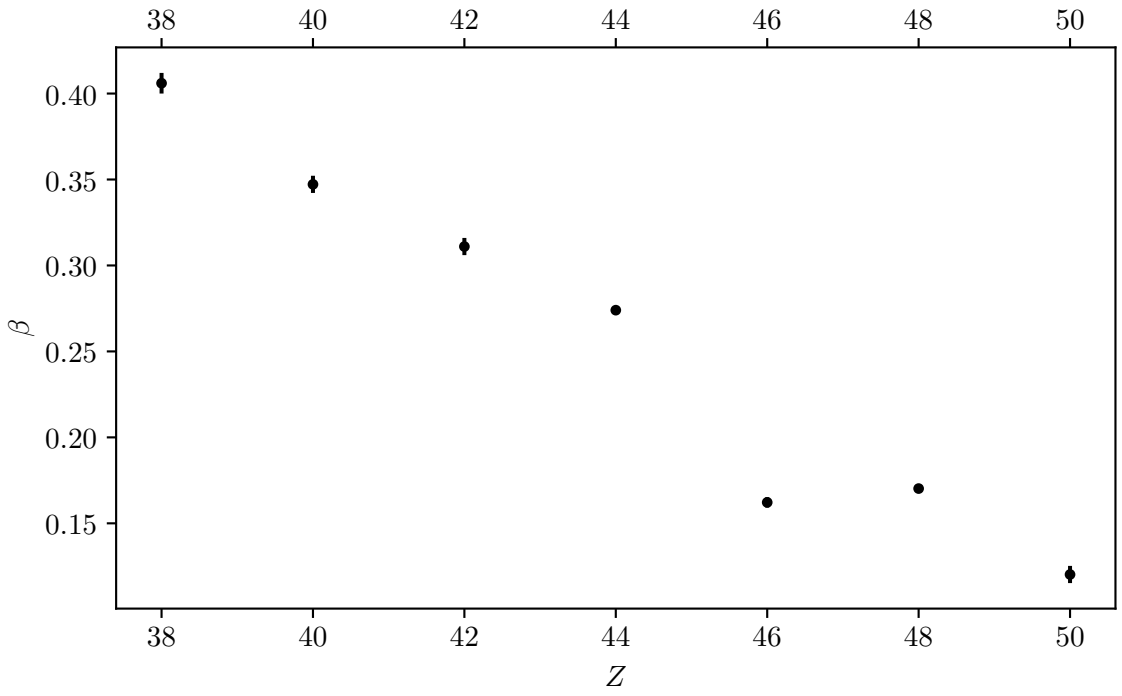

Figure 7.16: Deformation parameter β of the $N = 60$ isotopes in the palladium region. The values are taken from [51]. The deformation parameter shows an increasing trend when approaching the mid-shell region.

and Ru does have similarly or even larger quadrupole moments. This, in combination with the larger deformation parameters β of the even-even isotopes at $N = 60$ in this region shown in Fig. 7.16, indicates that the spherical shell model might not be appropriate anymore. Indeed, some of the observations can be explained using the deformed nuclear shell model (Nilsson model).

For the neutron mid-shell ^{114}Pd isotope, the NuDat3 database [51] lists a deformation parameter of $\beta_2 = 0.25$, which corresponds to a quadrupole deformation parameter $\epsilon_2 \sim 0.2$. Figure 7.17 shows the dependence of the single-particle energy levels for neutrons on the deformation ϵ_2, according to the Nilsson model [138]. The red rectangle marks the area in the plot which is relevant for the neutron-rich Pd isotopes. The Fermi level of the 19 neutrons above $N = 50$ lies in the region of the crossing of the 1/2[411], 5/2[402], and the (negative parity) 5/2[532] levels. The spins and parities of ^{115}Pd excitations given in [51] can all be found within this area, although the ordering is -expectedly- not in perfect agreement. Thus, it is plausible, that the $^1/_2{}^+$ state in ^{115}Pd is the 1/2[411] level originating from the (spherical) $3s_{1/2}$ level. The Nilsson diagram also predicts a mixing of the $2d_{3/2}$ with the $3s_{1/2}$ level,

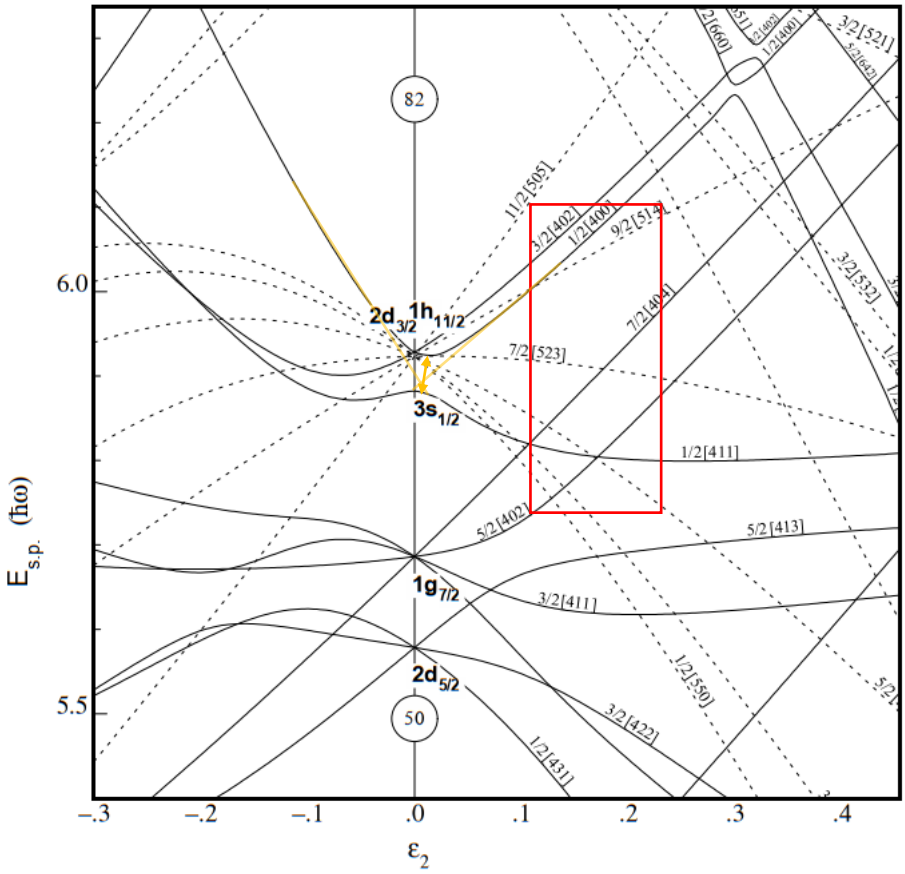

Figure 7.17: Nilsson diagram for neutrons [137]. The diagram shows the single-particle energy levels of neutrons in dependence of the quadrupole deformation parameter ϵ_2. The red rectangle highlights the part of the diagram relevant for neutron-rich Pd isotopes. The yellow marks indicate the repelling between the $^1/_2$[400] and $^1/_2$[411] levels.

indicated by the yellow marks in Fig. 7.17. Level mixing could explain why the nuclear magnetic dipole moment of ^{115}Pd measured within this work is shifted upward from the negative Schmidt value for the $s_{1/2}$ level, closer to the positive Schmidt value of the $d_{3/2}$ level, which is also plotted in Fig. 7.14. The energy trend of the relevant 1/2[411] in the Nilsson diagram becomes rather flat with increasing deformation. It is possibly repelled by the lower-lying 1/2[420] level (from $g_{7/2}$). Additional admixture of this state, which also has a positive g-factor, may further enhance the trend towards positive g-factors and finally push the state in Ru in the positive region.

7.2.2 Charge Radii

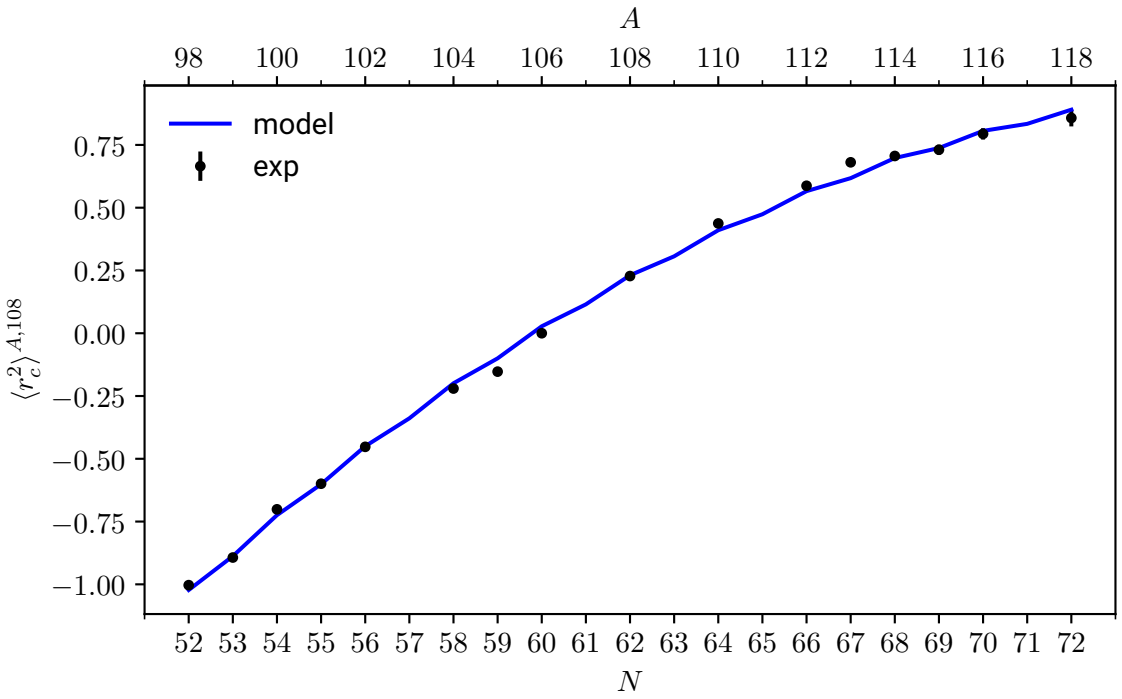

Figure 7.18: Differential ms nuclear charge radii of palladium. Experimental results from this work and [16] (for $^{98-101}$Pd) are marked a black dots. The blue line is a fit of the model of Zamick and Talmi to the experimental values (see text).

The differential ms charge radii of Pd are plotted in Fig. 7.18 and show a linear increasing trend with an additional parabolic shape. The plot also shows a superimposed odd-even staggering, but for ^{113}Pd, the OES is inverted compared to normal OES, i.e., the nuclear charge radius of ^{113}Pd is larger than the radii of its neighbors. Zamick and Talmi proposed a param-

eterization of the differential ms nuclear charge radius [139, 140], which can be specifically applied to isotopic chains which span between $50 \leq N \leq 82$ by

$$\delta\langle r_c^2\rangle = a(N-50) + b(N-50)(82-N) + \frac{c}{2}\left[1-(-1)^N\right] + d. \tag{7.18}$$

The parameter a accounts for the volume effect, i.e., the linearly increasing trend with increasing neutron number. The deformation is accounted for by the parameter b, leading to a maximum deformation in mid-shell, i.e., at $N = 66$. The parameter c describes the strength of normal odd-even staggering, and the offset d depends on the chosen reference isotope.

A fit of this parameterization to the Pd data yields a volume effect of $a = 0.072\,\mathrm{fm}^2$, which is identical to the one observed in the neighboring cadmium isotopes [117]. Since the inverted OES at ^{113}Pd cannot be described by the Zamick-Talmi model, the fit yields $c = -0.017\,\mathrm{fm}^2$, which is smaller than the one in Cd [117] and also too small to describe the normal OES in ^{105}Pd.

The deformation parameter $b = 0.0030\,\mathrm{fm}^2$ fitted to the Pd isotopes is larger than in the Cd isotopes ($b = 0.0017\,\mathrm{fm}^2$ [117]). For the neutron mid-shell isotope ^{112}Pd, it leads to a deformation contribution of $\delta\langle r_c^2\rangle_{\mathrm{def}} = b \cdot 16^2 = 0.768\,\mathrm{fm}^2$. Using Eq. (2.22), this yields a deformation parameter $\langle\beta_2^2\rangle = 0.094$, which is almost twice the deformation of ^{114}Cd according to the Zamick-Talmi model [117].

For a further comparison of the differential ms nuclear charge radii of Pd to neighboring isotopic chains, Fig. 7.19 shows the experimental values for isotopic chains between $Z = 36$ and $Z = 50$.

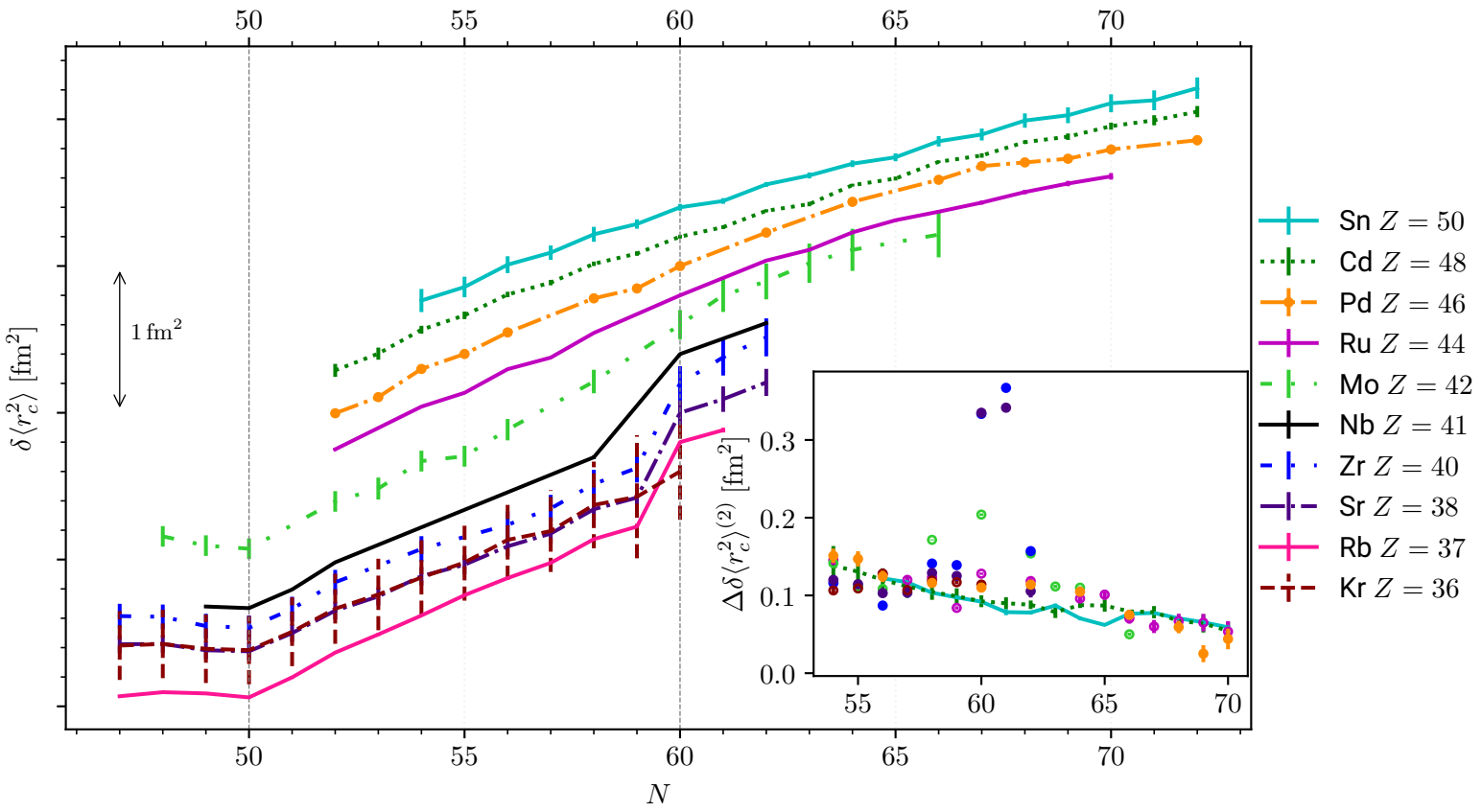

Figure 7.19: Differential mean-square nuclear charge radii $\delta\langle r_c^2\rangle^{A,A'}$ of the palladium and neighboring isotopic chains. Values for $^{98-101}\mathrm{Pd}_{52-55}$ are taken from [16]. For comparison, experimental values for Sn [133], Cd [141], Ru [B. Maaß, private communication], Mo [33], Nb [34], Zr [35, 36], Sr [37, 38], Rb [39] and Kr [142] are also plotted. The inset shows the $2N$-derivative $\Delta\delta\langle r_c^2\rangle^{(2)}$ of the differential mean-square nuclear charge radii for the same isotopic chains in $N = 56 - 70$ region.

For the isotopic chains of Rb up to Nb, a sudden increase of the nuclear charge radius at $N = 60$ has been observed, related to a sudden shape-change from prolate to oblate nuclei [32]. This sudden increase gets smoother in Mo ($Z = 42$), and the overall slope in this neutron-number region decreases until $Z = 48$, Cd.

To investigate the deviations between the isotopic chains, the $2N$-derivatives of the differential ms charge radii

$$\Delta\delta\langle r_c^2\rangle^{(2)}(A) = \frac{\delta\langle r_c^2\rangle^{A,A'} - \delta\langle r_c^2\rangle^{A-2,A'}}{2} \tag{7.19}$$

are plotted in the inset of Fig. 7.19. In this so-called Brix-Kopfermann plot, the influence of the odd-even staggering is removed, and only the change between two even or two odd isotopes remains. The inset shows the $N = 56 - 70$ region, where the strongest deviations between the isotopic chains appear, including the sudden shape change at $N = 60$.

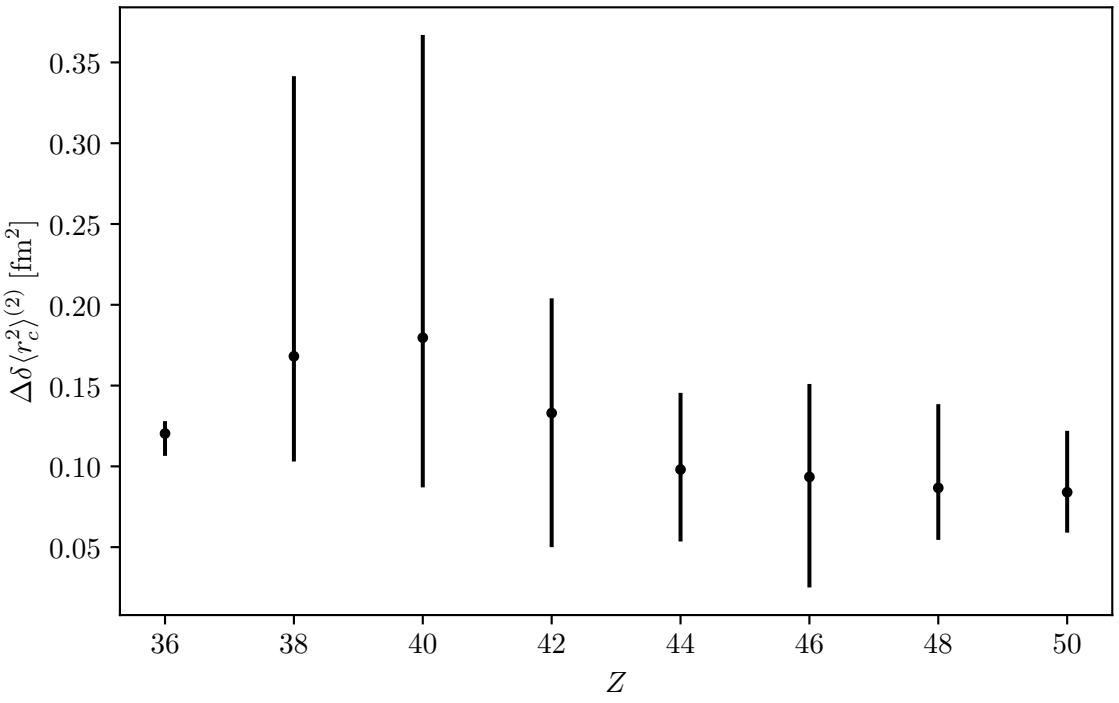

Figure 7.20: Mean $2N$-derivative $\Delta\delta\langle r_c^2\rangle^{(2)}$ of Sn, Cd, Pd, Mo, Zr and Kr versus the proton number Z. The mean is taken from isotopes with $56 < N < 70$, as available. The ends of the error bars mark the maximum and minimum values for each element and are meant to represent the range of variation for the respective Z.

The mean $2N$-derivative for each element in this neutron number region is plotted in Fig. 7.20. The maximum appears at $Z = 40$, Zr, exactly in the middle of the $Z = 50$ shell, and the $2N$-

derivative decreases when approaching both neutron shell closures $Z = 28$ and $Z = 50$.

When looking at small-scale effects an inverted odd-even staggering (OES) is observed for ^{113}Pd$_{67}$. Such an inverted OES pattern is also visible in the $Z = 42$, Mo isotopic chain between $N = 60 - 64$ (the odd-N isotopes below and above have yet to be measured) but not for any other isotopic chain in this region. For a detailed investigation of the odd-even staggering, the OES parameter defined in Eq. (6.6) is plotted in Fig. 7.21. It shows for experimental data

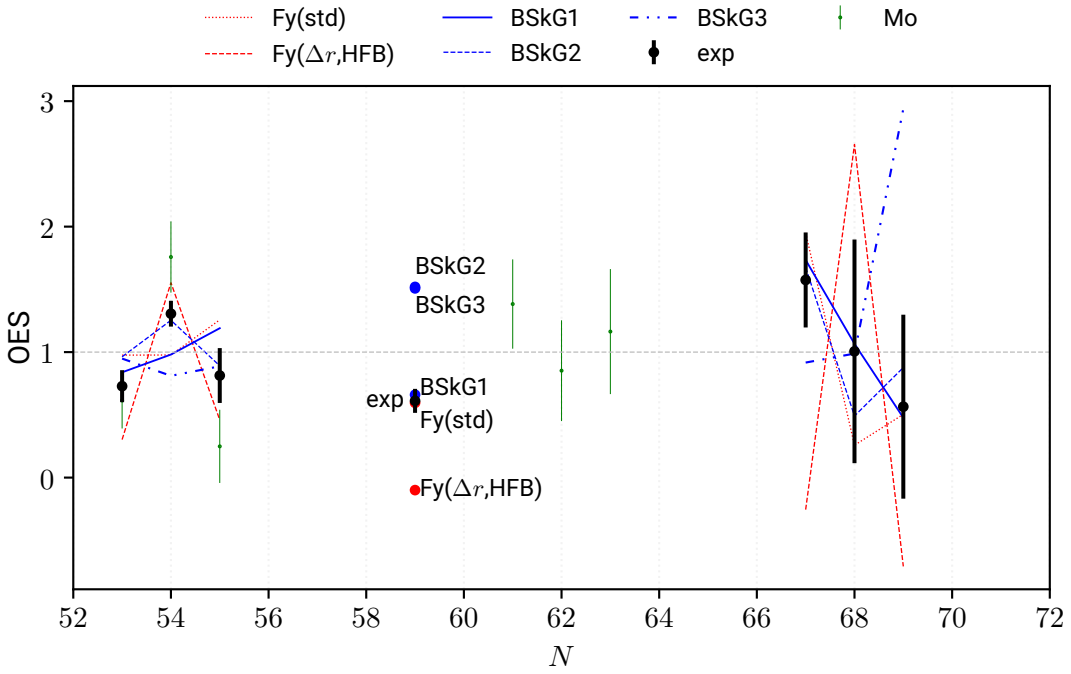

Figure 7.21: Experimental and theoretical odd-even staggering (OES) of palladium. For $N \leq 59$ and $N > 68$ normal OES is observed for Pd and inverted OES for $N = 67$. For Mo normal OES is observed for $N \leq 55$ and inverted OES for $N \geq 59$.

normal OES for the neutron-deficient isotopes of palladium as well as for ^{115}Pd while for ^{113}Pd an OES pattern inverted to normal OES shows up. The OES of Mo is also plotted for comparison and exhibits the same pattern as in Pd, i.e., normal OES for neutron-deficient isotopes and inverted OES for $N = 61 - 63$. The experimental results on radii and OES can now be compared to predictions from various nuclear models.

Fy(std) is a standard Fayans functional calculation based on a Hartree-Fock and Bardeen–Cooper–Schrieffer framework (HF–BCS) and with axial symmetry [13] adjusted to the Pd region [16]. Fy(Δr,BCS) was not only tuned to binding energies, but also to a few selected differential charge radii in order to describe OES by pairing interactions [13]. As this model

treats pairing such that the resulting particle and pair densities are not spatially localized and is therefore not well applicable for weakly bound nuclei, it was re-developed within a Hartree-Fock-Bogoliubov framework (Fy(Δr,HFB)) [15] and also adjusted to the palladium region [16].

The BSkG models [31, 41, 42] are Skyrme-EDF-based calculations in a Hatree-Fock-Bogoliubov framework allowing triaxiality. While the Fayans functionals Fy(std) and Fy(Δr,HFB) were tuned to one or two observables from restricted sets of isotopes, the BSkG models were adjusted to five observables of almost all nuclei for which these were available. Compared to BSkG1, BSkG2 does not rely on the Equal Filling Approximation (it breaks time-reversal symmetry for odd nuclei) and, therefore, allows for more general nuclear configurations compared to BSkG1. Additionally, it also contains information on the fission barriers of actinides.

For the BSkG3 model, a more microscopically founded treatment of pairing was employed and ground state reflection asymmetry is allowed. Constraints on infinite nuclear matter properties at high densities were included also, with the aim to predict the nuclear equation of state in heavy pulsars. This emphasises the fact, that the main goal was not the reproduction of nuclear charge radii.

The differential ms charge radii obtained from EDF calculations of Pd isotopes using these functionals are compared with the experimental values in Fig. 7.22. The Fy(std) calculation predicts a smaller slope of the differential ms charge radii than observed experimentally, especially in the neutron deficient region. The Fy(Δr,HFB) calculation predicts an overall larger slope of the differential ms charge radii for the Pd isotopic chain. Although the BSkG models' goal is the global reproduction of nuclear masses, all three BSkG models show a very good agreement with the experimental trend in the differential ms charge radii. BSkG2 predicts a slightly smaller slope than the experimental data.

Comparing the OES pattern to theoretical calculations in Fig. 7.21 shows that the Fy(std) cannot reproduce the small-scale effects for the neutron-deficient isotopes and also slightly deviates from the observed OES pattern in the neutron-rich isotopes. Fy(HFB) shows a similar but sightly overestimated OES pattern for the neutron-deficient isotopes in Fig. 7.21. It shows strong and normal OES for the neutron-rich isotopes, contrary to the experimental data. The BSkG1 calculation slightly deviates from the experimental OES parameters of the neutron-deficient isotopes while it shows very good agreement for ^{105}Pd and the neutron-rich isotopes. The BSkG2 model agrees with the experimental OES pattern of Pd for both neutron-deficient and neutron-rich isotopes, but mistakenly predicts inverted OES for ^{105}Pd. BSkG3 cannot reproduce the OES pattern for any of the palladium iosotpes.

A more detailed investigation of effects coming from different treatments of pairing, triax-

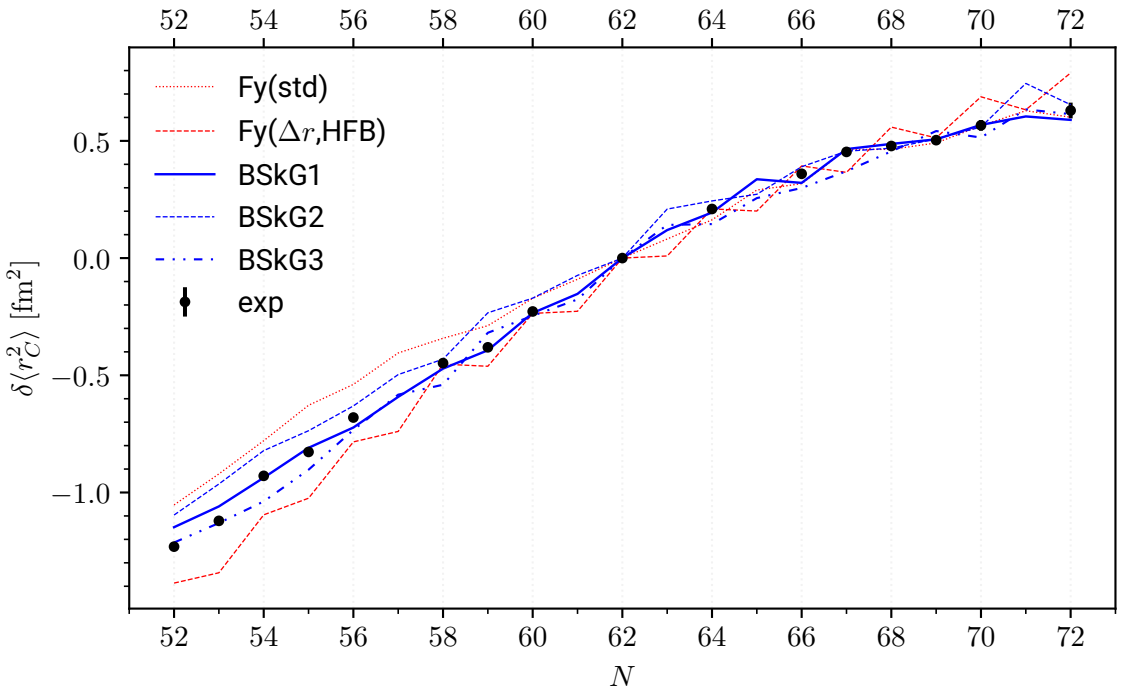

Figure 7.22: Experimental differential mean-square charge radii compared to density functional calculations employing the following functionals: Fy(std) and Fy(Δr,HFB)[16], BSkG1 [31], BSkG2 [41], BSkG3 [42]. See text for details about the functionals.

iality or time-reversal asymmetry is needed to understand the concrete origin of normal OES and inverted OES for the different neutron numbers, and the measurement of differential ms charge radii should be completed in this neutron number region for Pd and Mo.

Kumar et al. connect the smooth but strongly increasing slope in Mo between $N = 56 - 70$ to an increasing quadrupole deformation and triaxiality [143]. This interpretation could be adopted for palladium and agrees with the strong quadrupole moments observed for $N \geq 57$ and the good agreement between the observed differential ms nuclear charge radii and the ones calculated with triaxial BSkG models. But a direct comparison between axial and triaxial calculations is necessary for a compelling argumentation. Triaxiality could also explain the inverted OES, but the completion of experimental data is required for a final conclusion. Also it is interesting that, though BSkG3 should refine the description of nuclei compared to BSkG1 and BSkG2, it cannot reproduce the OES pattern observed in Pd while it agrees well with the overall trend. This deviation of the OES could be a sign, that the microscopic description of pairing is not appropriate for medium-mass nuclei like palladium.

8 Summary

This work has contributed to the investigation of nuclear properties of both spherical and deformed nuclei through precise collinear laser spectroscopy measurements on lead and palladium isotopes.

In the investigation of lead isotopes, the analysis of nuclear differential ms charge radii and electric and magnetic moments provided detailed insights into the nearly spherical isotopes at the $Z = 82$ proton-shell closure, below the neutron-shell closure at $N = 126$. The measurements of the differential ms charge radii of both, ground states and isomers, showed excellent agreement with theoretical predictions from the doubly magic ^{208}Pb down to ^{199}Pb. The Fayans EDF calculations reproduce the general trend excellently while the small-scale effect of odd-even staggering is much better reproduced by the first ab initio calculations in this region. A detailed discussion of the comparison of experimental and theoretical values is currently in progress and will be published in an upcoming paper.

The observed trends in the magnetic dipole moments can be interpreted in the picture of the spherical nuclear shell model. The observed increasing deviations towards neutron mid-shell are expected due to enhanced level mixing. The linear trend of nuclear quadrupole moments expected from the spherical nuclear shell model is met by the three ground-state isotopes closest to the $N = 126$ shell closure. Also the expected switch of the sign, when the filling of a new (sub-) shell starts, is observed in the ground-state quadrupole moments. These observed good agreements with expectations from the spherical nuclear shell model support the magicity of lead.

The behavior of the isomer shift, which is slightly different from the trend observed in magic tin isomers [27], is not yet understood and opens up the question, if it can be related to the unique-parity character of the intruder $^{13}/_{2}^{+}$ level in the region between the $N = 82$ and $N = 126$ shell closures. For a better understanding of nuclei in proton-shell closure regions, the recently conducted CLS measurements on tellurium, $Z = 52$, together with the investigation of thallium $Z = 81$, both also performed at COLLAPS, may give some further guidance.

The investigation of isomeric states in palladium isotopes in the mid-shell region could also have helped in finding an answer to this question. While this was originally one of the motivations for this work, these could unfortunately not be observed in the atomic spectra recorded at the newly established ATLANTIS setup at the Argonne National Laboratory.

With the palladium campaign serving as the online commissioning of ATLANTIS, an outstanding sensitivity of the new setup is shown. Despite extremely low ion yields provided by CARIBU, the sensitivity was sufficiently increased by bunching the ion beam with an RFQCB for unprecedented long accumulation times of up to $30\,\mathrm{s}$, which enables the study of many more interesting short-lived isotopes and isomers with low production yields. Also, the resonant and unexpectedly efficient charge exchange of palladium with magnesium provided an atomic beam for CLS with a high population of the required atomic state and it further increased the sensitivity. The new charge-exchange cell designed for the use with magnesium gives access to new population distributions after charge exchange, which could also increase the efficiency of charge exchange for other elements. Another remarkable feature was that the atomic spectra were very symmetric even at pressures that provided $\approx 90\,\%$ charge exchange probability.

The investigation of the palladium ground states reveals intricate nuclear structures and highlights the presence of nuclear ground-state shapes that deviate significantly from spherical symmetry as it was expected in this region. The deviation of the magnetic moments of $^1/_2{}^+$ isotopes from the Schmidt values can be qualitatively explained by the Nilsson model for deformed nuclei. However, calculation of the magnetic moments using state-of-the-art EDF calculations are ongoing but could not be finalized until this thesis was completed.

The observed increasing quadrupole moments when moving towards both, neutron and proton mid-shell, indicate an increasing nuclear deformation. This is in agreement with the deformation extracted from the observed differential ms charge radii using the Zamick-Talmi model and also with the trends observed in neighboring isotopic chains between the proton shell closures $Z = 26$ and $Z = 50$.

The precise determination of differential nuclear charge radii in comparison to EDF calculations indicate that the experimental values are better met by EDF calculations allowing triaxial ground states [31, 41, 42]. Not only the overall trend of the differential ms charge radii, but also the pattern of odd-even staggering including inverted OES for ^{113}Pd is predicted better when triaxiality is allowed. The results of this work contribute to the ongoing debate about the nature of nuclear deformation in this region, but for a convincing conclusion precise measurements of further isotopes in this region are needed. A first step in this direction is the investigation of ruthenium isotopes, which took place at ATLANTIS right after the commissioning with palladium and its analysis is still ongoing.

The findings from both lead and palladium isotopes underscore the importance of high-precision laser spectroscopy in probing nuclear structure and have contributed valuable data to the field of nuclear physics, aiding in the refinement of nuclear models and the understanding of nuclear structure. The precise measurements of nuclear properties in lead and palladium isotopes not only benchmark existing theoretical frameworks but also pave the way for future investigations into more exotic nuclei and the underlying forces that govern their behavior.

The herewith established new infrastructure ATLANTIS at Argonne National Laboratory (ANL) will serve several laser spectroscopy experiments. It is connected to the nuCARIBU facility, which is under commissioning and will soon provide short-lived isotopes from the neutron-induced fission of actinides. Proposals to study Tc, Ce, Nd and $La^{+}+$ were recently accepted by the ATLAS Physics Advisory Committee. Two of these proposals are from groups at ANL and Michigan State University. This demonstrates that ATLANTIS is of interest for abroad community and will contribute to our knowledge of nuclear structure in the regions of the nuclear chart that can be addressed by nuCARIBU.

Bibliography

[1] E. Rutherford. “LXXIX. The scattering of α and β particles by matter and the structure of the atom”. In: *The London, Edinburgh, and Dublin Philosophical Magazine and Journal of Science* 21.125 (1911), pp. 669–688. DOI: 10.1080/14786440508637080.

[2] E. Rutherford. “LIII. Collision of α particles with light atoms III. Nitrogen and oxygen atoms”. In: *The London, Edinburgh, and Dublin Philosophical Magazine and Journal of Science* 37.222 (1919), pp. 571–580. DOI: 10.1080/14786440608635918.

[3] E. Rutherford. “LIV. Collision of α particles with light atoms. IV. An anomalous effect in nitrogen”. In: *The London, Edinburgh, and Dublin Philosophical Magazine and Journal of Science* 37.222 (1919), pp. 581–587. DOI: 10.1080/14786440608635919.

[4] J. Chadwick. “Possible Existence of a Neutron”. In: *Nature* 129.3252 (1932), p. 312. DOI: 10.1038/129312a0.

[5] G. Gamow. “Mass defect curve and nuclear constitution”. In: *Proceedings of the Royal Society of London. Series A, Containing Papers of a Mathematical and Physical Character* 126.803 (1930), pp. 632–644. DOI: 10.1098/rspa.1930.0032.

[6] H. A. Bethe and R. F. Bacher. “Nuclear Physics A. Stationary States of Nuclei”. In: *Reviews of Modern Physics* 8.2 (1936), p. 82. DOI: 10.1103/RevModPhys.8.82.

[7] Heinz E. “Eine graphische Darstellung der Energietal-Fläche”. In: *Zeitschrift für Naturforschung A* 8.2-3 (1953), pp. 116–120. DOI: 10.1515/zna-1953-2-302.

[8] T. L. Collins, A. O. Nier, and W. H. Johnson, Jr. “Atomic Masses from Titanium through Zinc”. In: *Physical Review* 86.3 (1952), p. 408. DOI: 10.1103/PhysRev.86.408.

[9] J. H. D. Jensen M. Goeppert Mayer. *Elementary Theory of nuclear shell structure*. New York: John Wiley & Sons, Inc., 1955.

[10] A. Bohr and B. R. Mottelson. *Collective and individual-particle aspects of nuclear structure*. Vol. 27,16. Matematisk-fysiske meddelelser. København: Munksgaard in Komm, 1953. URL: https://cds.cern.ch/record/213298/files/p1.pdf (visited on 06/23/2024).

[11] B. R. Mottelson and S. G. Nilsson. “Classification of the Nucleonic States in Deformed Nuclei”. In: *Physical Review* 99.5 (1955), p. 1615. DOI: 10.1103/PhysRev.99.1615.

[12] G. Colò. “Nuclear density functional theory”. In: *Advances in Physics: X* 5.1 (2020), p. 1740061. DOI: 10.1080/23746149.2020.1740061.

[13] P.-G. Reinhard and W. Nazarewicz. “Toward a global description of nuclear charge radii: Exploring the Fayans energy density functional”. In: *Physical Review C* 95.6 (2017), p. 064328. DOI: 10.1103/PhysRevC.95.064328.

[14] X. Roca-Maza and N. Paar. “Nuclear equation of state from ground and collective excited state properties of nuclei”. In: *Progress in Particle and Nuclear Physics* 101 (2018), pp. 96–176. DOI: 10.1016/j.ppnp.2018.04.001.

[15] A. J. Miller et al. “Proton superfluidity and charge radii in proton-rich calcium isotopes”. In: *Nature Physics* 15.5 (2019), pp. 432–436. DOI: 10.1038/s41567-019-0416-9.

[16] S. Geldhof et al. “Impact of Nuclear Deformation and Pairing on the Charge Radii of Palladium Isotopes”. In: *Physical Review Letters* 128.15 (2022), p. 152501. DOI: 10.1103/PhysRevLett.128.152501.

[17] K. Blaum, J. Dilling, and W. Nörtershäuser. “Precision atomic physics techniques for nuclear physics with radioactive beams”. In: *Physica Scripta* 2013.T152 (2013), p. 014017. DOI: 10.1088/0031-8949/2013/T152/014017.

[18] O. Sorlin and M.-G. Porquet. “Nuclear magic numbers: New features far from stability”. In: *Progress in Particle and Nuclear Physics* 61.2 (2008), pp. 602–673. DOI: 10.1016/j.ppnp.2008.05.001.

[19] H. de Witte. “Nuclear Charge Radii of Neutron-Deficient Lead Isotopes Beyond $N = 104$ Midshell Investigated by In-Source Laser Spectroscopy”. In: *Physical Review Letters* 98.11 (2007), p. 112502. DOI: 10.1103/PhysRevLett.98.112502.

[20] W. D. Myers and K.-H. Schmidt. “An update on droplet-model charge distributions”. In: *Nuclear Physics A* 410.1 (1983), pp. 61–73. DOI: 10.1016/0375-9474(83)90401-3.

[21] K. König et al. “Surprising Charge-Radius Kink in the Sc Isotopes at $N = 20$”. In: *Physical Review Letters* 131.10 (2023), p. 102501. DOI: 10.1103/PhysRevLett.131.102501.

[22] M. M. Sharma, G. A. Lalazissis, and P. Ring. “Anomaly in the charge radii of Pb isotopes”. In: *Physics Letters B* 317.1 (1993), pp. 9–13. DOI: 10.1016/0370-2693(93)91561-Z.

[23] G. Racah. “Theory of Complex Spectra. I”. In: *Physical Review* 61.3-4 (1942), pp. 186–197. DOI: 10.1103/PhysRev.61.186.

[24] G. Racah. “Theory of Complex Spectra. II”. In: *Physical Review* 62.9-10 (1942), pp. 438–462. DOI: 10.1103/PhysRev.62.438.

[25] G. Racah and I. Talmi. “The pairing property of nuclear interactions”. In: *Physica* 18.12 (1952), pp. 1097–1100. DOI: 10.1016/S0031-8914(52)80178-8.

[26] B. H. Flowers. “Studies in jj -coupling. I. Classification of nuclear and atomic states”. In: *Proceedings of the Royal Society of London. Series A, Containing Papers of a Mathematical and Physical Character* 212.1109 (1952), pp. 248–263. DOI: 10.1098/rspa.1952.0079.

[27] D. T. Yordanov et al. “Structural trends in atomic nuclei from laser spectroscopy of tin”. In: *Communications Physics* 3.1 (2020), pp. 1–9. DOI: 10.1038/s42005-020-0348-9.

[28] D. T. Yordanov et al. “Simple Nuclear Structure in $^{111-129}$Cd from Atomic Isomer Shifts”. In: *Physical Review Letters* 116.3 (2016), p. 032501. DOI: 10.1103/PhysRevLett.116.032501.

[29] D. T. Yordanov et al. “Spins, Electromagnetic Moments, and Isomers of Cd107−129”. In: *Physical Review Letters* 110.19 (2013), p. 192501. DOI: 10.1103/PhysRevLett.110.192501.

[30] H. and Akito A. “Configuration Mixing and Quadrupole Moments of Odd Nuclei”. In: *Physical Review* 99.3 (1955), p. 778. DOI: 10.1103/PhysRev.99.778.

[31] G. Scamps et al. “Skyrme-Hartree-Fock-Bogoliubov mass models on a 3D mesh: effect of triaxial shape”. In: *The European Physical Journal A* 57.12 (2021), pp. 1–24. DOI: 10.1140/epja/s10050-021-00642-1.

[32] B. Cheal and K. T. Flanagan. “Progress in laser spectroscopy at radioactive ion beam facilities”. In: *Journal of Physics G: Nuclear and Particle Physics* 37.11 (2010), p. 113101. DOI: 10.1088/0954-3899/37/11/113101.

[33] F. C. Charlwood et al. “Nuclear charge radii of molybdenum fission fragments”. In: *Physics Letters B* 674.1 (2009), pp. 23–27. DOI: 10.1016/j.physletb.2009.02.050.

[34] B. Cheal et al. “Laser spectroscopy of niobium fission fragments: first use of optical pumping in an ion beam cooler buncher”. In: *Physical Review Letters* 102.22 (2009), p. 222501. DOI: 10.1103/PhysRevLett.102.222501.

[35] D. H. Forest et al. “Laser spectroscopy of neutron deficient zirconium isotopes”. In: *Journal of Physics G: Nuclear and Particle Physics* 28.12 (2002), pp. L63–L68. DOI: 10.1088/0954-3899/28/12/101.

[36] P. Campbell et al. “Laser spectroscopy of cooled zirconium fission fragments”. In: *Physical Review Letters* 89.8 (2002), p. 082501. DOI: 10.1103/PhysRevLett.89.082501.

[37] F. Buchinger et al. “Systematics of nuclear ground state properties in $^{78-100}$Sr by laser spectroscopy”. In: *Physical review. C, Nuclear physics* 41.6 (1990), pp. 2883–2897. DOI: 10.1103/physrevc.41.2883.

[38] P. Lievens et al. “On the odd-even staggering of mean-square charge radii in the light krypton and strontium region”. In: *Europhysics Letters (EPL)* 33.1 (1996), pp. 11–16. DOI: 10.1209/epl/i1996-00296-0.

[39] C. Thibault et al. “Hyperfine structure and isotope shift of the D_2 line of $^{76-98}$Rb and some of their isomers”. In: *Physical Review C* 23.6 (1981), p. 2720. DOI: 10.1103/PhysRevC.23.2720.

[40] L. E. Svensson et al. “Multiphonon vibrational states in 106,108Pd”. In: *Nuclear Physics A* 584.3 (1995), pp. 547–572. DOI: 10.1016/0375-9474(94)00514-N.

[41] W. Ryssens et al. “Skyrme–Hartree–Fock–Bogoliubov mass models on a 3D mesh: II. Time-reversal symmetry breaking”. In: *The European Physical Journal A* 58.12 (2022), pp. 1–29. DOI: 10.1140/epja/s10050-022-00894-5.

[42] G. Grams et al. “Skyrme-Hartree-Fock-Bogoliubov mass models on a 3D mesh: III. From atomic nuclei to neutron stars”. In: *The European Physical Journal A* 59.11 (2023), pp. 1–28. DOI: 10.1140/epja/s10050-023-01158-6.

[43] A. C. Mueller et al. “Spins, moments and charge radii of barium isotopes in the range $^{122-146}$Ba determined by collinear fast-beam laser spectroscopy”. In: *Nuclear Physics A* 403.2 (1983), pp. 234–262. DOI: 10.1016/0375-9474(83)90226-9.

[44] R. Neugart et al. “Collinear laser spectroscopy at ISOLDE: new methods and highlights”. In: *Journal of Physics G: Nuclear and Particle Physics* 44.6 (2017), p. 064002. DOI: 10.1088/1361-6471/aa6642.

[45] Guy S. et al. “CARIBU: a new facility for the study of neutron-rich isotopes”. In: *Hyperfine Interactions* 199 (2011), pp. 301–309. DOI: 10.1007/s10751-011-0325-5.

[46] Felix Sommer. “Nuclear Charge Radii across the N=Z=28 Shell Closure in Nickel Isotopes”. PhD thesis. Technische Universität Darmstadt, 2022. DOI: 10.26083/TUPRINTS-00020359.

[47] Jack T. Wilson et al. “Space-based measurement of the neutron lifetime using data from the neutron spectrometer on NASA’s MESSENGER mission”. In: *Physical Review Research* 2.2 (2020), p. 023316. DOI: 10.1103/PhysRevResearch.2.023316.

[48] P. A. Zyla et al. “Review of Particle Physics”. In: *Progress of Theoretical and Experimental Physics* 2020.8 (2020). DOI: 10.1093/ptep/ptaa104.

[49] W. Heisenberg. “Über den Bau der Atomkerne. I”. In: *Zeitschrift für Physik* 77.1 (1932), pp. 1–11. DOI: 10.1007/BF01342433.

[50] W. Demtröder. *Nuclear and Particle Physics*. 1st ed. 2022. Undergraduate Lecture Notes in Physics. Cham: Springer International Publishing and Imprint Springer, 2022. ISBN: 9783030583132. DOI: 10.1007/978-3-030-58313-2.

[51] National Nuclear Data Center. *information extracted from the NUDat database*. URL: https://www.nndc.bnl.gov/nudat/ (visited on 04/30/2024).

[52] M. G. Mayer. “On Closed Shells in Nuclei”. In: *Physical Review* 74.3 (1948), pp. 235–239. DOI: 10.1103/PhysRev.74.235.

[53] Otto Haxel, J. Hans D. Jensen, and Hans E. Suess. “On the ”Magic Numbers” in Nuclear Structure”. In: *Physical Review* 75.11 (1949), p. 1766. DOI: 10.1103/PhysRev.75.1766.2.

[54] G. Royer and R. Rousseau. “On the liquid drop model mass formulae and charge radii”. In: *The European Physical Journal A* 42.3 (2009), pp. 541–545. DOI: 10.1140/epja/i2008-10745-8.

[55] G. Fricke and K. Heilig, eds. *Numerical data and functional relationships in science and technology: New series*. Vol. 20. Berlin: Springer, 2004. ISBN: 3-540-42829-1. DOI: 10.1007/b87879.

[56] T. Suda and H. Simon. “Prospects for electron scattering on unstable, exotic nuclei”. In: *Progress in Particle and Nuclear Physics* 96 (2017), pp. 1–31. DOI: 10.1016/j.ppnp.2017.04.002.

[57] E. Tiesinga et al. “CODATA Recommended Values of the Fundamental Physical Constants: 2018”. In: *Journal of physical and chemical reference data* 50.3 (2021), p. 033105. DOI: 10.1063/5.0064853.

[58] M. Honma et al. “New effective interaction for f_5pg_9-shell nuclei”. In: *Physical Review C* 80.6 (2009), p. 064323. DOI: 10.1103/PhysRevC.80.064323.

[59] M. Anselment et al. “Charge radii and moments of tin nuclei by laser spectroscopy”. In: *Physical review. C, Nuclear physics* 34.3 (1986), pp. 1052–1059. DOI: 10.1103/physrevc.34.1052.

[60] F. Le Blanc et al. “Charge-radius change and nuclear moments in the heavy tin isotopes from laser spectroscopy: Charge radius of ^{132}Sn”. In: *Physical Review C* 72.3 (2005), p. 034305. DOI: 10.1103/PhysRevC.72.034305.

[61] V. Fella et al. “Magnetic moment of ^{207}Pb and the hyperfine splitting of $^{207}Pb^{+}_{81}$”. In: *Physical Review Research* 2.1 (2020), p. 013368. DOI: 10.1103/PhysRevResearch.2.013368.

[62] A. Bohr and B. R. Mottelson. *Nuclear structure: Single-Particle Motion*. [New ed.] Vol. 1. Singapore: World Scientific, 1998. ISBN: 9810239793.

[63] A. Bohr and B. R. Mottelson. *Nuclear structure: Nuclear Deformations*. [New ed.] Vol. 2. Singapore: World Scientific, 1998. ISBN: 9810239807.

[64] A. De-Shalit and I. Talmi. *Nuclear shell theory*. Vol. 14. Pure and applied physics. New York: Academic Press, 1963.

[65] R. Machleidt and D.R. Entem. “Chiral effective field theory and nuclear forces”. In: *Physics Reports* 503.1 (2011), pp. 1–75. DOI: https://doi.org/10.1016/j.physrep.2011.02.001.

[66] E. Epelbaum, H.-W. Hammer, and Ulf-G. Meißner. “Modern theory of nuclear forces”. In: *Rev. Mod. Phys.* 81 (4 Dec. 2009), pp. 1773–1825. DOI: 10.1103/RevModPhys.81.1773.

[67] Kai Hebeler. “Three-nucleon forces: Implementation and applications to atomic nuclei and dense matter”. In: *Physics Reports* 890 (2021). Three-nucleon forces: Implementation and applications to atomic nuclei and dense matter, pp. 1–116. DOI: https://doi.org/10.1016/j.physrep.2020.08.009.

[68] S.K. Bogner, R.J. Furnstahl, and A. Schwenk. “From low-momentum interactions to nuclear structure”. In: *Progress in Particle and Nuclear Physics* 65.1 (2010), pp. 94–147. DOI: https://doi.org/10.1016/j.ppnp.2010.03.001.

[69] H. Hergert et al. “The In-Medium Similarity Renormalization Group: A novel ab initio method for nuclei”. In: *Physics Reports* 621 (2016). Memorial Volume in Honor of Gerald E. Brown, pp. 165–222. DOI: https://doi.org/10.1016/j.physrep.2015.12.007.

[70] S. Ragnar Stroberg et al. “Nonempirical Interactions for the Nuclear Shell Model: An Update”. In: *Annual Review of Nuclear and Particle Science* 69 (2019), pp. 307–362. DOI: https://doi.org/10.1146/annurev-nucl-101917-021120.

[71] H. Hergert. “A Guided Tour of ab initio Nuclear Many-Body Theory”. In: *Frontiers in Physics* 8 (2020), p. 578923. DOI: 10.3389/fphy.2020.00379.

[72] Baishan Hu et al. “Ab initio predictions link the neutron skin of ^{208}Pb to nuclear forces”. In: *Nature Phys.* 18.10 (2022), pp. 1196–1200. DOI: 10.1038/s41567-023-02324-9. arXiv: 2112.01125 [nucl-th].

[73] K. Hebeler et al. “Normal ordering of three-nucleon interactions for ab initio calculations of heavy nuclei”. In: *Phys. Rev. C* 107.2 (2023), p. 024310. DOI: 10.1103/PhysRevC.107.024310. arXiv: 2211.16262 [nucl-th].

[74] P. Hohenberg and W. Kohn. “Inhomogeneous Electron Gas”. In: *Physical Review* 136.3B (1964), B864. DOI: 10.1103/PhysRev.136.B864.

[75] W. Kohn and L. J. Sham. “Self-Consistent Equations Including Exchange and Correlation Effects”. In: *Physical Review* 140.4A (1965), A1133. DOI: 10.1103/PhysRev.140.A1133.

[76] C. J. Foot. *Atomic physics*. Oxford master series in atomic, optical and laser physics. Oxford and New York: Oxford University Press, 2011. ISBN: 978 0 19 850695 9.

[77] W. H. King. *Isotope Shifts in Atomic Spectra*. Physics of Atoms and Molecules. Boston, MA and s.l.: Springer US, 1984. ISBN: 978-1-4899-1788-1. DOI: 10.1007/978-1-4899-1786-7.

[78] G. Drake, ed. *Springer Handbook of Atomic, Molecular, and Optical Physics*. New York, NY: Springer Science+Business Media Inc, 2006. ISBN: 9780387263083. DOI: 10.1007/978-0-387-26308-3.

[79] E. C. Seltzer. “K X-Ray Isotope Shifts”. In: *Physical Review* 188.4 (1969), p. 1916. DOI: 10.1103/PhysRev.188.1916.

[80] F. Boehm and P. L. Lee. “Changes of mean-square nuclear charge radii from isotope shifts of electronic K_α X-rays”. In: *Atomic Data and Nuclear Data Tables* 14.5 (1974), pp. 605–611. DOI: 10.1016/S0092-640X(74)80005-7.

[81] S. A. Blundell et al. “A reformulation of the theory of field isotope shift in atoms”. In: *Journal of Physics B: Atomic and Molecular Physics* 20.15 (1987), p. 3663. DOI: 10.1088/0022-3700/20/15/015.

[82] J. C. Berengut et al. “Generalized King linearity and new physics searches with isotope shifts”. In: *Physical Review Research* 2.4 (2020), p. 043444. DOI: 10.1103/PhysRevResearch.2.043444.

[83] M. Door et al. *Search for new bosons with ytterbium isotope shifts*. 2024. DOI: /doi.org/10.48550/arXiv.2403.07792.

[84] J. Hur et al. “Evidence of Two-Source King Plot Nonlinearity in Spectroscopic Search for New Boson”. In: *Physical Review Letters* 128.16 (2022), p. 163201. DOI: 10.1103/PhysRevLett.128.163201.

[85] K. Ono et al. “Observation of Nonlinearity of Generalized King Plot in the Search for New Boson”. In: *Physical Review X* 12.2 (2022), p. 021033. DOI: 10.1103/PhysRevX.12.021033.

[86] C. Solaro et al. “Improved Isotope-Shift-Based Bounds on Bosons beyond the Standard Model through Measurements of the $^2D_{3/2} - ^2D_{5/2}$ Interval in Ca^+”. In: *Physical Review Letters* 125.12 (2020), p. 123003. DOI: 10.1103/PhysRevLett.125.123003.

[87] T. T. Chang et al. *Systematic-free limit on new light scalar bosons via isotope shift spectroscopy in Ca^+*. 2023. DOI: 10.48550/arXiv.2311.17337.

[88] W. Demtröder. *Atoms, molecules and photons: An introduction to atomic-, molecular- and quantum physics*. 2018. DOI: 10.1007/978-3-662-55523-1.

[89] A. R. Vernon et al. “Simulation of the relative atomic populations of elements $1 \leq Z \leq 89$ following charge exchange tested with collinear resonance ionization spectroscopy of indium”. In: *Spectrochimica Acta Part B: Atomic Spectroscopy* 153 (2019), pp. 61–83. DOI: 10.1016/j.sab.2019.02.001.

[90] A. Kramida and Y. Ralchenko. *NIST Atomic Spectra Database, NIST Standard Reference Database 78*. 2023. DOI: 10.18434/T4W30F.

[91] U. Dinger et al. “Nuclear moments and change in the charge-radii of neutron deficient lead isotopes”. In: *Zeitschrift für Physik A Atomic Nuclei* 328.2 (1987), pp. 253–254. DOI: 10.1007/BF01290669.

[92] S. B. Dutta et al. “Measurement of isotope shift and hyperfine splitting of ^{190,191,193,197}Pb isotopes by collinear laser spectroscopy”. In: *Zeitschrift für Physik A Hadrons and Nuclei* 341.1 (1991), pp. 39–45. DOI: 10.1007/BF01281272.

[93] M. D. Seliverstov et al. “Charge radii and magnetic moments of odd- A $^{183-189}$Pb isotopes”. In: *The European Physical Journal A* 41.3 (2009), pp. 315–321. DOI: 10.1140/epja/i2009-10817-3.

[94] Y. X. Luo et al. “New insights into the nuclear structure in neutron-rich ^{112,114,115,116,117,118}Pd”. In: *Nuclear Physics A* 919 (2013), pp. 67–98. DOI: 10.1016/j.nuclphysa.2013.10.002.

[95] X. F. Yang et al. “Laser spectroscopy for the study of exotic nuclei”. In: *Progress in Particle and Nuclear Physics* 129.5 (2023), p. 104005. ISSN: 0146-6410. DOI: 10.1016/j.ppnp.2022.104005.

[96] B. Schinzler et al. “Collinear laser spectroscopy of neutron-rich Cs isotopes at an on-line mass separator”. In: *Physics Letters B* 79.3 (1978), pp. 209–212. ISSN: 0370-2693. DOI: 10.1016/0370-2693(78)90224-1.

[97] R. Neugart et al. “Fast-beam laser spectroscopy of neutron-rich barium isotopes”. In: *Hyperfine Interactions* 9.1 (1981), pp. 151–157. ISSN: 1572-9540. DOI: 10.1007/BF01020911.

[98] R. Catherall et al. “The ISOLDE facility”. In: *Journal of Physics G: Nuclear and Particle Physics* 44.9 (2017), p. 094002. ISSN: 0954-3899. DOI: 10.1088/1361-6471/aa7eba.

[99] U. Köster et al. “On-line yields obtained with the ISOLDE RILIS”. In: *Nuclear Instruments and Methods in Physics Research Section B: Beam Interactions with Materials and Atoms* 204 (2003), pp. 347–352. ISSN: 0168583X. DOI: 10.1016/S0168-583X(02)01956-0.

[100] I. Podadera-Aliseda. “New developments on preparation of cooled and bunched Radioactive Ion beams at ISOL facilities : the ISCOOL project and the rotating wall cooling”. PhD thesis. Barcelona, Polytechnic U, 2006. DOI: 10.17181/CERN.A80J.OPTX.

[101] E. Mané. “High resolution laser spectroscopy of radioactive isotopes using a RFQ cooler-buncher at CERN-ISOLDE”. PhD dissertation. Manchaster: University of Manchester, 2009.

[102] K. König et al. *High Voltage Determination and Stabilization for Collinear Laser Spectroscopy Applications*. 2024.

[103] S. L. Kaufman. “High-resolution laser spectroscopy in fast beams”. In: *Optics Communications* 17.3 (1976), pp. 309–312. ISSN: 0030-4018. DOI: 10.1016/0030-4018(76)90267-4.

[104] K. -R. Anton et al. “Collinear Laser Spectroscopy on Fast Atomic Beams”. In: *Physical Review Letters* 40.10 (1978), p. 642. DOI: 10.1103/PhysRevLett.40.642.

[105] K. Kreim et al. “Nuclear charge radii of potassium isotopes beyond $N = 28$”. In: *Physics Letters B* 731 (2014), pp. 97–102. ISSN: 0370-2693. DOI: 10.1016/j.physletb.2014.02.012.

[106] E. Riis et al. “Absolute wavelength measurement and fine-structure determination in ^{7}ii”. In: *Physical Review A* 33.5 (1986), p. 3023. DOI: 10.1103/PhysRevA.33.3023.

[107] W. Nörtershäuser et al. “Nuclear Charge Radii of ^{7,9,10}Be and the One-Neutron Halo Nucleus ^{11}Be”. In: *Physical Review Letters* 102.6 (2009), p. 062503. DOI: 10.1103/PhysRevLett.102.062503.

[108] B. Maaß. “Laser Spectroscopy of the Boron Isotopic Chain”. PhD thesis. Darmstadt: Technische Universität Darmstadt, 2020. DOI: 10.25534/tuprints-00011484.

[109] Matthew G. et al. “Second generation degrader foil for the CARIBU project”. In: *EPJ Web of Conferences* 229 (2020), p. 06002. ISSN: 2100-014X. DOI: 10.1051/epjconf/202022906002.

[110] *CARIBU Beams | Argonne National Laboratory*. Lemont (Illinois), 2023. URL: https://www.anl.gov/atlas/caribu-beams (visited on 02/19/2024).

[111] K. Minamisono et al. “Commissioning of the collinear laser spectroscopy system in the BECOLA facility at NSCL”. In: *Nuclear Instruments and Methods in Physics Research Section A: Accelerators, Spectrometers, Detectors and Associated Equipment* 709 (2013), pp. 85–94. ISSN: 0168-9002. DOI: 10.1016/j.nima.2013.01.038.

[112] B. R. Barquest. “An advanced ion guide for beam cooling and bunching for collinear laser spectroscopy of rare isotopes”. Dissertation. Lansing (Michigan): Michigan State University, 2014.

[113] W. M. Haynes, ed. *CRC handbook of chemistry and physics*. 95th ed. Boca Raton, FL: CRC Press, an imprint of Taylor and Francis, 2014. ISBN: 978-1-4822-0868-9.

[114] S. Kaufmann. *Laser spectroscopy of nickel isotopes with a new data acquisition system at ISOLDE*. Darmstadt, 2019.

[115] W. Demtröder. *Laser Spectroscopy 1: Basic Principles*. 5. 5th ed. 2014. Berlin, Heidelberg: Springer Berlin Heidelberg, 2014. ISBN: 9783642538599.

[116] Patrick Müller. *qspec 0.2.0: A python package for calculations surrounding laser spectroscopy*. 2023. URL: https://pypi.org/project/qspec/ (visited on 06/23/2024).

[117] M. Hammen. "Spins, moments and radii of Cd isotopes". PhD thesis. Johannes Gutenberg-Universität Mainz, 2013. DOI: 10.25358/OPENSCIENCE-1792.

[118] M. Verlinde et al. "On the performance of wavelength meters: Part 1—consequences for medium-to-high-resolution laser spectroscopy". In: *Applied Physics B* 126.5 (2020), pp. 1–14. ISSN: 1432-0649. DOI: 10.1007/s00340-020-07425-4.

[119] K. König et al. "On the performance of wavelength meters: Part 2—frequency-comb based characterization for more accurate absolute wavelength determinations". In: *Applied Physics B* 126.5 (2020), pp. 1–8. ISSN: 1432-0649. DOI: 10.1007/s00340-020-07433-4.

[120] J. Dembczyński and H. Rebel. "Fine- and hyperfine structure analysis of the odd configurations in the lead atom". In: *Zeitschrift für Physik A Atoms and Nuclei* 315.2 (1984), pp. 137–144. DOI: 10.1007/BF01419372.

[121] T. J. Wasowicz. "Electronic and nuclear properties from the analysis of the isotope shifts in the spectral lines of lead". In: *The European Physical Journal D* 53.3 (2009), pp. 263–272. ISSN: 1434-6079. DOI: 10.1140/epjd/e2009-00133-6.

[122] Paul-Gerhard Reinhard et al. *Extended Fayans energy density functional: optimization and analysis*. 2024. arXiv: 2402.15380 [nucl-th]. URL: https://arxiv.org/abs/2402.15380.

[123] R. L. Kurucz and B. Bell. *1995 Atomic Line Data: Kurucz CD-ROM No. 23*. Cambridge, Mass.: Smithsonian Astrophysical Observatory.

[124] W. Demtröder. *Laser Spectroscopy 2: Experimental Techniques*. 5. 5th ed. 2015. Berlin, Heidelberg: Springer Berlin Heidelberg, 2015. ISBN: 978-3-662-44641-6. DOI: 10.1007/978-3-662-44641-6.

[125] J. J. Olivero and R. L. Longbothum. "Empirical fits to the Voigt line width: A brief review". In: *Journal of Quantitative Spectroscopy and Radiative Transfer* 17.2 (1977), pp. 233–236. ISSN: 0022-4073. DOI: 10.1016/0022-4073(77)90161-3.

[126] K. H. Channappa and J. M. Pendlebury. "Hyperfine structure measurements in some low-lying multiplets of ^{47}Ti, ^{49}Ti, ^{59}Co and ^{105}Pd". In: *Proceedings of the Physical Society* 86.5 (1965), pp. 1145–1146. ISSN: 0370-1328. DOI: 10.1088/0370-1328/86/5/126.

[127] J. Blachot. *Nucl. Data Sheets 113*. 2012. URL: https://www.nndc.bnl.gov/ensdf/ (visited on 10/10/2023).

[128] J. A. Seitchik, A. C. Gossard, and V. Jaccarino. “Knight Shifts and Susceptibilities of Transition Metals: Palladium”. In: *Physical Review* 136.4A (1964), A1119–A1125. ISSN: 0031-899X. DOI: 10.1103/PhysRev.136.A1119.

[129] J.-L. Vuilleumier et al. “Nuclear charge parameters and quadrupole moment in ^{105}Pd from muonic X-rays”. In: *Nuclear Physics A* 294.3 (1978), pp. 273–277. DOI: 10.1016/0375-9474(78)90217-8.

[130] J.R. Persson. “Table of hyperfine anomaly in atomic systems”. In: *Atomic Data and Nuclear Data Tables* 99.1 (2013), pp. 62–68. ISSN: 0092-640X. DOI: https://doi.org/10.1016/j.adt.2012.04.002.

[131] A. Ortiz Cortes. “Palladium: a Study of Nuclear Deformation of a Refractory Element. Laser Spectroscopy at the IGISOL (Jyväskylä, Finland) and S3-LEB (GANIL, France)”. In: *JYU dissertations* (2023).

[132] N. J. Stone. *Table of Recommended Nuclear Magnetic Dipole Moments: Part I - Long-lived States*. 2019. DOI: 10.61092/iaea.yjpc-cns6.

[133] Parnefjord Gustafsson, F. O. A. “The evolution of nuclear moments and charge radii approaching ^{100}Sn”. PhD thesis. KU Leuven, 2022. URL: https://cds.cern.ch/record/2799928?ln=de (visited on 06/23/2024).

[134] D. T. Yordanov et al. “Spins and electromagnetic moments of $^{101-109}$Cd”. In: *Physical Review C* 98.1 (2018). DOI: 10.1103/PhysRevC.98.011303.

[135] N. Frömmgen et al. “Collinear laser spectroscopy of atomic cadmium”. In: *The European Physical Journal D* 69.6 (2015), pp. 1–12. ISSN: 1434-6079. DOI: 10.1140/epjd/e2015-60219-0.

[136] N. J. Stone. *Table of Recommended Nuclear Magnetic Dipole Moments - Part II, Short-lived States*. 2020. DOI: 10.61092/iaea.pd7h-zvmy.

[137] R. B. Firestone. *Table of Isotopes*. CD-ROM. 1996. URL: https://application.wiley-vch.de/books/info/0-471-35633-6/toi99/toi.htm (visited on 06/23/2024).

[138] S. G. Nilsson. “Binding states of individual nucleons in strongly deformed nuclei”. In: *Dan. Mat. Fys. Medd.* 29.CERN-55-30 (1955).

[139] L. Zamick. “Two body contribution to the effective radius operator”. In: *Annals of Physics* 66.2 (1971), pp. 784–789. ISSN: 0003-4916. DOI: 10.1016/0003-4916(71)90080-7.

[140] I. Talmi. “On the odd-even effect in the charge radii of isotopes”. In: *Nuclear Physics A* 423.2 (1984), pp. 189–196. ISSN: 03759474. DOI: 10.1016/0375-9474(84)90587-6.

[141] M. Hammen et al. “From Calcium to Cadmium: Testing the Pairing Functional through Charge Radii Measurements of $^{100-130}$Cd”. In: *Physical Review Letters* 121.10 (2018), p. 102501. DOI: 10.1103/PhysRevLett.121.102501.

[142] M. Keim et al. “Laser-spectroscopy measurements of $^{72-96}$Kr spins, moments and charge radii”. In: *Nuclear Physics A* 586 (1995), pp. 219–239. DOI: doi.org/10.1016/0375-9474(94)00786-M.

[143] P. Kumar et al. “Nuclear shape evolution and shape coexistence in Zr and Mo isotopes”. In: *The European Physical Journal A* 57.1 (2021), pp. 1–13. ISSN: 1434-601X. DOI: 10.1140/epja/s10050-021-00346-6.

Acknowledgements

I would like to express my gratitude to all those who have contributed to the successful completion of my doctoral studies and this thesis.

Firstly, I extend my greatest thanks to Wilfried Nörtershäuser, who has been an exceptional supervisor and mentor already throughout my Bachelor's and Master's, and even more during my doctoral studies. His support and encouragement have been really beneficial in my academic journey. The incredible opportunities to be a part of a large collaboration like COLLAPS, and to participate in conferences, summer schools, and experiments worldwide, were all made possible by his efforts. This experience has been immensely rewarding and fascinating.

The ATLANTIS setup and palladium beamtime would not have been possible without the immense effort put in by Bernhard. Thank you for introducing me to the lab, showing me around Chicago, and for your relentless support during any crisis situations during the beamtimes. This project would also not have been possible without Peter, who has actively supported the initiative locally from the very beginning. I also extend my gratitude to Guy Savard and Daniel Santiago-Gonzalez for their efforts in making CARIBU behave.

I am also very grateful to Liss for her invaluable guidance in teaching me the intricacies of fitting and analyzing CLS data. Her expertise and patience have been crucial to my research, and I learned a great deal during our discussions about the lead data.

I also want to thank all the members of the LaserSpHERe group, who have created such a pleasant, productive, and supportive working environment. I especially want to mention Patrick, who never seemed to tire of answering my questions about his qspec python package, as well as Bernhard and Kristian for all the discussions we had about the palladium data.

Of course, a very important thank you goes to all the proofreaders, especially Liss, Bernhard, and Wilfried. Despite the limited time, you managed to provide me with very detailed and important feedback on my writing.

The SFB 1245 has greatly supported my doctoral position. I benefited from the integrated research training group and the strong network within the SFB. Being part of the gender-equality team and planning workshops with Sabrina and Almudena has broadened my horizons. I enjoyed the regular Women's Lunches and appreciated the opportunities to connect with other experimentalists and theorists in my field during the annual workshops and other SFB occasions.

Since a doctoral study is not only about science but also involves a lot of administration, I am very thankful to Giovanna Umberti Caroli and Carina Seeger, who always helped me with all the bureaucracy.

I also want to thank Prof. Dr. Alexandre Obertelli for agreeing to be my second reviewer, as well as Prof. Dr. Achim Schwenk and Prof. Dr. Michael Vogel for agreeing to be on my examination committee.

Meine gesamte Studienzeit wäre ohne meine liebsten Mitstudenten nicht das Gleiche gewesen. Mark, Tobi (Grübchen), Timo, Thomas, Tobi und Sebastian, euch habe ich teilweise schon an meinem ersten Tag an der TU kennengelernt und ihr habt bis zum Schluss mit mir durchgehalten. Ihr habt die Studienzeit und auch die letzten viereinhalb Jahre für mich zu einer ganz besonderen Zeit gemacht und ich hoffe sehr, dass unsere Geschichte hier noch nicht vorbei ist.

Den notwendigen Ausgleich zur doch sehr rationalen Physik haben all die wunderbaren Menschen in meinem Verein geschaffen. Jedes Jahr mit euch auf der Bühne zu stehen und all die kreativen Vorbereitungen, die wir dazu gemeinsam getroffen haben, haben mich immer wieder durchgeschüttelt und mir neue Energie für die akademische Welt gegeben.

Danke, Dennis, für die letzten 12 Jahre, für unser gemeinsames Erwachsenwerden in Darmstadt, für deine Unterstützung und Geduld und für dein immer wieder gutes Zureden, wenn ich es so dringend gebraucht habe.

Nichts von alledem wäre möglich gewesen ohne die bedingungslose Unterstützung meiner Familie. Von klein auf haben meine Eltern mich in meiner Neugier bestärkt und mir geholfen, meinen Wissensdurst zu stillen. Egal ob Pflanzen, Musik, Dinos oder Technik, was mich und meine Brüder interessiert hat, wurde uns gezeigt, ausprobiert und erklärt. Meinen Großeltern gebührt der Dank, dass ich mich von Anfang an voll und ganz auf das Studium konzentrieren konnte und sie mir immer wieder gezeigt haben, wie stolz sie auf mich sind.

merrsie-aach